2012

Hadronic physics from extensive air showers

Guofeng Yuan
Louisiana State University and Agricultural and Mechanical College, gyuan2@lsu.edu

HADRONIC PHYSICS FROM EXTENSIVE AIR SHOWERS

A Dissertation

Submitted to the Graduate Faculty of the
Louisiana State University and
Agricultural and Mechanical College
in partial fulfillment of the
requirements for the degree of
Doctor of Philosophy

in

The Department of Physics and Astronomy

by
Guofeng Yuan
B.S., University of Science and Technology of China, 2006
December 2012

In loving memory of my grandfather, Yunzhao Yuan (1928 - 2011).

Acknowledgements

First and foremost, I would like to give my appreciations to my advisor Dr. James Matthews, for his clear guidance, limitless support, patience and encouragement. During the four and half years working with him, I am not only benefited a lot from his broad knowledge and creative thoughts, but also learned a lot from his nice personality, some of his jokes would just make my day. His explanations just made the difficult concepts easy and clear. It is a great privilege to work with him.

I would also like to thank my committee members, Dr. Gabriela González, Dr. William Metcalf, Dr. Hwang Lee and Dr. Guoping Zhang. Thank you very much for your time and effort.

I also want to express my appreciations to my current and former lab mates, Dr. Michael Sutherland, Azadeh Keivani, Amir Shadkam and Dr. Viviana Scherini. I got a lot of valuable ideas and help in the discussion and I feel fortunate that I can do research together with you guys. I would especially like to thank Mike for helping me with the thesis editing.

I also thank Pierre Auger Collaboration and Department of Energy, for providing me such opportunity to tackle the interesting and challenging topics and to work with brilliant people from all over the world.

I would like to thank my teachers in middle school and high school, Wanzhou Dong, Lingyun Pan and Sancheng Li, for showing me the beauty of physics and mathematics. I would also like to thank my undergraduate professors at University of Science and Technology of China, for providing me good foundation for my graduate study.

I would especially like to thank my dearest wife Ling. Her love and encouragement is always there when I need. I am so glad we can spend our life together.

I would also like to thank my friends in and out of LSU (too many to name), you made my study aboard more colorful and memorable. These friendships are lifetime treasure and I will also remember that. I feel that no matter what country you are from, most values are

shared. The friendship bridge can be built easily across the culture differences.

Finally, I would like to thank my parents, Wensong Yuan and Shuduan Guo, my sister, Yingfeng Yuan, for their unconditional love and support. Without them, I would never make it today.

Table of Contents

Dedication . . . ii

Acknowledgements . . . iii

List of Tables . . . vii

List of Figures . . . viii

Abstract . . . xii

1. Introduction . . . 1

2. Ultra-High Energy Cosmic Ray Physics . . . 3
   2.1 History . . . 3
   2.2 Energy Spectrum . . . 4
   2.3 Origin and Propagation . . . 6
      2.3.1 Sources and Acceleration . . . 6
      2.3.2 Magnetic Field . . . 11
      2.3.3 GZK Cutoff . . . 11
   2.4 Composition . . . 17
      2.4.1 Composition of the UHECR . . . 17
         2.4.1.1 Neutrinos and Photons . . . 17
   2.5 Extensive Air Showers (EAS) . . . 18
      2.5.1 Physics of Air showers . . . 20
         2.5.1.1 Electromagnetic EAS . . . 20
         2.5.1.2 Hadronic EAS . . . 21
      2.5.2 EAS Detection Technique . . . 24
         2.5.2.1 Air Fluorescence detection . . . 25
         2.5.2.2 Surface Array Detection . . . 28

3. Pierre Auger Observatory . . . 31
   3.1 Overview . . . 31
   3.2 The Surface Detector (SD) . . . 31
      3.2.1 Surface Detector Design . . . 33
      3.2.2 Data Acquisition and Detector Calibration . . . 35
      3.2.3 SD Tigger System . . . 36
         3.2.3.1 Local Triggers . . . 36
         3.2.3.2 CDAS Triggers . . . 37
         3.2.3.3 Offline Triggers . . . 38
      3.2.4 SD Event Reconstruction . . . 40
   3.3 The Fluorescence Detector (FD) . . . 43
      3.3.1 Fluorescence Detector Design . . . 44
         3.3.1.1 Optical System of FD . . . 46
      3.3.2 Data Acquisition . . . 49
      3.3.3 FD Electronics and Trigger System . . . 49
         3.3.3.1 Hardware Triggers . . . 51
         3.3.3.2 Software Triggers . . . 51

3.3.4 FD Calibration . . . 52
3.3.5 FD Event Reconstruction . . . 54
3.3.5.1 Geometrical Reconstruction . . . 54
3.3.5.2 Shower Profile and Energy Reconstruction . . . 55
3.4 Hybrid Events . . . 55
3.5 Atmosphere Monitoring . . . 58
3.5.1 Central Laser Facility (CLF) and eXtreme Laser Facility (XLF) . . . 59
3.5.2 LIght Detection And Ranging (LIDAR) . . . 60
3.5.3 Infrared Cloud Camera (IR camera) . . . 60
3.5.4 Radiosonde Balloons . . . 61
3.5.5 Aerosol Phase Function monitors (APF) . . . 62
3.5.6 Horizontal Attenuation Monitors (HAM) . . . 62
3.5.7 Fotometric Robotic Atmosphere Monitoring (FRAM) . . . 62
3.6 PAO Scientific Results . . . 63
3.6.1 Photons and Neutrinos Limits . . . 63
3.6.2 Cosmic Ray Flux and GZK Cutoff Observation . . . 65
3.6.3 Composition Studies with Depth of Shower Maximum (X_{max}) . . . 66
3.6.4 Anisotropy Studies with the Arrival Direction . . . 67
3.6.5 Ultra-High Energy Proton Cross Section with Air . . . 69

4. Surface Detector FADC Peak Finding Method . . . 74
4.1 Introduction . . . 74
4.2 Hadronic Physics at Highest Energy Level . . . 74
4.2.1 Leading Particle Physics . . . 75
4.2.1.1 FD "Double Bump" Events . . . 75
4.2.1.2 SD "Double Shell" Events . . . 76
4.2.2 Connect SD with FD . . . 82
4.2.2.1 The Normal Events . . . 82
4.2.2.2 Double Shell Event Candidates . . . 87
4.2.3 Leading Particle Cross Section Implications . . . 89
4.3 Discussion and Summary . . . 92

5. New Methods for Muon Counting . . . 94
5.1 Introduction . . . 94
5.2 Muon Signal Characters . . . 94
5.3 Garrido's Method . . . 95
5.4 New Methods for Muon Counting . . . 96
5.5 SD Stations Selection . . . 97
5.6 Results . . . 99
5.6.1 The Simulation Correlation Results . . . 99
5.6.2 Grouping Improves the Correlation . . . 101
5.6.3 Results with the PAO Data . . . 103
5.7 Discussion and Summary . . . 105

6. Summary and Outlook . . . 115
6.1 Summary . . . 115
6.2 Outlook . . . 116

Bibliography . . . 117

Vita . . . 124

List of Tables

3.1 The location and operation information of past and present experiments. . . 32

3.2 Surface detector comparison from different experiments. 33

3.3 Trigger levels used by the fluorescence detector 50

3.4 FD photon fraction limit result. 64

3.5 SD photon fraction limit result. 64

List of Figures

2.1 Observed energy spectrum of cosmic rays. 5

2.2 Schematic diagram of second order Fermi acceleration. 8

2.3 Schematic diagram of first order Fermi acceleration. 8

2.4 The Hillas plot showing possible sites for UHECR accelerations. 10

2.5 Schematic diagram of different Galactic Magnetic Field (GMF). 12

2.6 Simulated trajectories of nuclei in the BSS-S GMF model. 13

2.7 The intensity of the cosmic microwave background versus frequency. 14

2.8 The nucleon interaction length and attenuation length. 16

2.9 Primary composition of cosmic rays. 18

2.10 Schematic diagram of EAS. 19

2.11 Schematic diagram of electromagnetic and hadronic cascades. 20

2.12 Longitudinal profiles of high-energy showers. 26

2.13 Schematic plot of EAS detection by a fluorescence detector. 27

2.14 Volcano Ranch array surface detector position arrangement. 29

3.1 A map of Auger south site. 32

3.2 A surface detector overlooked by a fluorescence detector. 33

3.3 Schematic overview of the surface detector design. 34

3.4 First three trigger levels of the Auger surface detector 37

3.5 Example of two T3 modes. 38

3.6 The offline triggers of the Auger surface detector. 39

3.7 Trigger efficiency of the Auger surface detector as a function of energy. . . . 40

3.8 Signal density as a function of distance from the shower axis. 42

3.9 Correlation between S_{38} and the FD reconstructed energy. 43

3.10 Reconstruction of a real SD event. 44

3.11 Measured fluorescence spectrum. 45
3.12 Schematic top view of the fluorescence detector layout. 45
3.13 Schematic view of a fluorescence detector telescope. 46
3.14 Geometrical structure of the FD optical system. 47
3.15 Mercedes stars and light collectors. 48
3.16 Schematic plot of the FD data acquisition system. 50
3.17 Basic types of pattern of SLT 51
3.18 Reconstruction of a real FD event. 56
3.19 A hybrid event example. 57
3.20 Reconstruction comparison between monocular and hybrid data. 57
3.21 The locations of the atmosphere monitoring facilities in the PAO map. . . . 58
3.22 The central laser facility. 59
3.23 An example cloud image from the IR camera. 61
3.24 The highest energy cosmic ray spectrum. 66
3.25 PAO $\langle X_{max} \rangle$ and RMS(X_{max}) result 67
3.26 Sky map of PAO correlation result in 2007. 69
3.27 Sequential PAO correlation result for period II and III. 70
3.28 Unbinned likelihood fit of Λ_η to the tail of X_{max}. 71
3.29 The conversion between Λ_η and σ_{p-air} for different simulation models. 72
3.30 The PAO σ_{p-air} compared with different model predictions. 73
4.1 Example of a double-bump shower profile. 76
4.2 Schematic diagram of the spherical shower front. 77
4.3 Schematic diagram of a double shower front geometry. 78
4.4 The shower plane time residual distribution. 79
4.5 The shower plane time residual of SD event. 80
4.6 Simulated FADC traces showing the muonic and EM component. 81
4.7 The first peak time bin position distribution. 82

4.8 Peak finding example. 83
4.9 Separation of FADC trace peaks. 84
4.10 SD double shell events demonstration. 85
4.11 Example of calculation of the shower profile start point. 86
4.12 Shower radius of curvature and distance from shower start point to ground. . 87
4.13 Converting the calculated shower curvature to the shower longitudinal profile. 88
4.14 Distribution of the shower ages corresponding to the fitted radii of curvature. 89
4.15 The ratio of the shower size to the shower maximum distribution. 90
4.16 ΔX distribution. 92
4.17 Modified ΔX distribution. 93
5.1 FADC trace jump fitting results. 96
5.2 Muon signal is overwhelmed by EM signal close to the shower core. 98
5.3 Different muon counting methods example. 100
5.4 Sum of the jump signal size correlation result with true muon number. . . . 101
5.5 Number of jumps-plus-drops correlation result with true muon number. . . . 102
5.6 Sum of jumps-plus-drops signal size correlation result with true muon number. 103
5.7 Number of peaks correlation result with true muon number. 104
5.8 Sum of the peaks signal size correlation result with true muon number. . . . 105
5.9 Difference between sum of the jump signal size and true muon number. . . . 106
5.10 Difference between number of jumps-plus-drops and true muon number. . . . 106
5.11 Difference between sum of jumps-plus-drops signal size and true muon number. 107
5.12 Difference between number of peaks correlation and true muon number. . . . 107
5.13 Difference between sum of the peaks signal size and true muon number. . . . 108
5.14 The correlation result of the sum of jumps-plus-drops signal (50 stations). . . 109
5.15 The correlation result of the sum of peaks signal (50 stations). 110
5.16 Difference result of sum of jumps-plus-drops signal (50 stations). 111
5.17 Difference result of sum of peaks signal (50 stations). 112

5.18 Comparison of PAO data and simulation (sum of jumps-plus-drops signal). . 113
5.19 Comparison of PAO data and simulation (sum of the peak signal). 114

Abstract

Although cosmic rays were discovered exactly one century ago, the most fundamental questions about them are still not answered, especially the origin and composition of ultra-high energy cosmic rays (UHECR). The Pierre Auger Observatory (PAO) is constructed with the goal of solving these mysteries. The PAO uses hybrid design and take advantage of both the air fluorescence and surface array technique. Since its debut in 2004, PAO has published several important scientific results.

The most probable candidate for UHECR composition is proton or iron nucleus. The two candidates do show differences in both fluorescence detector (FD) signal and in the surface detector (SD) signal. PAO has utilized the statistical depth of shower maximum (X_{max}) information of FD signal to study the composition and suggests that the nuclear mass is getting heavier from 10^{18} eV to 10^{19} eV and beyond. The result does not come without argument. The Telescope Array (TA)'s result consists with a pure proton primary. One other possible solution to check these results is to study the SD signal since SD has a lot more statistics. According to Matthews' Heitler model, the proton and iron primary air showers show significant differences in the muon production, thus muon number is very sensitive to the cosmic ray primary composition.

"Leading particle" physics - where one of the many particles emerging from a collision carries a significant portion of the energy - is a well-known and studied concept in high energy physics. It gives a lot of information about the hadronic interaction and yet to be studied in highest energies levels. It has two observables, a "double bump" longitude profile in FD and a "double shell" geometrical structure in SD.

In this dissertation, I will describe new methods to identify leading particles and to count muons in air showers. These observations are then compared to simulations using several hadronic physics modeling schemes.

1. Introduction

Since their discovery in 1912, cosmic rays have played a very important role in particles physics and astrophysics. The study of cosmic rays in the first half of the 20th century led to several important discoveries about elementary particles. After the second world war, physics entered an age of man-made accelerators. A lot of breakthroughs have been made on accelerators. However, nature has always been able to overpower the human race. What humans view as big is small or even tiny for the universe. Multiple cosmic ray showers above 10^{20} eV events has been observed since 1960s, an energy which is thousands times more energetic than the Large Hadron Collider (LHC) [1] can produce. The LHC is the most expensive experiment to this date and this means the energy limit for man-made accelerators will probably hold for another few decades. That leaves ultra-high energy cosmic rays (UHECR) as the only possible way to study the physics at this energy range.

Through the last century of cosmic ray research, people have gained a good amount of knowledge of lower energy cosmic rays through direct measurement by balloons and satellite experiments. But scientists still know relatively little about UHECR because their rarity. The most basic questions include, what are they (the composition), where do they come from (the origin) and how do they get such enormous energy (the acceleration mechanism). The detection of UHECR requires huge exposures. The Pierre Auger Observatory (PAO) is the first experiment to make possible the collection of high statistics in this energy range in just a few years. The surface detector (SD) array of PAO, covering 3000 km^2, finished construction in 2008 and have been collecting huge amount of data since 2004. The SD is sensitive to both muons and electromagnetic (EM) particles created in the cosmic ray air showers. The signals are digitized by Flash Analog-to-Digital Converters (FADCs) providing important timing information.

PAO has published results on composition studies based on the depth of shower maximum (X_{max}) of FD shower profile. The results suggest the nuclear mass is getting heavier with

the increase of energy. However, the Telescope Array Collaboration (TA) in the north hemisphere has a different conclusion, reporting that the composition is consistent with proton primaries [2]. Another way to check these results is to use the SD data which have a lot more statistics. Based on Matthews' simplified Heitler Model, iron primary showers would produce a significantly larger amount of muon signal than proton showers with the same energy. If we can identify the muon signals from the EM background, then we can compare the PAO data with simulations and study the trend of the composition.

Another important physics concept is called "leading particle physics". A secondary particle from the first cosmic ray interaction carries a significant fraction of the primary energy and may travel a long way before creating a large secondary shower with a shower size that is comparable to the primary one. This will look like two well separated showers that overlaying each other. If we can identify these events, we can learn more about the first interaction thus enabling us to study hadronic physics at highest energy levels.

The aim of this dissertation is to study the hadronic physics at the highest energy level and to study new ways to do composition research with the PAO SD data. Chapter 2 introduces the history and physics of cosmic rays. It summarizes our current knowledge and theories about cosmic rays. Chapter 3 gives a detailed description of the PAO, including the design and event reconstruction of FD and SD and the recent scientific results PAO published. In Chapter 4, we introduce the peak finding method that is used to find the SD timing information of a possible second shower front. "Jump", "Drop" and "Peak Finding" methods are used to find quantities that correlate with the muon number of the simulation. These methods and the comparison between PAO data and simulations are described in Chapter 5. Finally, the summary and outlook of this dissertation are presented in Chapter 6.

2. Ultra-High Energy Cosmic Ray Physics

2.1 History

At the beginning of 20th century, scientists were puzzled by the origin of atmospheric background radiation. In 1912, V. Hess [3] bravely took several brave balloon flights up to 5000 m and found that the ionization level in the atmosphere increase with the altitude. He concluded that the radiation must come from outer space. The name "Cosmic Rays" was first used by influential American physicist R. Millikan, who is famous for his oil drop experiment that calculated the charge of an electron. He suspected the cosmic rays to be gamma rays, the most penetrating particles known at that time. Hess was awarded the Nobel Prize in 1936 for the discovery of cosmic radiation. Since then, cosmic ray studies have become an important part of both particle physics and astrophysics and led to the important discoveries of positrons [4], muons [4] and pions [5].

In 1938, P. Auger and R. Maze furthered the investigation of cosmic rays by doing an experiment at high altitude [6]. They used Wilson chambers and Geiger-Muller tubes separated by large distance to record the particle arrival timing. They found that the time coincidence still occur even for the tubes separated as far as 300 meters. They concluded from the result that these particles must be secondary showers initiated by a primary particle. Auger named this phenomenon "Extensive Air Showers", from which he calculated that, for one event example, the primary particle energy could be as high as 10^{15} eV, which was astonishing at a time when the most energetic particles produced in the laboratories had energies of a few MeV.

In 1963, J. Linsley reported the first 10^{20} eV cosmic ray event using the Volcano Ranch array [30]. This result was reported before the 2.7K cosmic microwave background radiation was known. The Volcano Ranch array was the first large scale surface array experiment that measured the cosmic rays at the highest energies. After that, this ground based particle de-

tection technique has been widely used world wide. The important projects include Haverah Park (UK) [29], SUGAR (Australia) [63], Yakutsk (Russia) [64], AGASA (Japan) [32] and Pierre Auger Observatory (Argentina) [67].

This high energy event reported by Linsley was a shock for the 1960s' physics community. Not long after that, in 1965, the cosmic microwave background (CMB) was reported by A. Penzias and R. Wilson [42]. Then, in 1966, K. Greisen [20], V. Kuzmin, and G. Zatsepin [21] independently predicted that cosmic protons above a threshold energy of 5×10^{19} eV would undergo photo-pion production on the CMB. This would lead to a cutoff feature in the energy spectrum termed "GZK cutoff", which would be describe later in Section 2.3.3.

An alternative detection technique was also proposed (by K. Greisen, among others), the fluorescence technique, to use the earth's atmosphere to be a huge detector [7]. Air fluorescence was first studied in the 1960s by the Los Alamos National Laboratory(LANL). In 1976, at the Volcano Ranch array, physicists from University of Utah detected air fluorescence signals, for the first time, confirmed by a ground array signal [38]. Inspired by the success, Fly's Eye Experiment [31], followed by HiRes [39] and now the Telescope Array [40], made full use of this technique. The combination of both the fluorescence technique and ground array is being used at Pierre Auger Observatory(PAO) and Telescope Array(TA).

2.2 Energy Spectrum

After 100 years of study with many experiments, the overall cosmic ray energy spectrum has been well-measured up to energies near 10^{19} eV. The spectrum is observed to be a power law [27]:

$$dN/dE \sim E^{-\alpha} \tag{2.1}$$

where the index α is roughly 3, which means that the flux of cosmic rays above a given energy will decrease by a factor of 100 for every higher energy decade. For example, the flux of cosmic rays is about $1/\mathrm{m}^2$/second above 100 GeV, but decreases to $1/\mathrm{km}^2$/century above 10 EeV.

The index α changes slightly with the energy. At lower energies, it is about 2.7, but at around 3×10^{15} eV, the index increases to 3, this energy is called: the "knee". Then at about 10^{19} eV, the slope changes back again to 2.7, this energy is called: the "ankle" (see Figure 2.1 for details).

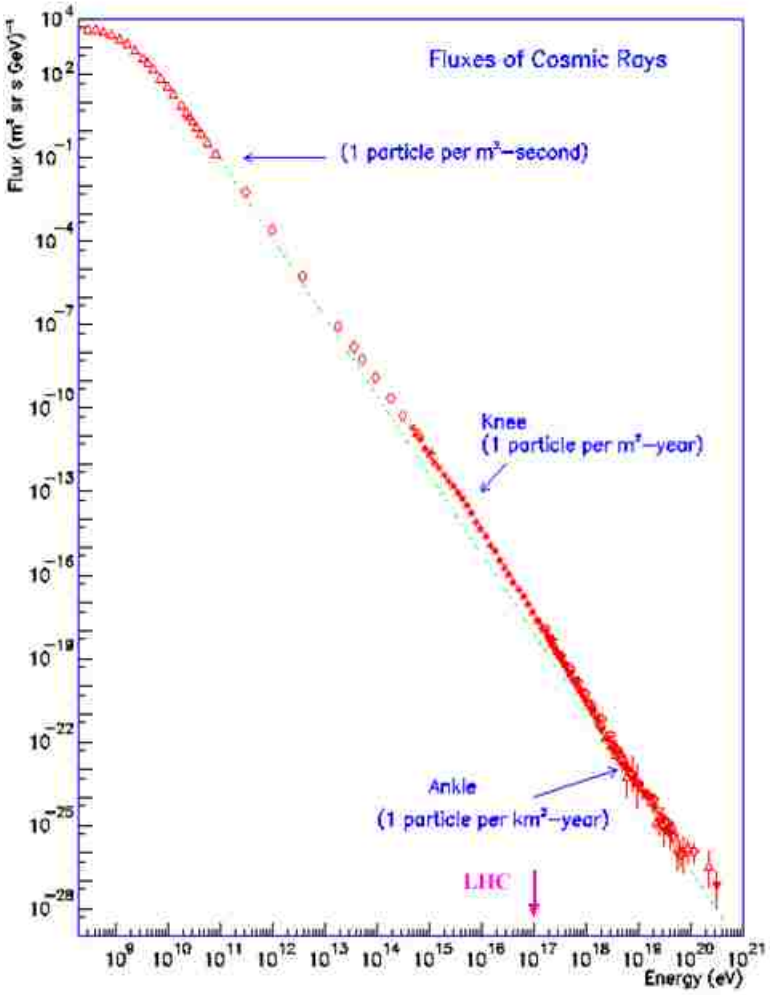

Figure 2.1: Observed energy spectrum of cosmic rays from 10^8 eV to 10^{21} eV [41]. The spectrum follows a power law with an index roughly -3. The equivalent laboratory energy of the CERN Large Hadron Collider (the largest man-made accelerator) is marked with a purple arrow.

2.3 Origin and Propagation

Up to the "ankle", the cosmic rays are believed to have a mainly galactic origin. But beyond that energy, scientists are still puzzled by the origin of UHECR. Theorists have many models for experimentalists to check [44]. It is well recognized that anything that can accelerate cosmic rays to a energy as high as 10^{20} eV must be extremely large.

2.3.1 Sources and Acceleration

Two popular model categories exist to explain why cosmic rays get such high energies: "bottom-up" models and "top-down" models. Bottom-up models propose that the particles are created at lower energies but accelerated somehow to higher energies. Top-down models say that particles are created at the high energies in the first place. For bottom-up models, there are two ways that a particle can gain momentum, either by direct acceleration by an electromotive force(EMF) or by the diffusive shock acceleration (Fermi acceleration). Diffusive shock acceleration was first proposed by Fermi in 1949 to explain the origin of the cosmic rays [43]. He suggested that it is possible when a charged particle is repeatedly reflected in the moving plasma, the particle on average will gain energy.

The original theory of Fermi acceleration can be depicted with Figure 2.2 [45]. A cosmic ray entering in a massive moving plasma with a initial energy of E_1 and momentum of P_1. The plasma moves at a speed of V. The energy difference can be calculated by using the Lorentz transformation between the laboratory frame and the plasma frame. The energy at the plasma frame $E_1^{'}$ is

$$E_1^{'} = \gamma E_1(1 - \beta \cos\theta_1) \tag{2.2}$$

where $\beta = V/c$ and $\gamma = 1/\sqrt{1-\beta^2}$ is the common Lorentz factor.

After bumping around in the plasma, it exits with energy of E_2 and momentum of P_2. Back in the laboratory frame, the energy E_2 is

$$E_2 = \gamma E_2^{'}(1 + \beta \cos\theta_2) \tag{2.3}$$

where the $E_2^{'}$ is the cosmic ray's energy before it escapes the plasma and θ_2 is the angle between the exit particle and the moving direction of the plasma.

In the magnetic field of the plasma's rest frame, there will be no change in the energy, so we have $E_2^{'} = E_1^{'}$. From equation 2.2 and equation 2.3, we can calculate the fractional energy change to be

$$\frac{\Delta E}{E} = \frac{E_2 - E_1}{E_1} = \frac{1 - \beta\cos\theta_1 + \beta\cos\theta_2^{'} - \beta^2\cos\theta_1\cos\theta_2^{'}}{1-\beta^2} - 1 \tag{2.4}$$

The plasma is massive and the cosmic ray will be bumping around inside the plasma multiple times, causing the distribution of the exit angle to be fairly uniform, so we have an average value of $\cos\theta_2^{'}$ as

$$\langle cos\theta_2^{'}\rangle = 0 \tag{2.5}$$

As can be seen from Figure 2.2, the average value of $\cos\theta_1$ depends on the rate at which cosmic rays collide with the plasma at different angles. The rate depends on the relative speed of the the cosmic rays and the moving plasma. So for UHECR, which have a speed very close to the speed of light ($v \simeq c$), we have the rate as

$$\frac{\mathrm{d}P}{\mathrm{d}\Omega_1} \propto v - V\cos\theta_1 \simeq (1 - \beta\cos\theta_1) \tag{2.6}$$

The average of $\cos\theta_1$ can be calculated as

$$\langle\cos\theta_1\rangle = \frac{\int \cos\theta_1 \frac{\mathrm{d}P}{\mathrm{d}\Omega_1}\mathrm{d}\Omega_1}{\int \frac{\mathrm{d}P}{\mathrm{d}\Omega_1}\mathrm{d}\Omega_1} = -\frac{\beta}{3} \tag{2.7}$$

Since the plasma speed is much slower($V \ll c$), we have $\beta \ll 1$. Substitute equation 2.5 and equation 2.7 into equation 2.4, we now have the energy change of the second order Fermi acceleration to be

$$\frac{\langle\Delta E\rangle}{E} = \frac{1+\beta^2/3}{1-\beta^2} - 1 \simeq \frac{4}{3}\beta^2 \tag{2.8}$$

From equation 2.8, we can see that the energy change is small (second order in β) but positive.

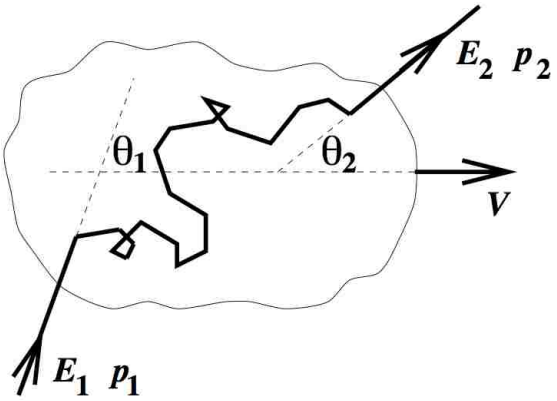

Figure 2.2: Schematic diagram of second order Fermi acceleration. From [45].

There is another more efficient way to accelerate the particle. In the 1970's, (Axford, Lear and Skadron 1977 [46], Krymsky 1977 [47], Bell 1978 [48], Blandford and Ostrkier 1978 [49]) modified Fermi's theory and described a first order in β energy gain in super nova shocks. We will use Figure 2.3 for a simplified calculation.

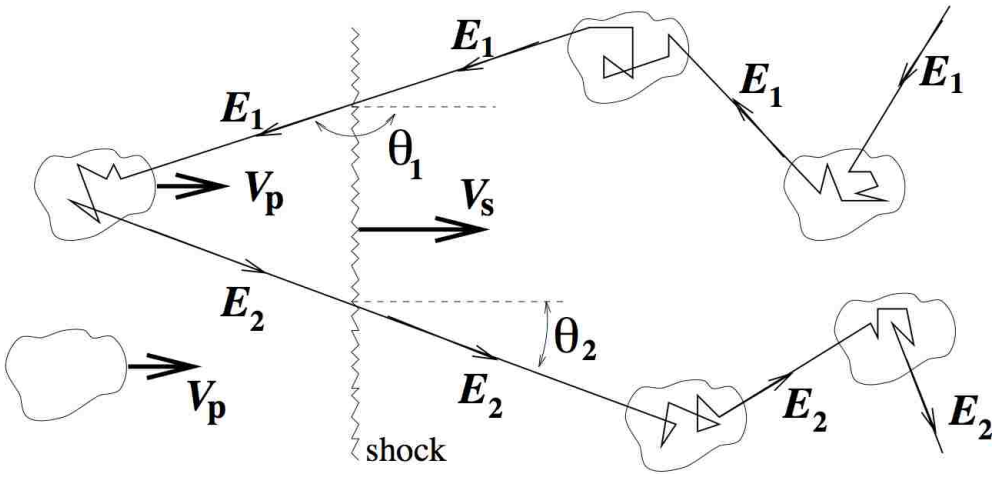

Figure 2.3: Schematic diagram of first order Fermi acceleration. From [45].

During a classic supernova explosion, the ejected masses is moving at a speed of $V_P \sim 10^4$ km/s, much faster than the speed of sound in the interstellar medium (ISM), which is 10 km/s. The shock velocity V_S has a relation with the ejecta velocity V_P of

$$\frac{V_S}{V_P} \simeq \frac{R}{R-1} \tag{2.9}$$

where R is the compression ratio.

By considering the rates of cosmic rays crossing the shock from downstream to upstream and from upstream to downstream, the average value of the cosine is $\langle \cos\theta_1 \rangle = -2/3$ and $\langle \cos\theta_2' \rangle = 2/3$. Substitute these two values to equation 2.4, the first order Fermi Acceleration at supernova and other shocks are

$$\frac{\langle \Delta E \rangle}{E} = \frac{1 + \frac{4}{3}\beta + \frac{4}{9}\beta^2}{1 - \beta^2} - 1 = \frac{\frac{4}{3}\beta + \frac{13}{9}\beta^2}{1 - \beta^2} \simeq \frac{4}{3}\beta \tag{2.10}$$

considering that $\beta = \frac{V_P}{c} \sim \frac{1}{30} \ll 1$.

Sources can only accelerate particles to some maximum energy before the particles escape from them. The maximum energy of the particle can be estimated as

$$\left(\frac{E_{max}}{\mathrm{EeV}}\right) = \frac{1}{2}\,\beta\, Ze \left(\frac{\mathrm{B}}{\mu\mathrm{G}}\right)\left(\frac{\mathrm{R}}{\mathrm{kpc}}\right) \tag{2.11}$$

where Ze is charge of the particle, B is strength of the magnetic field and R is the size of the acceleration source. The galaxy itself does not have the sufficient magnetic field and size to accelerate the UHECR. In 1984, M. Hillas pointed out that only a few astrophysical sites are capable of accelerating cosmic rays to energy as high as 10^{20} eV [8], see Figure 2.4.

Some plausible sources are listed here:

1. Active Galatic Nuclei (AGN)

   AGN are among the most discussed sources for UHECR because they have the size and strength to be perfect candidates. They are responsible for the enormous luminosity and electromagnetic field for the host galaxies. Typical AGN cores have sizes on the order of 10^{-5} pc and a magnetic field around 10^3 G, which is sufficient to contain a proton up to 10^{20} eV. Similarly, the AGN jets, having sizes around 10^{-2} pc and magnetic fields around 5 G, are also capable of accelerating protons to such energies [10]. However, the model of AGN predicts that heavy nuclei would have a hard time escape the central engine because of their interaction with ambient photons. Consequently the particles from AGN are more likely to be protons [9].

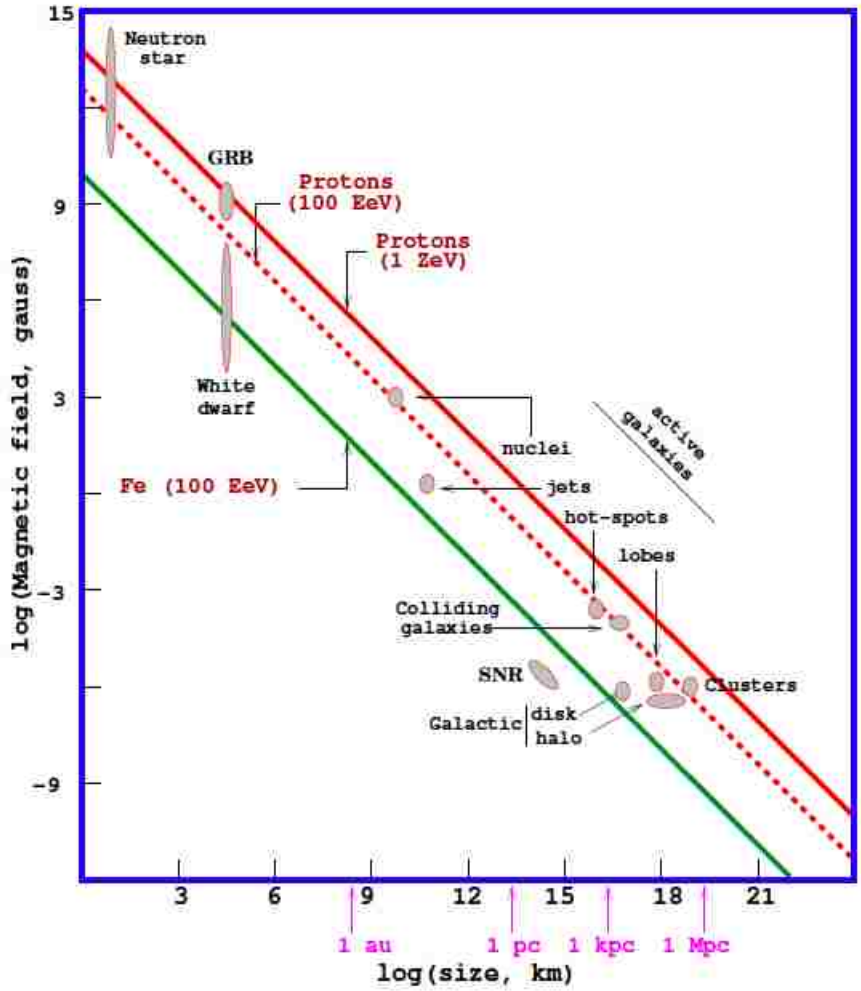

Figure 2.4: The Hillas plot showing the size the magnetic field strength of the possible sites for UHECR accelerations. The candidates below the three diagonal line (top to bottom), derived from equation 2.11, can not accelerate protons above 10^{21} eV, above 10^{20} eV and iron nuclei above 10^{20} eV, respectively. From [17].

2. Radio Galaxies

   Radio galaxies are a class of active galaxies that send very strong signals at radio wavelength. Typical radio galaxies have a size in the order of $10^3 \sim 10^6$ pc and a magnetic field of $10 \sim 10^3\,\mu$G [10]. They have the potential to accelerate particles up to 10^{21} eV. One famous radio galaxy is Centaurus A, which is also the nearest radio galaxy to earth.

3. Gamma Ray Bursts (GRB)

GRB are observations of a series of strong bursts of gamma-rays originating in the distant universe. They are the brightest electromagnetic events known in the universe. The connection of GRB to UHECR was first suggested by E. Waxman [11], M. Vietri [12] and M. Milgrom and V. Usov [13] in 1995. The duration of GRB varies from a few milliseconds to hundreds of seconds, releasing energy in the range of 10^{49} to 10^{53} ergs [18] [19]. This enormous energy is carried by an ultra relativistic wind with a Lorentz factor of order 100, enough to power Fermi acceleration of particles up to 10^{20} eV [11].

2.3.2 Magnetic Field

During their long travel to the earth, charged UHECR will be deflected by intervening magnetic fields along their trajectory. The strength of the intergalactic magnetic field is constrained to lower than 10^{-9} G [14] [15]. Recently, A. Taylor et. al. further constrain the strength of extra galactic magnetic field above 10^{-15} G with GeV-TeV observation of blazers with Fermi telescope [50]. The Galactic Magnetic Field (GMF) has a typical value of a few μG over an extent of a few tens of kpc [15] [16]. There are several different models [52] for the structure and direction of the GMF. Figure 2.5 shows two model examples.

Deflections arising from GMF could have a big impact on the arrival direction of the cosmic rays on earth, especially the ones with larger charge. Iron nuclei typically have much larger deflection angles than do protons. Figure 2.6 displays the simulated trajectories within the BSS-S GMF model.

2.3.3 GZK Cutoff

Because of the existence of the cosmic microwave background radiation (CMB), when cosmic rays surpass a certain energy, they will interact with the CMB photons, creating new particles and losing energy. This process limits the number of particles to go beyond certain energy and leads a cut off feature in the cosmic ray energy spectrum. This phenomenon is called GZK cut off, which was predicted independently by Greisen [20] and Zatsepin and Kuzmin [21] in

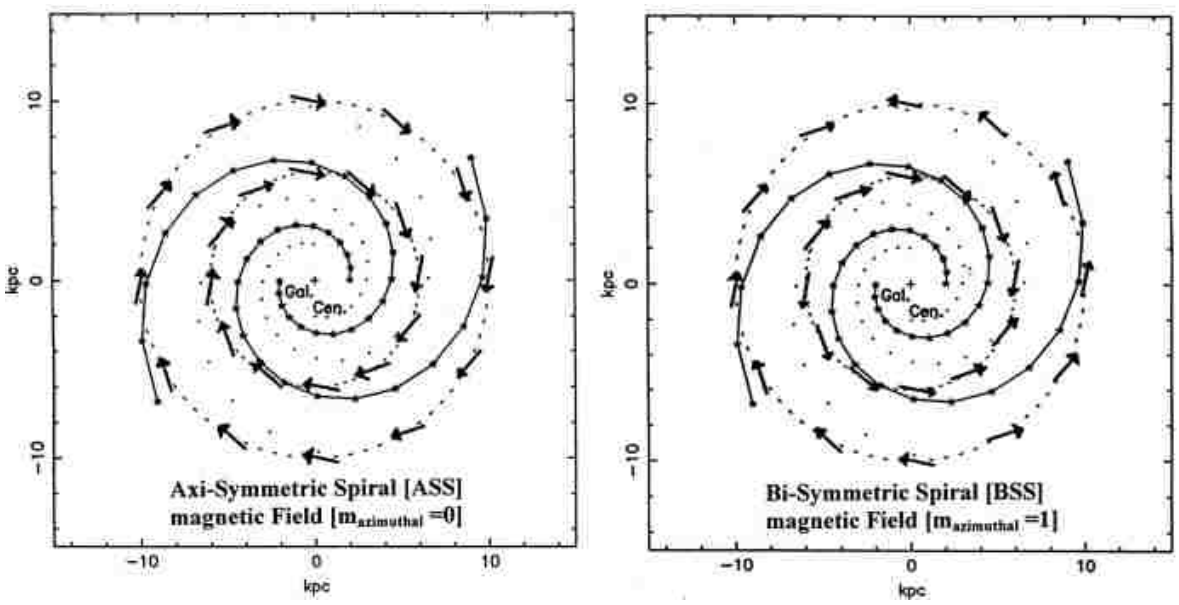

Figure 2.5: Schematic diagram of different Galactic Magnetic Field (GMF). The arrows are the direction of the magnetic field. The continuous curves with the star are the two spiral arms. Left: axisymmetric spiral (ASS) magnetic field. Right: bisymmetric spiral (BSS) magnetic field. From [52].

1966.

The interaction for protons, for example, is

$$\begin{aligned} p + \gamma_{cmb} &\rightarrow p + \pi^0 \\ &\rightarrow n + \pi^+ \end{aligned} \tag{2.12}$$

The threshold energy can be calculated. The objective is to calculate the threshold energy for this interaction to happen, so we want to consider a head-on collision scenario, which requires minimum proton energy. In the case of the neutral pion produced by the proton and CMB photons, by making $c = 1$ and considering $E^2 = m^2 + p^2$, the four momentum before the collision in the laboratory frame is,

$$\begin{aligned} s_{before} &= (q_\gamma + q_p)^2 \\ &= (E_\gamma + E_p)^2 - (\vec{p}_\gamma + \vec{p}_\gamma)^2 \\ &= {m_\gamma}^2 + m_p^2 + 2\,E_\gamma\,E_p - 2\,\vec{p}_\gamma\,\vec{p}_p \end{aligned} \tag{2.13}$$

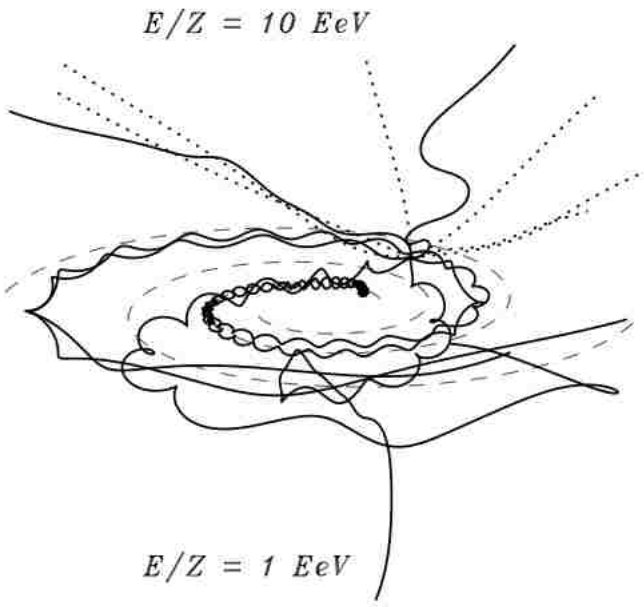

Figure 2.6: Simulated trajectories of nuclei with E/Z = 1 EeV (solid lines) and 10 EeV (dotted lines) in the BSS-S GMF model. From [53].

Since the mass of photon $m_\gamma = 0$ and the protons are moving relativistically($E_p \gg m_p$), we can write

$$\vec{p}_\gamma \, \vec{p}_p \approx -E_\gamma \, E_p \tag{2.14}$$

Substitute equation 2.14 into equation 2.13, we have

$$s_{before} \simeq m_p^2 + 4 \, E_\gamma \, E_p \tag{2.15}$$

For the interaction to happen, we need at least the amount of energy equal to the rest energy of a final state proton + pion,

$$s_{after} = (m_p + m_\pi)^2 = m_p^2 + m_\pi^2 + 2 \, m_p \, m_\pi \tag{2.16}$$

Conserving of four-momentum gives $s_{before} = s_{after}$. using equation 2.15 and equation 2.16,

$$
\begin{aligned}
m_p^2 + 4\,E_\gamma E_p &= m_p^2 + m_\pi^2 + 2\,m_p\,m_\pi \\
\Rightarrow 4\,E_\gamma E_p &= m_\pi^2 + 2\,m_p\,m_\pi \\
\Rightarrow E_p &= \frac{m_\pi^2 + 2\,m_p\,m_\pi}{4\,E_\gamma}
\end{aligned} \tag{2.17}
$$

The average energy of a blackbody photon in the 2.7 k CMB is $E_\gamma \sim 6.34 \times 10^{-4}$ eV, the rest mass of proton is $m_p \simeq 938$ MeV/c^2 and the rest mass of pion is $m_\pi \simeq 135$MeV/c^2. Putting these values in equation 2.21, the threshold energy of the proton pion production as

$$
E_p = \frac{135^2 + 2 \times 938 \times 135}{4 \times 6.34 \times 10^{-4}} \times 10^{12}\text{eV} \simeq 1.07 \times 10^{20}\,\text{eV} \tag{2.18}
$$

Please note that this threshold value can be lower since the microwave spectrum extends to $\sim 10^{-3}$ eV (see Figure 2.7). A common statement of the threshold energy is $\sim 7 \times 10^{19}$ eV.

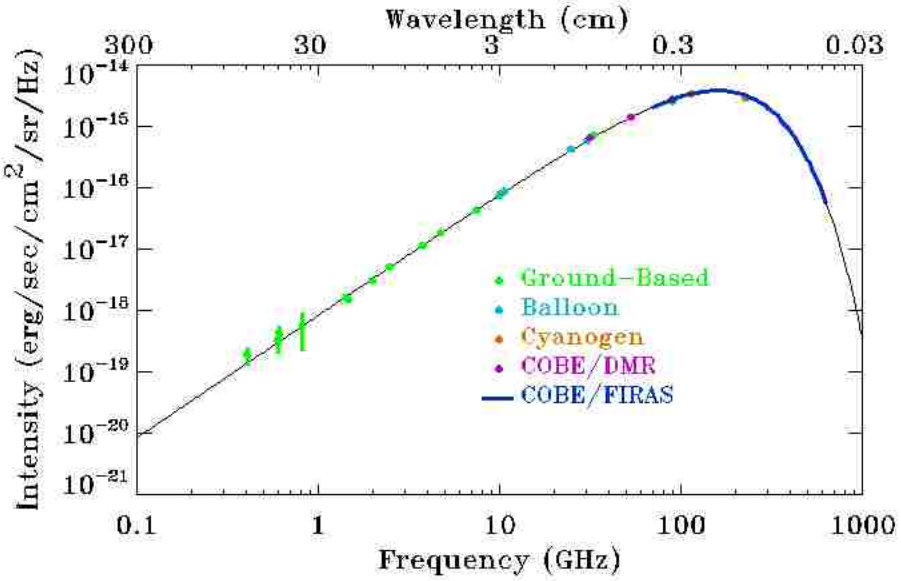

Figure 2.7: The intensity of the cosmic microwave background as a function of observing frequency (or wavelength). Courtesy NASA.

The main free path for the proton at 10^{20} eV can be estimated as

$$\lambda_{p\gamma} = \frac{1}{N\sigma_{p\gamma}} \approx 8\,\mathrm{Mpc} \tag{2.19}$$

where $N \approx 400cm^{-3}$ is the density of CMB photons and $\sigma_{p\gamma} \approx 100\,\mu b$ is the cross section for the proton-photon interaction at this energy. In each interaction, the proton loses about 20% of its energy, so this process will go on and on until the proton energy falls below the GZK threshold.

At lower energies, the proton may also lose energy due to Bethe-Heitler pair production.

$$p + \gamma_{cmb} \rightarrow p + e^+ + e^- \tag{2.20}$$

Following the similar method as equation 2.21, the threshold of the pair interaction can be found to be

$$\begin{aligned} m_p^2 + 4\,E_\gamma E_p &= m_p^2 + 4\,m_e^2 + 4\,m_p\,m_e \\ \Rightarrow 4\,E_\gamma E_p &= 4\,m_e^2 + 2\,m_p\,m_e \\ \Rightarrow E_p &= \frac{m_e^2 + m_p\,m_e}{E_\gamma} \\ \Rightarrow E_p &= \frac{0.51^2 + 938 \times 0.51}{6.34 \times 10^{-4}} \times 10^{12}\,\mathrm{eV} \simeq 7.55 \times 10^{17}\,\mathrm{eV} \end{aligned} \tag{2.21}$$

The energy loss of the process is very minimal compared to the photo-pion production, roughly $2m_e/m_p \approx 0.1\%$. The attenuation length for pair production is on the order of Gpc, see Figure 2.8 for details.

Neutrons are usually not accelerated in the UHECR sources since they have no charge. They are generated in the proton-pion production and either interact with CMB photons or decays into protons, neutrinos and electrons. Their interactions with the CMB photons are very similar to the protons [35],

$$\begin{aligned} n + \gamma_{cmb} &\rightarrow n + \pi^0 \\ &\rightarrow p + \pi^- \end{aligned} \tag{2.22}$$

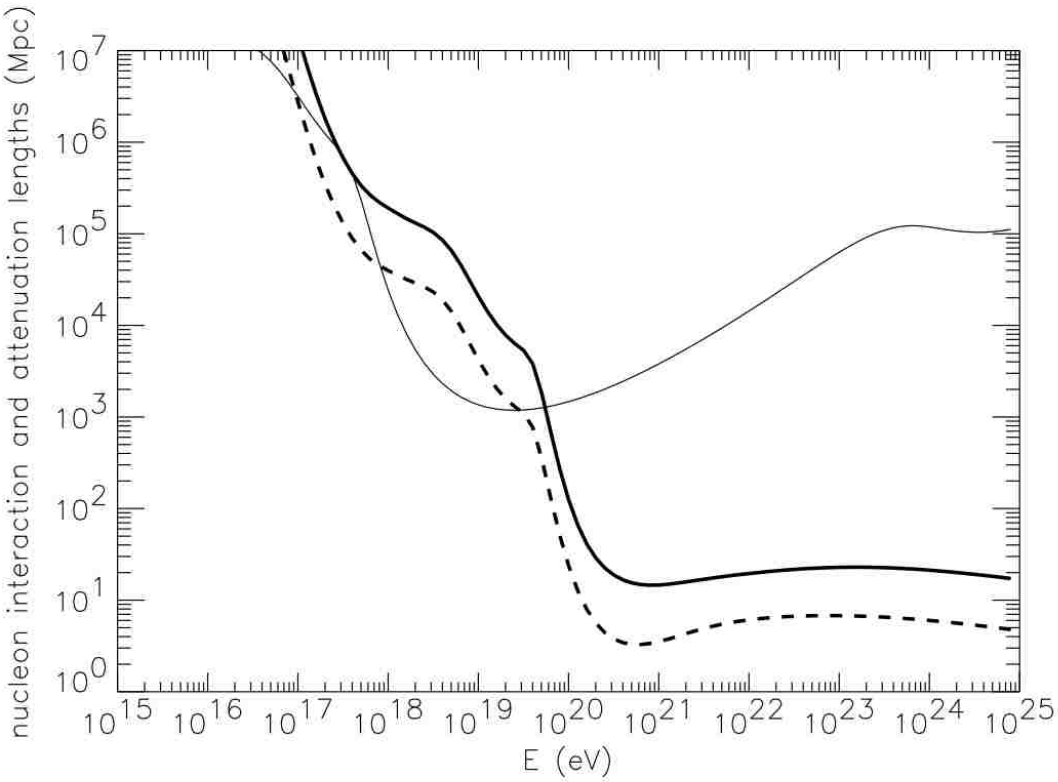

Figure 2.8: The nucleon interaction length (dashed line) and attenuation length (solid line) for photo-pion production and the proton attenuation length for pair production (thin solid line) in the combined CMB and the estimated total extragalactic radio background. From [55].

For heavier nuclei, the major energy loss processes include photo-disintegration in the CMB and infrared radiations (IR). They lose on average 3 to 4 nucleons per Mpc when their energy exceeds 2×10^{19} eV to 2×10^{20} eV depends on the IR background density [56]. Since their energy is shared between the nucleons, the energy threshold for heavier nuclei increases. The cross section also increases with nucleon number, consequently, the energy loss length is smaller for the heavier nuclei than protons. More details about heavier nuclei propagation can be found at [57].

2.4 Composition

The cosmic ray composition can be measured directly when the primary energy is below 10^{14} eV by placing detectors above the atmosphere due its relatively high flux. At these energies, cosmic rays components cover almost all of the elements in the periodic table, see Figure 2.9. About 79% of the nuclei are free protons, 15% helium and rest are electrons and heavier elements [54]. The common heavier elements (such as carbon, oxygen, magnesium, silicon, and iron) are present in very similar relative abundances as in the solar system, but there is a exceptional overabundance of the rare elements lithium, beryllium, and boron produced when heavier cosmic rays such as carbon, nitrogen, and oxygen disintegrate into lighter nuclei during collisions with the interstellar gas.

But for UHECR, on which this thesis is focused, their detection is another story. Since their flux is very low (the cosmic rays above 10^{20} eV have an estimated arrival rate at 1 per square kilometer per century), scientists need to rely on the air showers to measure the composition indirectly. This creates a huge challenge for us.

2.4.1 Composition of the UHECR

The composition of the highest energy cosmic rays is still not known at all. The most popular candidates are protons and iron nuclei as they have the largest binding energy. In other words, their probabilities of being broken during the long travel between galaxies are smallest. Muons in air showers play a big role in composition study, the physics is described in the Section 2.5. Neutrinos and photons are also possible candidates.

2.4.1.1 Neutrinos and Photons

Ultra-high energy neutrinos and gamma rays can be created as secondary particles from the decay of pions created during the GZK process (discussed in Section 2.3.3) or from "exotic" processes people may speculate about. Astrophysical photons have a relatively small range (< 10 Mpc at 10^{20} eV) because of pair production of e^+ and e^- on radio photon

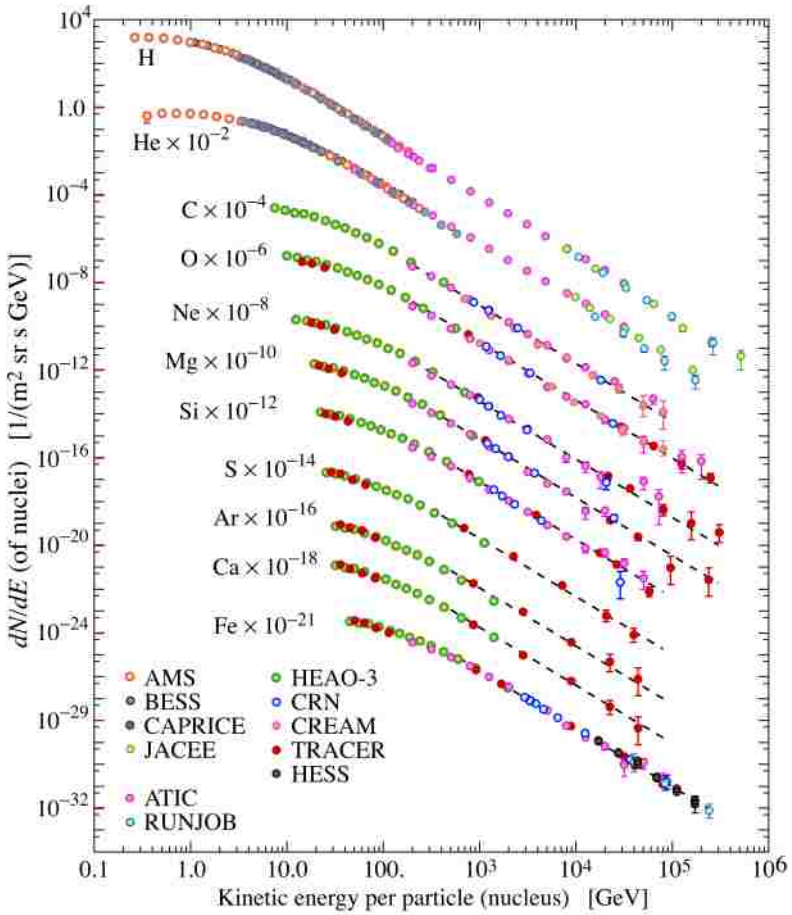

Figure 2.9: Primary composition of cosmic rays from 10^9 eV to 10^{14} eV, plot by P. Boyle and D. Muller. From [54].

background [59] but neutrinos can travel unhindered for a very large distance since they have very small cross sections. Limits on their fractions in the UHECR observations were both established in recent PAO results detailed in Section 3.6.

2.5 Extensive Air Showers (EAS)

Cosmic rays of lower energies are able to be detected directly from the ground or from balloon and satellite experiments, but for the ones with energies above 10^{15} eV , because of the very low flux (see Figure 2.1), physicists need to rely on Extensive Air Showers (EAS) (see Figure 2.10). EAS are created when a cosmic ray strikes the earth's atmosphere, interacts

with an atmospheric atom or molecule, and then creates a cascade of secondary particles. These particles, still with very high energies, will continually collide with other particles or decay, producing more particles until their energy falls below the threshold of creating more particles. Then the air shower starts to decrease in size.

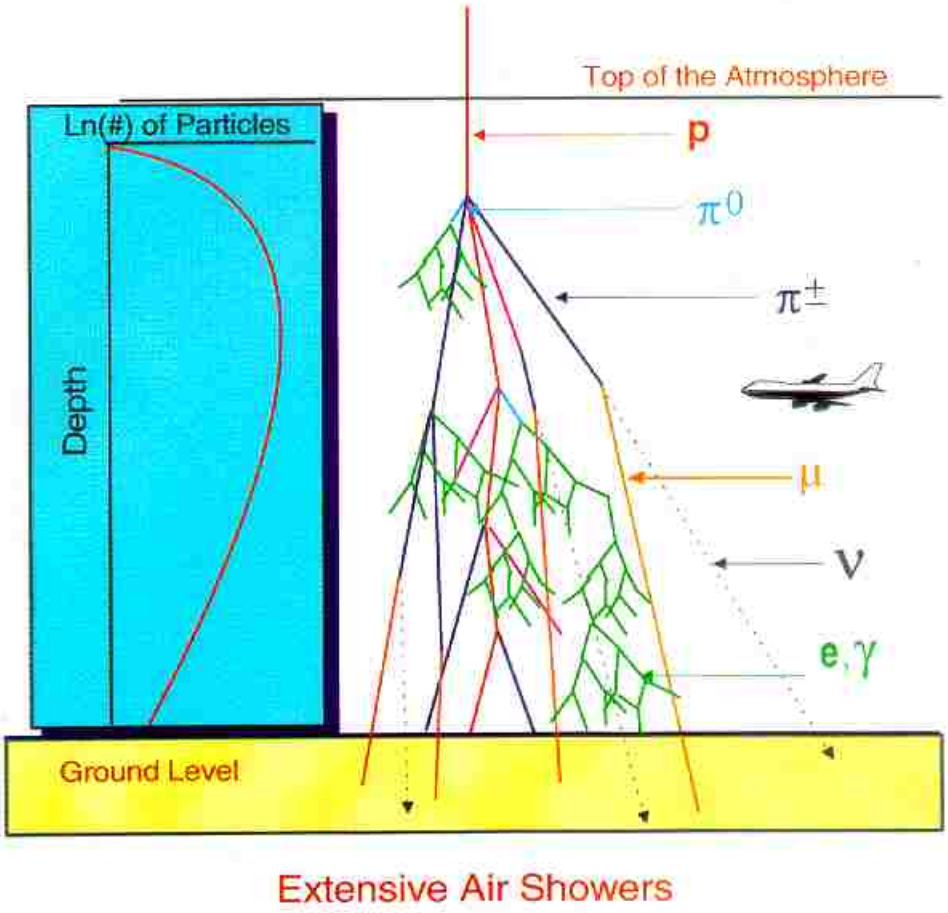

Figure 2.10: Schematic diagram of how EAS are formed, from the University of Adelaide astrophysics group website. Left, number of particles in EAS increase and decreases with the atmosphere depth. Right, the major interactions in the EAS.

Ultra-high energy cosmic rays (UHECR) are cosmic rays with energies above 1 EeV (10^{18} eV). In this energy region, using EAS seems to be the only possible way to study them. Since there is no direct measurement, this brings a great challenge for scientists trying to solve the mystery of the UHECR' origin and composition.

2.5.1 Physics of Air showers

The candidates for UHECR composition includes protons, heavier nuclei, photons and neutrinos (due to GZK process or directly produced at sources). They have different interactions when they interact with the atmospheric molecule, thus creating different type of showers. EAS have two components, electromagnetic showers and hadronic cascades. Figure 2.11 shows the schematic plot of these two EAS types.

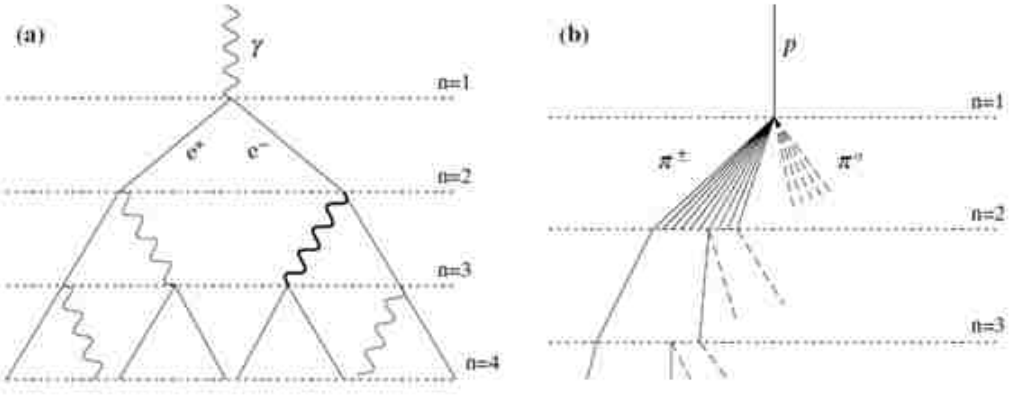

Figure 2.11: Schematic diagram of electromagnetic (a) and hadronic cascades (b). Right, the dashed line indicate neutral pions and the solid line indicates charged pions. From [34].

2.5.1.1 Electromagnetic EAS

The two major processes involved in Electromagnetic EAS is electron positron pair production and bremsstrahlung, see Figure 2.11 (a). When the high energy photons interact with an atmosphere nucleus, the photons convert themselves to electron positron pair, this process is called electron positron pair production.

$$\gamma + A \rightarrow e^+ + e^- + A \tag{2.23}$$

where A is an atmosphere nucleus.

The photons need to at least have an energy of $E_\gamma \geq 2\, m_e\, c^2 = 1.022$ MeV for this process to happen.

The electron or positron, if still with a very high energy, continues to travel. When it scatters, it will lose energy and emit a photon. This process is called bremsstrahlung.

$$e^{\pm} + B \rightarrow e^{\pm} + B + \gamma \tag{2.24}$$

where B is a charged particle in the atmosphere.

In 1954, W. Heitler presented a simplified model of electromagnetic EAS development in the atmosphere [33]. His assumption includes that every interaction has the same interaction length λ and every interaction loses half its original energy. Assume the cascade starts with a photon of energy E_0, then after length λ, the photon produces an electron and positron pair, each carrying half of its energy. After another (same) length, both the electron and positron emit a photon and lose another half its energy. After n steps, there are 2^n particles, each with an energy of $E_0/2^n$, see Figure 2.11 (a). This process will go on and on until the energy of individual $e^{\pm}$ and γ falls below the critical energy E_c. E_c for $e^{\pm}$ is where the electron energy losses from bremsstrahlung become smaller than those from ionization. In air, $E_c = 85MeV$ [34].

The number of particles at shower maximum N^e_{max} can be calculated as

$$N^e_{max} = E_0/E_c \tag{2.25}$$

and the depth of shower max X_{max} can be estimated as

$$X^{\gamma}_{max} = \lambda \ln(E_0/E_c) \tag{2.26}$$

The Heitler model suggests that in electromagnetic air showers, the maximum number of particles is proportional to the primary energy and the depth of shower maximum is proportional to the logarithm of the primary energy.

2.5.1.2 Hadronic EAS

For the hadronic air showers, the first interaction will start when the primary cosmic ray strikes an atmosphere nucleus in an inelastic collision, producing pions, kaons and a hadron

with significant fraction of the primary particle's energy. These secondary particles will continue to interact until they fall below the critical energy limit. High energy pions and kaons will likely interact before decaying since their Lorentz-dilated lifetimes are long. The neutral pions immediately decay into two photons,

$$\pi^0 \rightarrow \gamma + \gamma \tag{2.27}$$

thus providing the sources for electromagnetic cascades discussed above. The life time for π^0 is 8.4×10^{-17} s and the decay length is at the order of 25 nm. After their energies are reduced to about 10 GeV, most of the charged pions and kaons decay to muons and neutrinos with a fraction of kaons creating neutral pions to feed the electromagnetic showers [58].

$$\pi^{\pm} \rightarrow \mu^{\pm} + \nu \tag{2.28}$$

$$\begin{aligned} K^{\pm} &\rightarrow \mu^{\pm} + \nu \\ &\rightarrow \pi^{\pm} + \pi^0 \end{aligned} \tag{2.29}$$

The branching ratio for the charged kaons is 63.5% and 21.2%, respectively [58]. The two main decay modes of pions and kaons create the very important observable part of the air showers, the muon component. Muons have a relatively large interaction length and life time ($\sim 2.2 \times 10^{-6}$ s) and are sensitive to the composition of the primary cosmic rays, which will be explained in the following models. The neutrinos have very few interactions while carrying away significant amount of the primary energy.

In 2005, J. Matthews extended the original Heitler model from electromagnetic EAS to hadronic EAS [34] and thus enabling a quantitative estimate of the muon component difference from a proton initiated shower to a heavier nucleus. The sketch of this model is shown in Figure 2.11 (b). The model divides the atmosphere in layers of fixed thickness $\lambda_I \ln 2$, where λ_I is the interaction length of the strongly interaction particles. For pions in air, $\lambda_I \approx 120\,\mathrm{g/cm^2}$. The model also assumes λ_I to be a constant, which is a fairly good

approximation for interactions between 10 and 1000 GeV. The model simplifies the hadronic interaction process as follows: every hadron interacts after traveling one layer, producing N_{ch} charged pions ($\pi^{\pm}$) and $N_{ch}/2$ neutral pions (π^0). A π^0 decays to photons and initiates electromagnetic showers immediately. The $\pi^{\pm}$ will travel through another layer and interact. This process will go on and on until $\pi^{\pm}$ falls below critical energy E_c^{π} and decays to muons and neutrinos. E_c^{π} slowly decreases with the primary energy and the value used in this model is $E_c^{\pi} = 20$ GeV. N_{ch} is similar and the value used in this model is $N_{ch} = 10$, a value appropriate in the range from 1 GeV to 10 TeV.

Consider a proton entering in the atmosphere with a energy of E_0, after n atmospheric layers, there are $N_{\pi} = (N_{ch})^n$ total charged pions. Assume the energy is divided equally in all the pions produced, the charged pions carry $\frac{2}{3}$ of the total energy and the remainder $\frac{1}{3}$ goes into electromagnetic showers from the π^0 decay. The energy per charged pion after the nth interaction is

$$E_{\pi} = E_0 / \left(\frac{3}{2} N_{ch}\right)^n \tag{2.30}$$

The number of interactions before E_{π} falls below the critical energy E_c^{π} is

$$n_c = \frac{\log_{10}[E_0/E_c^{\pi}]}{\log_{10}[\frac{3}{2}N_{ch}]} = \frac{\log_{10}[E_0/E_c^{\pi}]}{\log_{10}[15]} = 0.85 \log_{10}[E_0/E_c^{\pi}] \tag{2.31}$$

From equation 2.28, we see that the number of muons is the same as charged pions during this process. So the primary energy can be estimated by the energy carried by pions and electromagnetic particles as

$$E_0 = E_c N_e^{max} + E_c^{\pi} N_{\mu} \approx 0.85 GeV (N_e + 24 N_{\mu}) \tag{2.32}$$

The importance of Equation 2.32 is that if N_e and N_{μ} are measured, the primary energy can be calculated regardless of the primary particle type and fluctuation.

From the result of equation 2.31, the number of muons created in the shower is obtained as

$$N_{\mu} = N_{\pi} = (N_{ch})^{n_c} = (N_{ch})^{0.85 \log_{10}[E_0/E_c^{\pi}]} = (E_0/E_c^{\pi})^{0.85} \approx 10^4 \left(\frac{E_0}{PeV}\right)^{0.85} \tag{2.33}$$

The number of electrons can be obtained as a function of primary energy as

$$N_\mu \approx 10^6 \left(\frac{E_0}{PeV}\right)^{1.03} \tag{2.34}$$

While the electrons are quite nearly proportional to the primary energy, the muon number is not. Higher energy showers will give more energy to the electromagnetic component as they develop more deeply into the atmosphere, at the expense of muon production. For the muon number in an iron primary shower, one can use the superposition model to approximate. The superposition model assumes the iron nucleus to be 56 protons with 1/56 of the primary energy and each proton interact independently. The muon and electron number of an iron primary shower can be roughly expressed as

$$\begin{aligned} N_\mu(Fe) &\approx 56 \times 10^4 \left(\frac{E_0/56}{PeV}\right)^{0.85} = 56^{0.15} N_\mu(p) \simeq 1.83\, N_\mu(p) \\ N_e(Fe) &\approx 56 \times 10^6 \left(\frac{E_0/56}{PeV}\right)^{1.03} = 56^{-0.03} N_e(p) \simeq 0.88\, N_\mu(p) \end{aligned} \tag{2.35}$$

The iron primary showers will have approximately 80% more muons and a little bit less electrons. If we identify the muon number accurately, we can estimate what the primary is or whether there is new physics involved in the highest energy cosmic ray showers.

To estimate the depth of the shower maximum X_{max}, the model further assumes only the neutral pions from the first generation contribute the electromagnetic component. The X_{max} for proton is estimated as

$$X^p_{max} = X_0 + \lambda \ln\left(\frac{E_0}{3\, N_{ch}\, E_c}\right) = \left[470 + 58\, \log_{10}\left(\frac{E_0}{PeV}\right)\right]\ \text{g/cm}^2 \tag{2.36}$$

where λ is the radiation length in the air and $X_0 = \lambda_I$ is the first interaction length of proton. The values of X^p_{max} is about 100 g/cm^2 or a bit less then $2\lambda_I$ shorter than the detailed simulation as we expected since the model assumptions ignore the contributions of the following sub showers.

2.5.2 EAS Detection Technique

Scientists currently have developed two techniques for the detection of EAS, one called Air Fluorescence detection, observing the emitted light as the EAS develops in the atmosphere,

the other named Surface Array detection, recording the final stage of the EAS on the ground. The Air Fluorescence technique was used by Fly's Eye experiment [31] and High Resolution Fly's Eye (HiRes) [65] experiment. The major experiments using surface array technique includes Volcano Ranch [30] in New Mexico, Haverah Park [29] in England, Sydney University Giant Air Shower Recorder (SUGAR) [63] in Australia, The Yakutsk experiment in Russia [64] and the Akeno Giant Air Shower Array (AGASA) [32] in Japan. The experiments built in the last decade, including Pierre Auger Observatory [67] and Telescope Array [66], are utilizing both techniques and doing hybrid measurements. More information about the running time and atmosphere depth of these experiments is shown in Table 3.1.

2.5.2.1 Air Fluorescence detection

When charged particles are created during the shower, they will interact with atmospheric nitrogen molecules and excite them. The excited molecules will emit fluorescence light mainly between 300 nm and 430 nm range. The number of fluorescence photons emitted, termed the air fluorescence yield, is proportional to the energy deposit of the shower particles. This process provides a measurable quantity for the EAS longitudinal development. However, the method is limited because its light emitted is so weak that the detector can only work on dark moonless nights. It should be noted this technique can only be used for the EAS with primary energies above 10^{17} eV since that is the energy limit for the telescope to distinguish showers from the night sky background. On the positive side, the measurement is a direct recording of the full shower development compared to the surface array technique.

The longitudinal profile of the extensive air showers (EAS) is often parameterized by the semi-empirical Gaisser-Hillas (GH) function, proposed in 1977 by T. Gaisser and A. Hillas [25].

$$N(X) = N_{max}\left(\frac{X - X_0}{X_{max} - X_0}\right)^{\frac{X_{max} - X_0}{\lambda}} \exp\left(\frac{X_{max} - X}{\lambda}\right) \tag{2.37}$$

where X is the atmospheric depth in g/cm^2 , $N(X)$ is the number of particle at depth X,

N_{max} is the maximum number of particles and X_{max} is the atmospheric depth where the shower reaches its maximum. The remaining parameters, λ and X_0 are fitted parameters that are correlated with the shower starting depth and attenuation after maximum. Figure 2.12 gives examples of two FD profiles fitted with GH function.

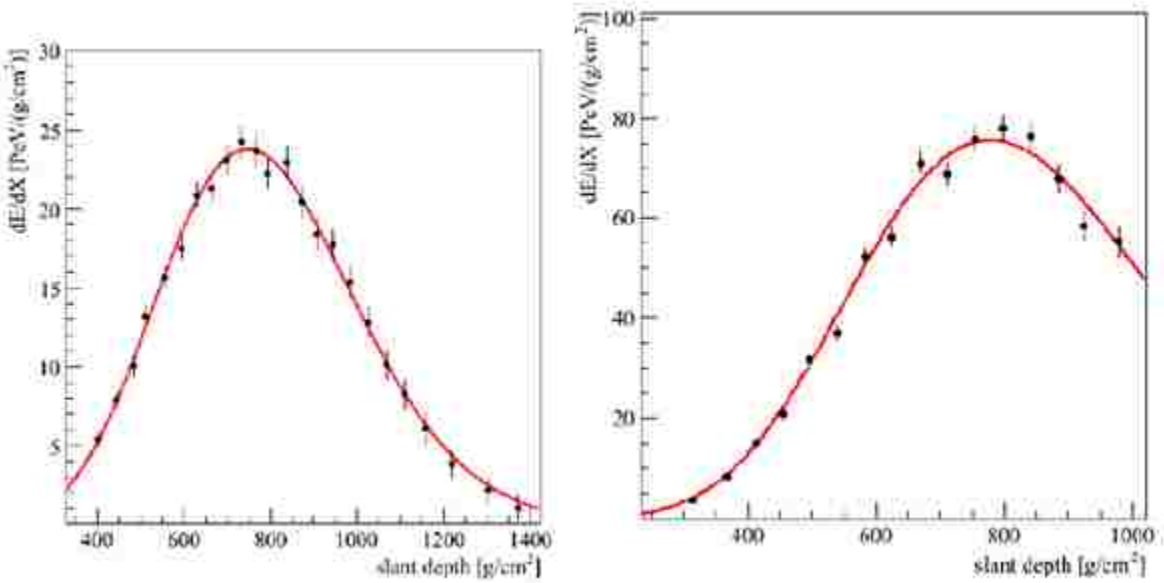

Figure 2.12: Examples of measured longitudinal profiles of high-energy showers. The black dots with error bars are the energy deposits and the red line are the fitted GH function. From [26].

The reconstruction of a fluorescence detector event starts from the calculation of the shower plane and shower axis, shown in Figure 2.13. This requires the knowledge of fluorescence efficiency, the absorption of the atmosphere, the quantum efficiency and gain of the photomultipliers.

We mark the time when light emitted at R_p reaches the detector as t_0. The time delay from the light reaching the ith photomultiplier at t_i to t_0 can be calculated as

$$\Delta t = t_i - t_0 = \frac{R_p}{c \sin\theta_i} - \frac{R_p}{c \tan\theta_i} = \frac{R_p}{c} \frac{1 - \cos\theta_i}{\sin\theta_i} = \frac{R_p}{c} \tan(\frac{\theta_i}{2}) \tag{2.38}$$

where c is the speed of light, θ_i is the angle between the shower axis and the light travel

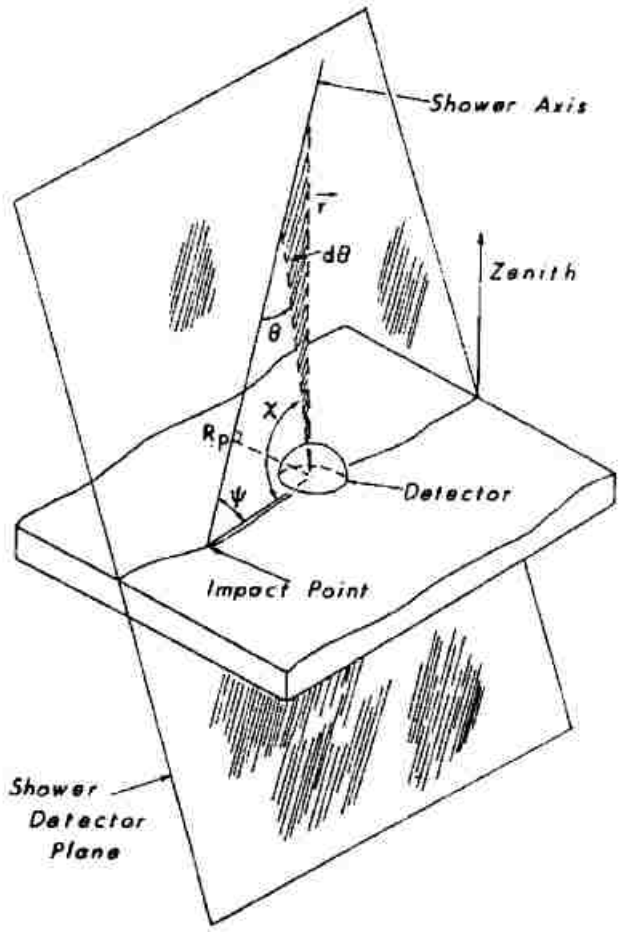

Figure 2.13: Schematic plot of EAS detection by a fluorescence detector, where R_p is the closet distance to the shower axis from the detector, χ is the observation angle, ψ is the incident angle. From [31].

path to reach the ith photomultiplier. It is related to ψ by

$$\theta_i = \pi - \psi - \chi_i \tag{2.39}$$

From the recorded data of t_i and χ_i (i form 1 to n for triggered photomultiplier), one can use χ^2 minimization of equation 2.38 to find the parameter R_p, t_0 and ψ, thus get the shower track geometry [59].

Once the shower geometry is determined, the expected fluorescence signal received by a photomultiplier can be calculated by the following equation,

$$S_\gamma = N_e \, Y_\gamma \, Q_e \, \frac{c \, \Delta t}{4 \, \pi \, r^2} \, \exp(-\frac{r}{r_e}) \, A \tag{2.40}$$

where N_e is the number of charged particles (mostly electrons) for each angular bin, Y_γ is the fluorescence yield, Q_e is the quantum efficiency for converting photons into photoelectrons, r is the distance from the source to the photomultiplier, r_e is the photon Rayleigh scattering extinction length and A is the optical gathering area of a mirror [59].

The background noise coming from the night sky background is,

$$N_\gamma = \sqrt{I_{bg}\,\Delta t\,A\,Q_e\,(\Delta\theta)^2} \tag{2.41}$$

where I_{bg} is the total sky noise coming from starlight, diffuse radiation from the galaxy, interplanetary scattered sunlight, photochemical atmospheric light, man-made light pollution [69]. From equation 2.40 and 2.41, the signal to noise ratio(SNR) is calculated as,

$$SNR = \frac{S_\gamma}{N_\gamma} = N_e\,Y_\gamma\,Q_e\,\frac{c}{4\,\pi\,r^2\,\Delta\theta}\,\exp(-\frac{r}{r_e})\,\sqrt{\frac{Q_e\,A\,\delta t}{I_{bg}}} \tag{2.42}$$

From this equation, we can see that in order to improve the SNR, one needs to build the detector with large collection area with small viewing angle and high quantum efficiency optics.

In certain cases, one EAS is seen by multiple fluorescence detectors. The shower geometry can be determined by the intersection of the shower plane without as much timing information from the detector. This will improve the accuracy of the event reconstruction.

2.5.2.2 Surface Array Detection

The surface array was the original way for the EAS detection when P. Auger discovered it in 1938 [6]. During the EAS development, the particle number increases and they will spread out from continuous cycles of decays, interactions and scatterings. The surface array technique takes advantage of that and uses water or plastic scintillators to record EAS's "foot prints" on the ground. When energetic particles from EAS pass through the water, they will emit Cherenkov light because they have larger speed than the light in that medium. The Cherenkov light can be collected with photomultipliers (PMT) inside the water tank. The collected signal is related to the particle density in that region. Different from air

fluorescence detection, the surface array, affected very little by the weather, can work with a 100% duty cycle.

Most surface array experiments arrange the detectors with equal space. The space d between the detectors depends on the target energy range; for UHECR, d is usually a few hundred to two thousand meters. Detectors are usually placed between an atmosphere depth between 800 g/cm^2 and 1000 g/cm^2 (sea level) as the average shower maximum is reached at around 750 g/cm^2. Figure 2.14 shows an example arrangement of detectors by Volcano Ranch experiment.

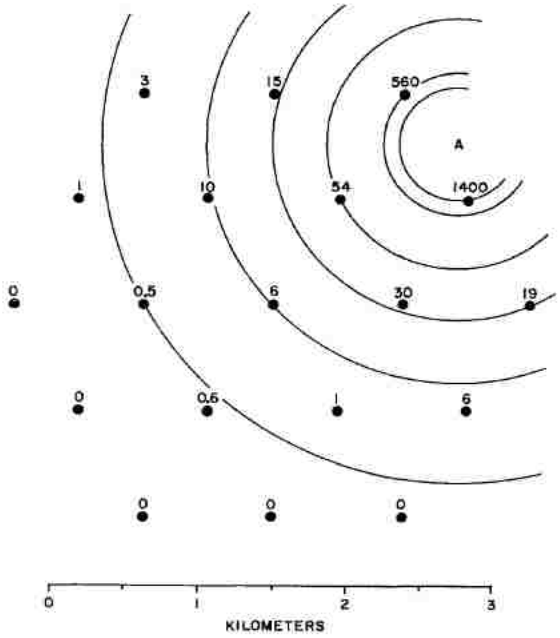

Figure 2.14: Volcano Ranch array surface detector position arrangement, showing the particle density map of the first 10^{20} eV event. From [30].

An important function, the lateral distribution function (LDF), is used to describe how the measured particle density changes with the distance away from the core. Quantitatively, this function can be described by Nishimura-Kamata-Greisen (NKG) function [60] [61].

$$f(\frac{r}{r_M}) = c(s)(\frac{r}{r_M})^{s-2}(1+\frac{r}{r_M})^{s-4.5} \tag{2.43}$$

where s is fitted and $c(s)$ is a normalization factor. Linsley, Scarsi and Rossi later modified

the function as [62]:

$$\rho_r = k(\frac{r}{r_M})^{-\alpha}(1+\frac{r}{r_M})^{-(\eta-\alpha)} \tag{2.44}$$

where ρ_r is the density of particles at distance r from the shower axis, r_M is the Molière radius (the product of one radiation length and the rms deflection of a particle of critical energy traversing one radiation length) [59], k is proportional to shower size and η and α is a fitting parameter to be determined empirically.

The shower core is calculated based on the timing, signal size of the detectors and fitting of the LDF. It is usually a chi-squared minimization or maximum-likelihood procedure. This quantity fluctuates significantly even for cosmic rays with the same energy and composition due to the inherent randomness of the first particle interaction. If the shower starts high in the atmosphere, shower particles will be more spread out. If the same shower starts deep in the atmosphere, the signal near the core will be very high, but with less shower spread. In 1970, M. Hillas suggested using the signal size of a detector at a certain distance away from the shower core as a energy estimator [68]. The purpose of this idea is to reduce the shower-to-shower fluctuation and minimize the dependence on the EAS primary and interaction model. The optimum distance r_{opt} depends on the detector array configuration and target cosmic ray energy range. For example, the AGASA experiment selects the distance to be 600m($S(600)$) [32] while PAO uses 1000m($S(1000)$) [67].

Based on the discussion in Section 2.5.1.2, different comic ray primary composition will lead to significant differences in the muon content detected at ground. With the ability to distinguish muon signal from EM background, the surface array is very important in composition studies. This is a focus of this dissertation and I will describe more details in Chapter 5.

3. Pierre Auger Observatory

3.1 Overview

The Pierre Auger Observatory (PAO) is constructed with the mission of solving the mysteries of the universe's highest energy particles. It is currently the largest cosmic ray observatory in the world. The project was first proposed by Jim Cronin and Alan Watson in 1992. It was proposed with two sites, Auger South near Malargüe, a small Argentine town at the foot of the Andes Mountains and Auger North in Colorado, USA. The Auger South site has finished construction in 2008 and has been collecting data since 2004. The Pierre Auger Collaboration is an international collaboration includes more than 490 scientists from 17 different countries.

The Pierre Auger Observatory is built on the successful experience of previous experiments and combines two independent detection techniques described in Section 2.5.2: the surface array detection and the fluorescence detection. Figure 3.1 shows a plan view of the Auger South site. The fluorescence detectors (FD) overlook the surface detector (SD) array which allows for energy and direction crosschecks, see Figure 3.2.

Table 3.1 below shows the location and running information of Auger South and other past or current experiments in the world.

3.2 The Surface Detector (SD)

The surface detector array uses 1600 water tanks covering 3000 km^2, 30 times the size of Paris. Table 3.2 shows a comparison between PAO SD with other past or current experiments.

Each tank is spaced 1.5 km from its nearest neighbors and contains over 3000 gallons of water. When energetic particles from the extensive air showers pass through the water in the tank, they emit Cherenkov light. The light is collected by three 9 inch photomultiplier tubes (PMT) inside the tank, converted to digital signals at 40 MHz by 10 bit Flash Analog-Digital

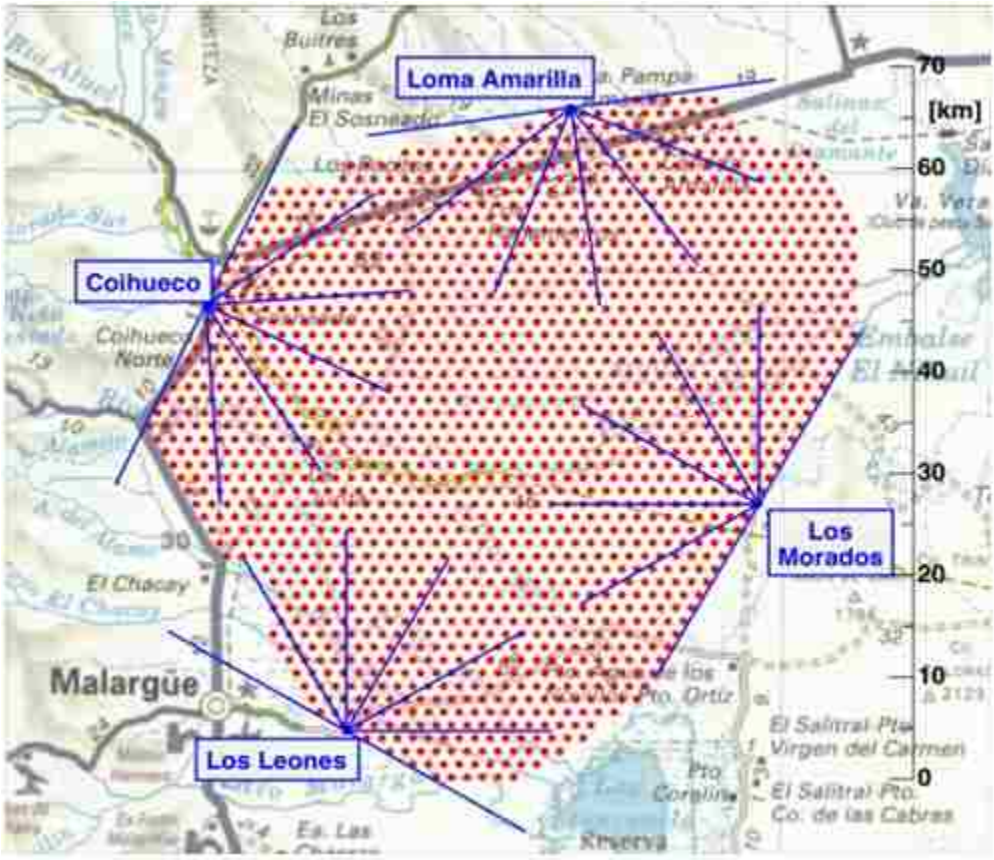

Figure 3.1: A map of Auger south site. Red dots are the surface detector tanks and the blue line shows the fluorescence telescopes pointing direction.

Table 3.1: The location and operation information of past and present experiments for ultra-high energy cosmic rays. Information from [22] [66].

Experiments	Locations	Begin (year)	End (year)	Altitude (m)	Atmospheric depth (g/cm^2)
Volcano Ranch	New Mexico	1959	1963	1770	834
SUGAR	Australia	1968	1979	250	1015
Haverah Park	England	1968	1987	200	1016
Yakutsk	Russia	1969	Running	105	1020
Fly's Eye	Utah	1981	1992	1372	860
AGASA	Japan	1990	2004	900	920
HiRes	Utah	1998	2005	1400	860
Auger South	Argentina	2004	Running	1420	880
Telescope Array	Utah	2007	Running	1400	860

Converters (FADC). The digital signals are then sent to the Central Data Acquisition System (CDAS) at the observatory central campus [23]. Figure 3.3 present a schematic overview of

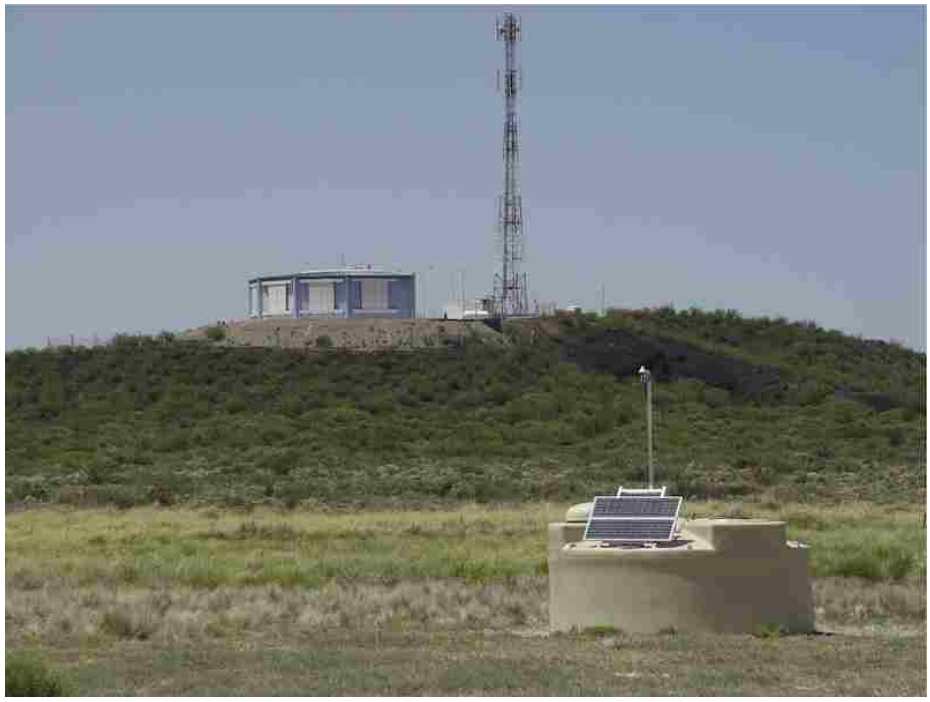

Figure 3.2: A surface detector overlooked by a fluorescence detector at Los Leones, one of the four locations of FD.

Table 3.2: Surface detector comparison from different experiments. Information from [22]. Yakutsk array rearranged around 1995 and the number in the table is the current number [59].

Experiments	Detector Type	Number of Detectors	Array coverage Area (km^2)
Volcano Ranch	Scintillator	19	8
SUGAR	Scintillator	47	60
Haverah Park	Water Cherenkov	34	12
Yakutsk	Scintillator	68	10
AGASA	Scintillator	111	100
Auger South	Water Cherenkov	1600	3000
Telescope Array	Scintillator	507	700

the surface detector design.

3.2.1 Surface Detector Design

The surface detector of PAO consists a cylindrical tank, 3.6 m in diameter and 1.55 m high. The water is highly purified to reduce the Cherenkov light attenuation. It is filled to 1.2 m high to absorb all the electromagnetic component and to optimize the muon pulse

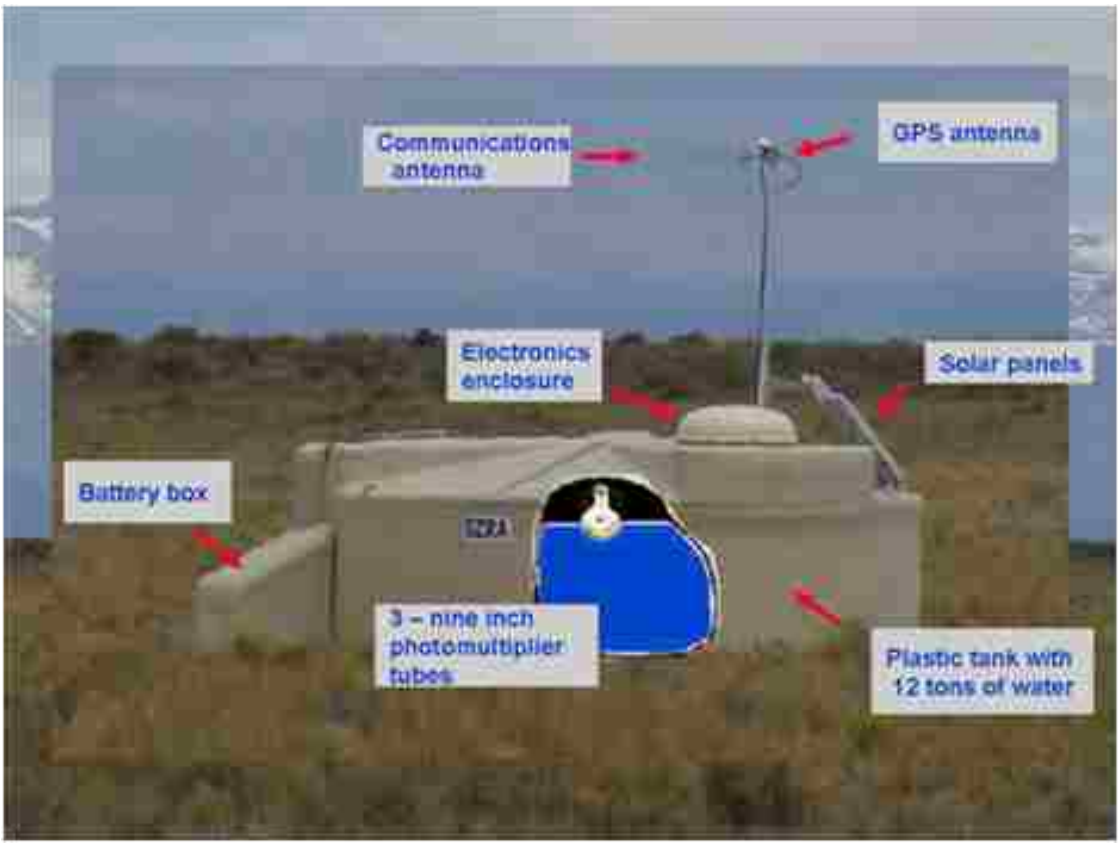

Figure 3.3: A schematic overview of the surface detector design.

amplitude. The tank is built with polyethylene that is strong enough to stabilize the solar panels in strong winds and to hold up to 3 people working on the top, yet durable enough for long term operation. It has a total thickness of 13 mm using two layers to resist the summer heating, winter ice formation and produce a perfect opacity. In side the inner layer, there is a cylindrical Polyolefin("Tyvek") bag, providing a 20 year seal of water, high reflectivity for the Cherenkov light, and acting as an additional barrier from external light source [70].

Three PMTs (9 inch Photonis XP 1805 model) are installed at the top of tank symmetrically at a distance of 1.2 m from the center [70]. Each PMT produces two signals: one directly from the the anode and the other provided by the last dynode amplified and inverted to 32 times the amplitude of anode signal. This configuration provides sufficient dynamic range to cover both the the strong signals close the shower core ($\sim$ 1000 particles/μs) and the weak signal far away from the shower core ($\sim$ 1 particles/μs). The signals are digitized

by 40 MHz 10 bit FADCs, which converts to 25 ns per FADC bin [23]. The PMT and electronics module are enclosed in a custom-molded plastic cover and sealed by clips and a silicone RTV gasket to protect the PMT from ambient light and environmental changes [70].

Each detector is operated autonomously with its own electronics and communication system powered by solar energy. The two 55 Wp solar panels provide sufficient power supply to the 24 V 10 W electronics system and for charging two 12 V 105 Ah battery for power storage. Power is expected to be available over 99% of the time [71].

3.2.2 Data Acquisition and Detector Calibration

The digitized signals from the three PMTs are sent by the radio communication system to a central data acquisition system (CDAS) once the signal meets the trigger conditions (Section 3.2.3). The bandwidth for the radio transmission is 1200 bits/s. Signals are measured in vertical muon equivalent(VEM), which is the average signal response when a single muon passes through the tank vertically. The detector itself cannot select vertical muons from other signals, but the random atmospheric muons produces a peak in the charge distribution, $Q_{\mathrm{VEM}}^{\mathrm{Peak}}$, which is proportional to the signal produced by a vertical through-going muon [23].

The calibration of the detector consists of timing and PMT calibration including the dynode to anode ratio calibration and the absolute calibration. The calibration is done locally and automatically, the parameters are determined with 2% accuracy and returned to CDAS every 60 s. The timing calibration is done by the GPS module and the time tagging board. GPS times are compared with the nearby stations. The PMT calibration includes three steps: [70].

1. The three PMTs are matched in gain by adjusting their voltages so that they would have the same rates above certain threshold. From the measurement of a test surface detector, the trigger rate above 3 VEM is about 100 Hz. Once a value for 1 VEM is chosen, the voltage then can be adjusted until the corresponding rate is 100 Hz.

2. On-line calibration, the evolution of the gains is monitored and stored in the data

transmitted to the CDAS. At first trigger level, we look at the rate of 3-fold coincidence above a threshold of 1.75 VEM. Once all the three PMTs are gain-matched, one expects all three will give the same rate of 70 Hz above a higher test threshold of 2.5 VEM. If one PMT has higher gain, the 3-fold trigger would not be affected significantly, whereas the individual rate would be higher than the other two. The local station controller can then adjust the VEM value to put all three PMTs at a similar rate above 2.5 VEM. The VEM value for each PMT is sent to CDAS for event reconstruction and other purposes. This value also provides a useful tracking tool once an error occurred.

3. The absolute calibration is determined by the measurement of the identical detector on the main campus of PAO. The value of 1 VEM is provided by a muon telescope with two scintillators placed both above and below the test detector. Overall, the calibrated stations have a precision of 5 %.

3.2.3 SD Tigger System

There are 5 trigger levels used by Auger surface detectors. The first two triggers are formed at the local detector because of the CDAS bandwidth limit. The T3 trigger starts the data acquisition and storage. The T4 and T5 triggers are offline triggers to ensure event quality. Figure 3.4 shows the logical relations between the first three triggers.

3.2.3.1 Local Triggers

The first trigger T1 allows the local data acquisition at the detector. The data is stored on local disk for 10 s for a possible T3 trigger. Two independent trigger modes are used. The first one, a simple threshold trigger (T1-TH), requires that the coincidence of the three PMT each above 1.75 $I_{\mathrm{VEM}}^{\mathrm{Peak}}$. This mode is used to collect signals that are narrow and large. The second mode, time over threshold trigger (T1-TOT), requires that at least 13 FADC bins (325 ns) in 120 bins (3 μs) are above 0.2 $I_{\mathrm{VEM}}^{\mathrm{Peak}}$ in coincidence of at least 2 PMTs in the detector. This mode is intended for nearby lower energy showers or far away high energy

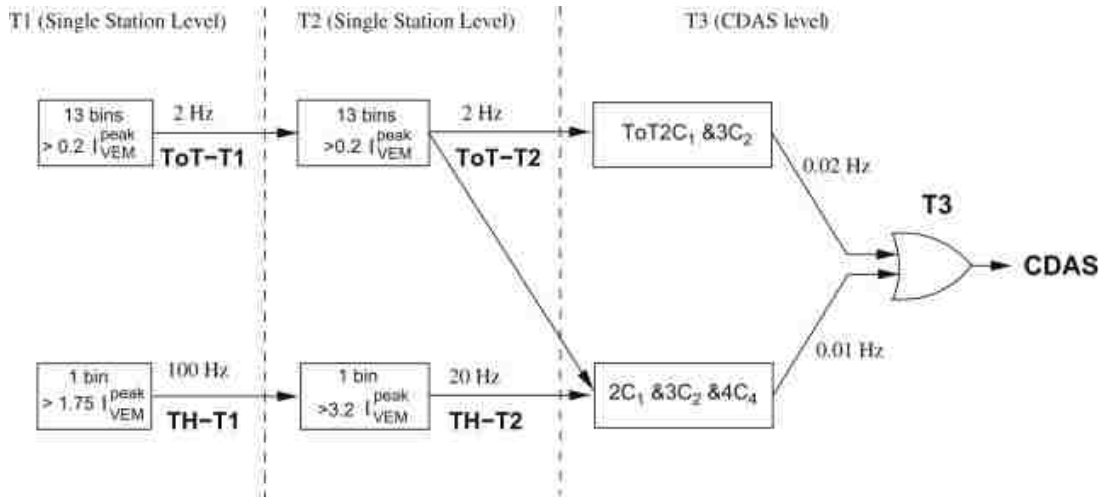

Figure 3.4: A schematic view of the logical relations between the first three trigger levels of the Auger surface detector. From [23].

showers [23]. The trigger rates for the two modes are 100 Hz and 2 Hz respectively. See Figure 3.4.

The second trigger T2 is applied for controlling the event rate to about 20 Hz due to the limit of the bandwidth of the communication system. All T1-TOT triggers are advanced to the T2 level while T1-TH triggers needs to pass an additional threshold of 3.2 $I_{\mathrm{VEM}}^{\mathrm{Peak}}$ in coincidence of all the three PMTs. The event rates of T1-TH trigger are rather uniform among different detectors, within a few percent, whereas the T1-TOT triggers are sensitive to the shape of the signal. However, the T1-TOT trigger rate difference does not affect the event selection or reconstruction. The T2 triggers, their time stamps and subtypes are sent to the CDAS for the formation of the T3.

3.2.3.2 CDAS Triggers

The third trigger T3, formed at the CDAS, is the beginning of the central data acquisition. T3 is based on a combination of T2. There are also two modes in T3. The first mode, called "$ToT2C_1\&3C_2$", requires the coincidence of at least three detectors that have passed ToT conditions, have a closest neighbors and a second closest neighbors triggered. The second mode, named "$2C_1\&3C_2\&4C_4$", does not require TOT. It requires one detector that have

one of its closest, one of its second closest and one of its fourth closest neighbors triggered and pass the TH threshold trigger in coincidence. The time criterion of coincidence here requires that the neighbor detectors need to be within $(6 + 5C_n)\,\mu$s of the first detector, where C_n is the nth set of the closest neighbor. An example of the T3 configuration is shown in Figure 3.5.

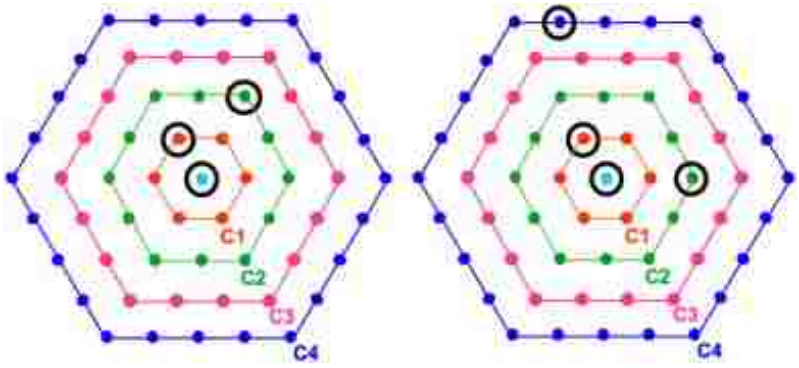

Figure 3.5: Example of two T3 modes. Left, "$ToT2C_1\&3C_2$" mode, right, "$2C_1\&3C_2\&4C_4$" mode. C1, C2, C3, C4 are first, second, third and forth set of closest neighbors, at 1.5, 3.0, 4.5, 6.0 km from the T3 triggered detector respectively. From [23].

Once the T3 trigger is formed, the FADC signal passed T2 requirement are sent to the CDAS. The signal passed T1 but not the T2 would also be passed if the detectors timing are within 30 μs of the T3. The event rates above T3 are about 1200 events/day, containing about 10 % real cosmic ray showers.

3.2.3.3 Offline Triggers

The additional triggers levels are used for offline event selections. The first one, T4, set additional time and space limit for the event selection. It requires two criterion based on the T2 mode. The second one, T5, set further location limit on the shower. It requires that the shower selected by T4 is contained inside the array, which ensures the shower reconstruction quality. Figure 3.6 shows the logical relations between offline triggers.

The fourth trigger, T4, is called physics trigger. There are two criteria defined. The first T4 criterion, called 3ToT, requires the stations, passing the T2-ToT, to have a triangular

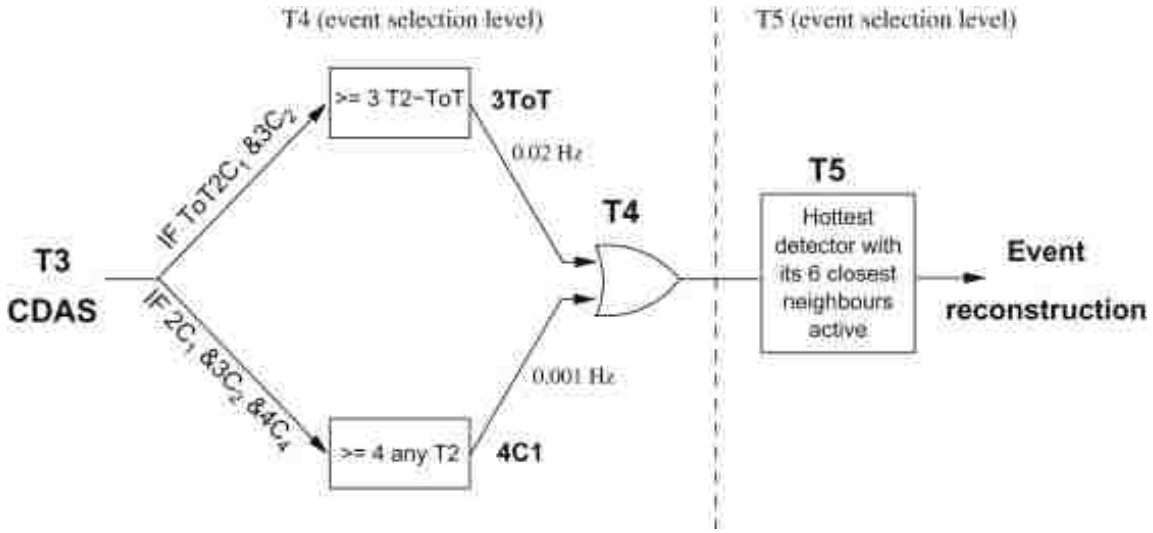

Figure 3.6: A schematic view of the logical relations between the offline triggers of the Auger surface detector. From [23].

pattern. It further requires that the times of the signals of the three stations must fit to a plane shower front which moves at the speed of light. The second T4 criterion, called 4C1, fits on any kind of T2. It also requires the time of signals of the four stations to fit to the plane shower front moving at the speed of light. Both of the modes are highly efficient towards events with non-inclined showers (zenith angle $<= 60°$), having an efficiency of 98% and 100% respectively.

The last trigger, T5, is called fiducial trigger. The aim of this trigger is to eliminate the showers close the border of the surface array. Otherwise, the partly missing shower might have a poorly reconstructed energy and shower axis. The T5 trigger requires that the detector with the highest signal should be surrounded by a operating hexagon of other detectors. In other words, all its 6 closest neighbor detectors should report no errors at the time of event. This fiducial trigger reduces the triggering of the high energy event falling outside the array. The only downside of this trigger is that we might throw away some well contained showers that falls close to a non-working detector since with a array as large as PAO, there might be 1 % of detectors not working at any given moment. Eventually, with the large exposure PAO has, these effects of throwing away these events are negligible.

The trigger efficiency is strongly related to the shower energy. At lower energies, the showers do not have enough signal to pass all the triggers. Above 3×10^{18} eV, the trigger efficiency rises above 97 %. Figure 3.7 shows the trigger efficiency rises with energy.

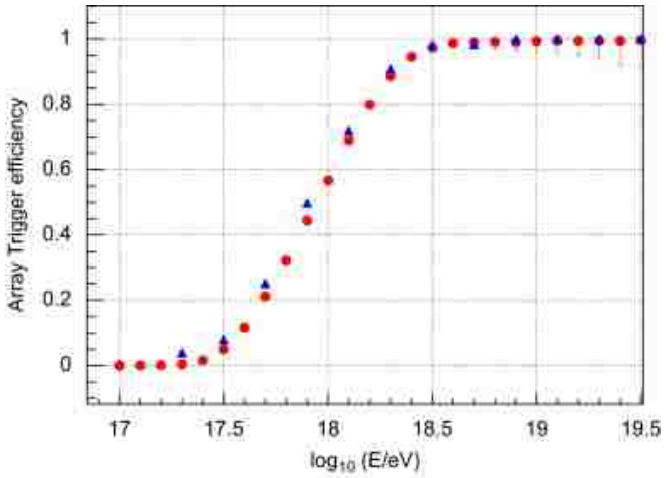

Figure 3.7: Trigger efficiency of the Auger surface detector as a function of energy, the triangles are from SD and the circles are from hybrid data. From [23].

3.2.4 SD Event Reconstruction

The first parameter to fit is the shower front, which is done by fitting the timing reported by the detectors. A shower track can be viewed as a point moving along an axis at the speed of light c. Suppose at time t_i, the point is at position $\vec{x_i}$,

$$\vec{x_i} = \vec{x_0} - c(t_i - t_0)\vec{a} \tag{3.1}$$

where t_0 and $\vec{x_0}$ are the initial time and position of the signal-weighted barycenter, $\vec{a}$ is the unit vector of the shower axis. The shower plane is perpendicular to the shower axis. The time it passes through any other station can be predicted using

$$t_i(x_i) = t_0 - \frac{(\vec{x_i} - \vec{x_0})\vec{a}}{c} \tag{3.2}$$

The shower axis can be fitted by minimizing the square of the difference between the predicted time $t_i(x_i)$ and the measured time t_i [74],

$$\chi^2 = \sum_{i=1}^{n}(t_i(x_i) - t_i)^2 = \frac{1}{\sigma^2(t_i)}\sum_{i=1}^{n}[(t_i - t_0) + \frac{1}{c}(\vec{x_i} - \vec{x_0})\vec{a}]^2 \tag{3.3}$$

where n is the number of stations triggered and $\sigma^2(t_i)$ is the uncertainty of t_i.

The energy reconstruction follows the general discussion as Section 2.5.2.2. Showers that passed the triggers above are stored in FADC bins. Signals are converted to $Q_{\mathrm{VEM}}^{\mathrm{Peak}}$ (as described in Section 3.2.2) and then fitted to the Lateral Distribution Function (LDF) (as described in equation 2.44). The LDF used within PAO is given below,

$$S_r = S(1000)(\frac{r}{1000m})^{\beta}(\frac{r + r_s}{1000m + r_s})^{\beta+\gamma} \tag{3.4}$$

where S(1000) is a fitting parameter representing the signal size at 1000 m from the shower axis, β is a function of zenith angle θ, $\beta = a + b(\sec\theta - 1)$, γ represents the scale of flattening and r_s is fixed at 700m to reflect the difference in shapes of muonic and electromagnetic showers. The initial values for S(1000) are the signal of the stations near 1000 m from the core. For β and γ, the initial values are [74]

$$\begin{aligned} \beta &= 0.9\sec\theta - 3.3 \\ \gamma &= 0 \end{aligned} \tag{3.5}$$

The fitting procedure is the minimization of the square of difference between the station signal S_i and projected signal $S(r_i)$

$$\chi^2 = \sum_{i=1}^{n}(S(r_i) - S_i)^2 = \sum_{i=1}^{n}\frac{[S(r_i) - S_i]^2}{S(r_i)} \tag{3.6}$$

This is based on the assumption that the uncertainty of $S_i \propto \sqrt{S(r_i)}$. Figure 3.8 shows an example fitting of the LDF.

S(1000) varies with different zenith angle. To eliminate the fluctuation, Auger SD uses the energy estimator S_{38}, which is S(1000) if the shower arrived at a zenith angle of 38°.

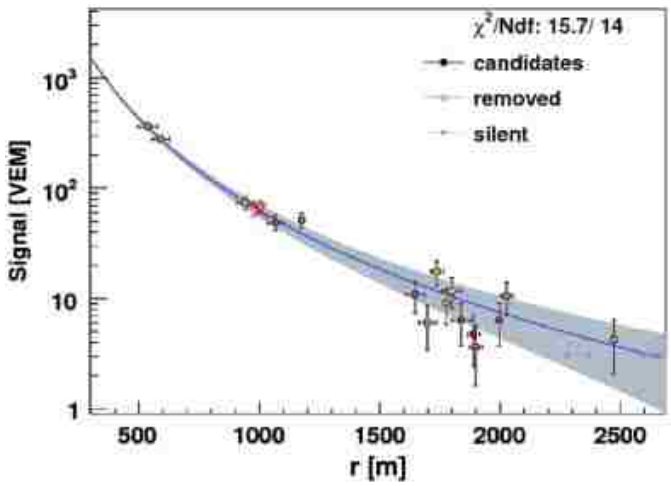

Figure 3.8: Signal density as a function of distance from the shower axis. The solid line is the fitted LDF and the red cross represent the fitted S(1000). From [72].

The relationship between S(1000) and S_{38} is

$$S_{38} = S(1000)/\mathrm{CIC}(\theta) \tag{3.7}$$

where θ is the zenith angle of the reconstructed shower axis and $\mathrm{CIC}(\theta) = 1 + a\,x + b\,x^2$. The variables are $x = \cos^2\theta - \cos^2 38°$, a = 0.94 ± 0.06 and b = -1.21 ± 0.27 [75].

The energy corresponding to S_{38} comes from the correlation of S_{38} and the fluorescence detector reconstructed energy of high quality hybrid events. Figure 3.9 shows the correlation between $\lg(S_{38})$ and $\lg(E_{FD})$.

The data show a linear relationship of

$$\lg(E_{\mathrm{FD}}) = A + B\lg(S_{38}) \tag{3.8}$$

where E_{FD} is in eV and S_{38} is in VEM. The best fit gives the result of A = 17.08 ± 0.03 and B = 1.13 ± 0.02 with a reduced χ^2 of 1.3 [75]. This allows for an energy estimate from S_{38}. Combining equation 3.7 and equation 3.8, the relation below is used for SD energy reconstruction,

$$E_{\mathrm{SD}} = a\,[S(1000)]^b \quad (\text{in EeV}) \tag{3.9}$$

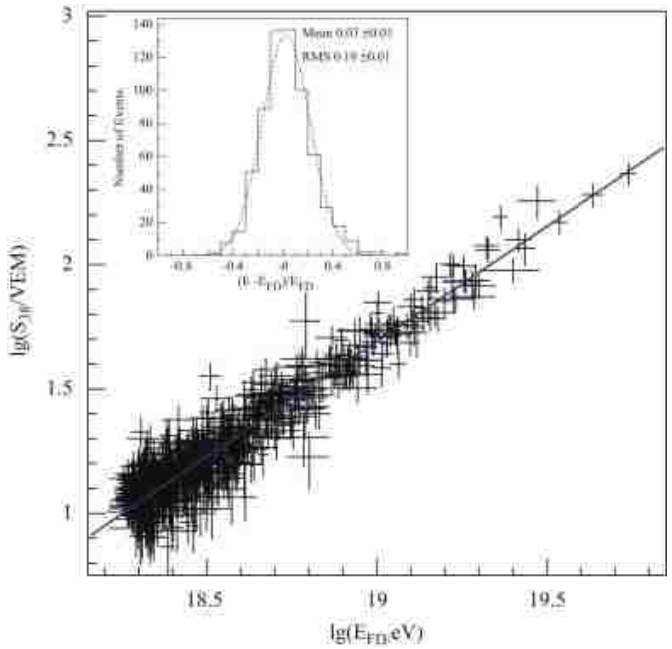

Figure 3.9: Correlation between S_{38} and the FD reconstructed energy, the fractional dispersion is shown in the small plot. From [73].

where $a = 0.37 - 0.51 \sec\theta + 0.30 \sec^2\theta$ and $b = 1.27 - 0.27 \sec\theta + 0.08 \sec^2\theta$ [74].

The SD reconstructed energies have a relatively small statistical uncertainty, e.g. the relative uncertainty $\sigma(E_{\rm SD})/E_{\rm SD}$ at 10^{20} eV is about 5%. Figure 3.10 shows the typical reconstruction information obtained from a real SD event.

3.3 The Fluorescence Detector (FD)

The second technique, as described in Section 2.5.2.1, uses 4 fluorescence sites to look over the surface array named Los Leones, Los Morados, Loma Amarilla, and Coihueco. The four FD buildings are located on the small hills on the edge of the surface array. When charged particles are created during the shower, they interact with atmospheric nitrogen molecules and excite them. The excited molecules emit fluorescence light mainly between 300 nm and 430 nm range, see Figure 3.11. The number of fluorescence photons emitted is proportional to the energy deposit of the shower particles. The timing and intensity of light are measured by the 4 fluorescence detectors, each equipped with 6 independent telescopes with a field

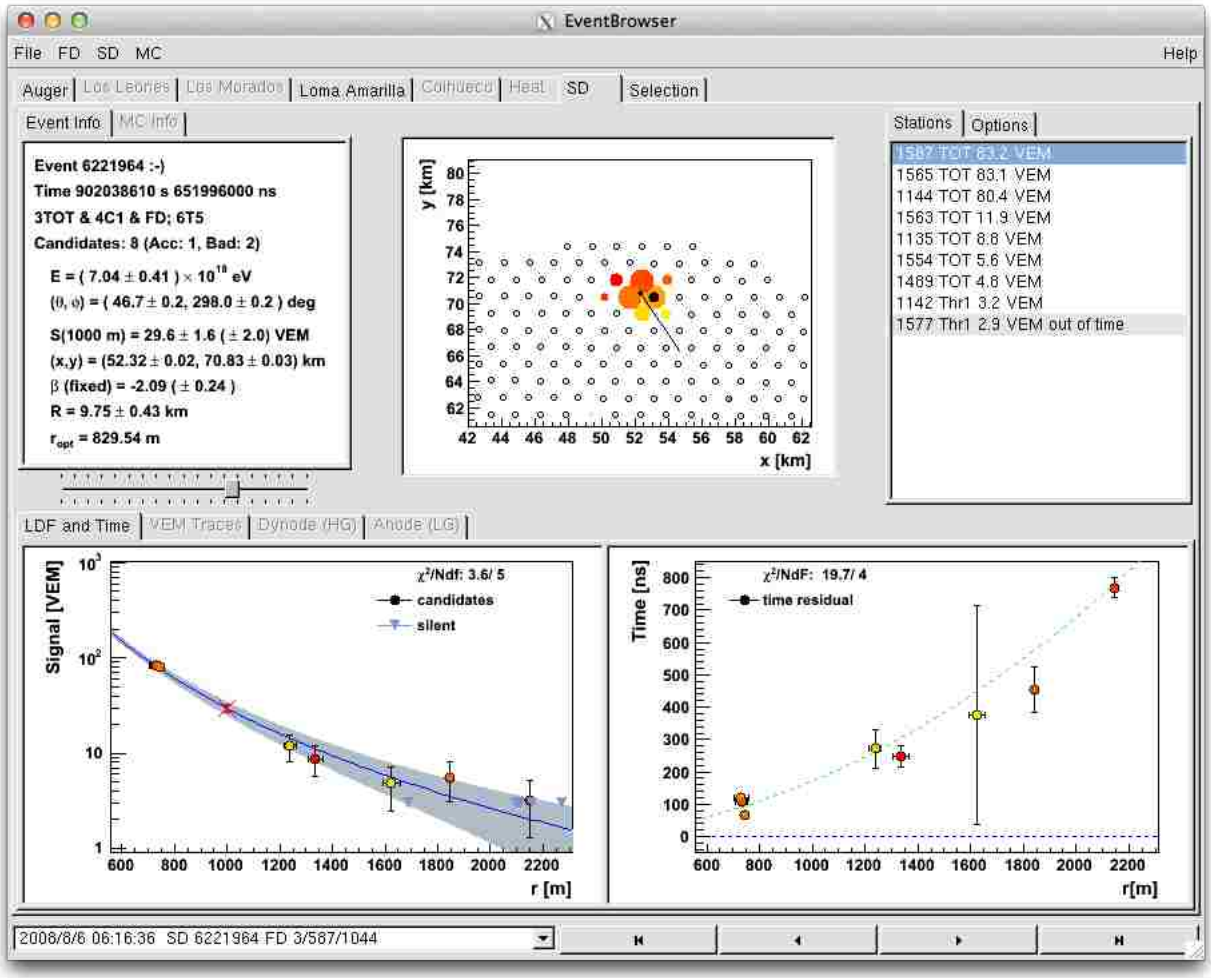

Figure 3.10: Reconstruction of a real SD event with a energy of $(7.04 \pm 0.41) \times 10^{18}$ eV. Top left: summary of the event information, including the event time, trigger type, energy, S(1000), direction and location. Top center: graphical view of the triggered stations, the size of the circle shows the signal size, the larger, the higher. Top right: the signal size of the triggered tanks. Bottom left: the fitting of the LDF. Bottom right:time residual plot, which is the time behind the reconstructed shower front if the shower front is a plane.

of view of $30° \times 30°$ [24]. Figure 3.12 shows a schematic layout of a fluorescence detector building.

3.3.1 Fluorescence Detector Design

As seen in Figure 3.12, the fluorescence detector consists 6 telescopes overlooking the surface detector array at an angle of 180°. The optical system and electronics are well maintained

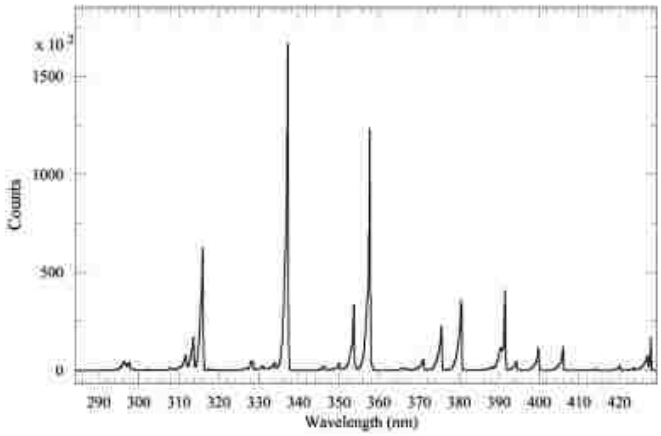

Figure 3.11: Measured fluorescence spectrum. The fluorescence light range is mainly between 300 nm and 430 nm. From [24].

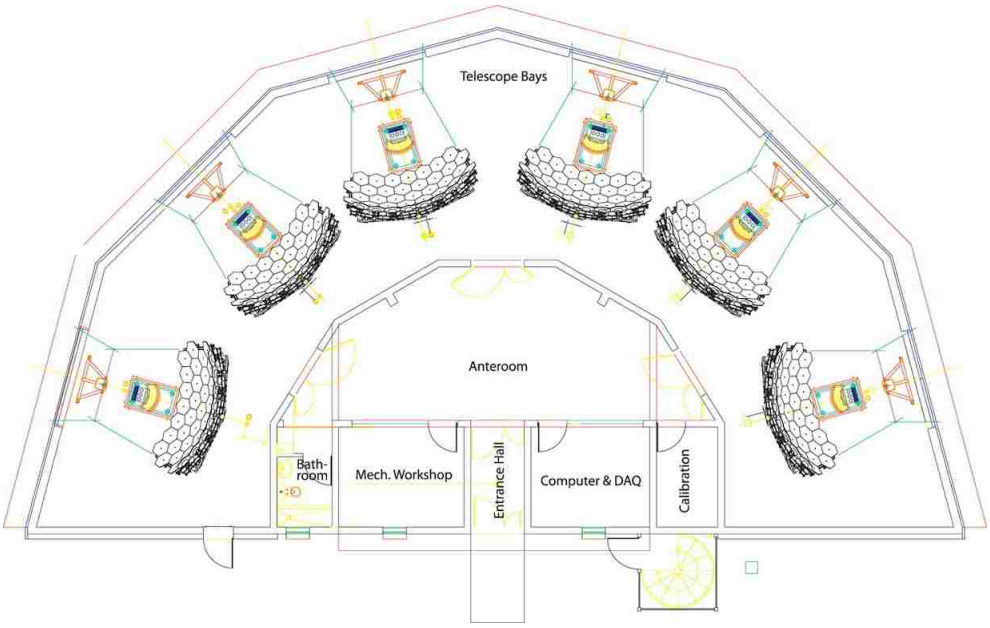

Figure 3.12: Schematic top view of the fluorescence detector layout inside the building. From [24].

inside a clean climate-controlled room. The fluorescence light passes through a large UV-passing filter window and an optical corrector ring when the detector is in operation and shutter is open. The light is then reflected and focused by a 13.4 m^2 mirror to a camera with 440 photomultiplier tubes (PMT). The signals collected are digitized by the electronics enclosure every 100 ns. Once the signals pass the triggers, they are sent to the data acquisition

system (DAQ). A schematic view of the fluorescence detector design is provided in Figure 3.13.

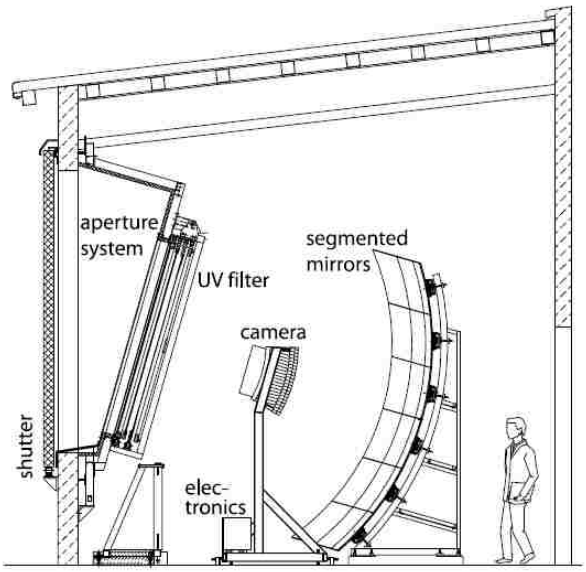

Figure 3.13: Schematic view of a fluorescence detector telescope. From [24].

3.3.1.1 Optical System of FD

The optical system of FD are a Schmidt camera design. It includes the following elements: a circular aperture system after the shutter, a UV filter , a corrector ring , a mirror and a camera of PMTs. Figure 3.14 shows the geometrical structure of the FD optical system.

The aperture consists a circular diaphragm of 3.8 m^2 and has a $30° \times 30°$ field of view. The corrector ring is the circumferential part of the corrector plate with one planar side and another spheric shape corresponding of a 6th order polynomial curve. It is used to reduce the optical aberrations while keeping the advantage of a large aperture.

The main goal of the UV filter is to improve the signal to noise ratio (SNR) from the sky light background. The filter absorbs visible light but let through the nitrogen fluorescence light from $\sim$ 290 nm up to $\sim$ 410 nm wave length. It also acts as a protection and seals the telescope from the outside environment.

The 13.4 m^2 mirror is segmented to reduce the cost and weight of the optical system. Two

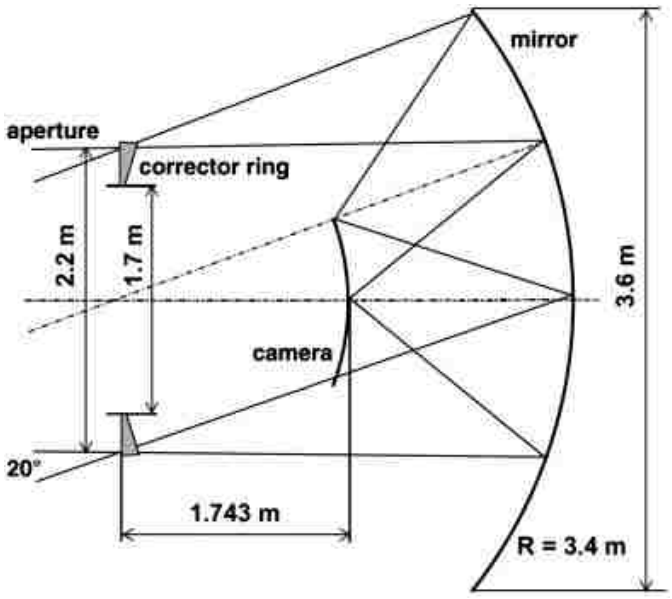

Figure 3.14: Geometrical structure of the FD optical system. From [24].

segmentation configurations are used, one with 36 rectangular anodized aluminum mirrors of three different sizes, the other with 60 hexagonal vacuum-deposited reflective coating glass mirrors of four shapes and sizes. However, the two configuration both have a spherical inner radius of 3.4 m. Los Leones and Los Morados sites use aluminum mirror while Loma Amarilla and Coihueco sites use glass mirrors [24].

The camera of PMTs is the sensitive element of the FD. The 440 PMTs are arranged in a matrix of 22 rows by 20 columns, corresponding to a field of view of 30° in azimuth and 28.1° in zenith. One single camera has a dimension of 930 mm by 860 mm, with spherical outer and inner surfaces. This shape places all the PMTs on the focal surface of the camera. The outer radius of curvature is 1701 mm and the inner radius is 1641 mm. The PMTs are mounted in the 440 40mm diameter holes [24].

The PMTs have a different model (XP3062) from the SD, but still keep the same brand of Photonis. The hexagonal shape of the PMT ensures the optimum coverage to the focal surface. The space between the PMTs are insensitive yet needed for safe mechanical mounting. The light collectors named “Winston cone” are used to maximize the light collection

around the PMT. The "Winston cone" is a combination of six "Mercedes stars", which is a flat reflecting surface. The six Mercedes stars are positioned on the hexagonal vertex and collect the light for a given PMT. Monte Carlo simulation suggests that the light collection efficiency averaged over the camera is 94 %. Without the light collectors, the camera would only manage an efficiency of 70%. A picture of the camera body with PMTs and light collectors is shown in Figure 3.15.

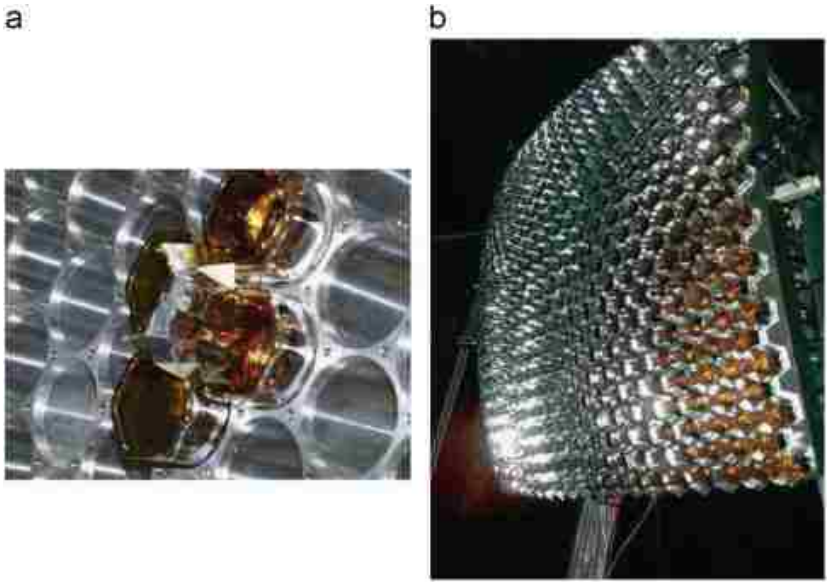

Figure 3.15: a) Picture of the four PMTs mounted with two Mercedes stars. b) Picture of the camera with 440 PMTs and light collectors. From [24].

The XP3062 PMT is an eight stage PMT with quantum efficiency of 25 % or larger in the fluorescence spectrum between 350 nm and 450 nm. Each PMT is equipped with a unit called "head electronic" (HE) to provide a high voltage (HV) of 835 V. The HE grounds the PMT photocathode and supplies positive HV to the anode. It is very efficient and draws a current of less than 170 μA. A different-input and balanced-output low-noise preamplifier is used to provide high rejection rate to the dark sky background and improve the signal to noise ratio. Overall, The PMTs produce a gain of about 4.4×10^4 [70].

3.3.2 Data Acquisition

The PMT signals are received by a set of 20 front-end boards in the electronics enclosure below the camera. The electronics are responsible for filtering, digitizing and storing the signals. Once these signals are processed, they need to pass three levels of triggers set in the firmware and software. After that, these surviving events are sent to the Central Data Acquisition System(CDAS), the same as is done with the SD. If one surface detector is triggered in conjunction with the FD event, a hybrid event is generated. A schematic plot of the FD data acquisition is shown in Figure 3.16. The 440 PMTs $\times$ 6 telescopes and the head electronics detect and record the signal. Frond-End (FE) sub-racks digitize the signals and provide the threshold and geometry triggers. The DAQ subnet, including six mirror PCs, reads out the data and rejects the background noise. The Eye PC, merging data from the mirror PCs, transfers the data to the CDAS in PAO's Malargüe campus. Inside the FD building, there is also a Field PC for the remote control so that the calibration and shift can be done in PAO's campus. The GPS system is the same as in the SD, providing a synchronized time for the camera electronics and PCs.

3.3.3 FD Electronics and Trigger System

The front end electronics have 22 PMT channels. Therefore 20 Analog Boards(AB) are needed to read out each PMT column. The ABs then digitize the inputs by the 10 MHz 12 bit analog-to-digital converters(ADC). The functions of AB include, [24]

1. Performing a differential conversion of the input signal.

2. Adjusting the channel gain. This device can change individual channels gains to a factor of 1.9, thus allows gain matching of all the channels to be within 0.6 % to guarantee a uniform amplitude response.

3. Applying anti-aliasing filter before signal sampling. A fourth-order Bessel filter is implemented to match the 10 MHz digitization rate.

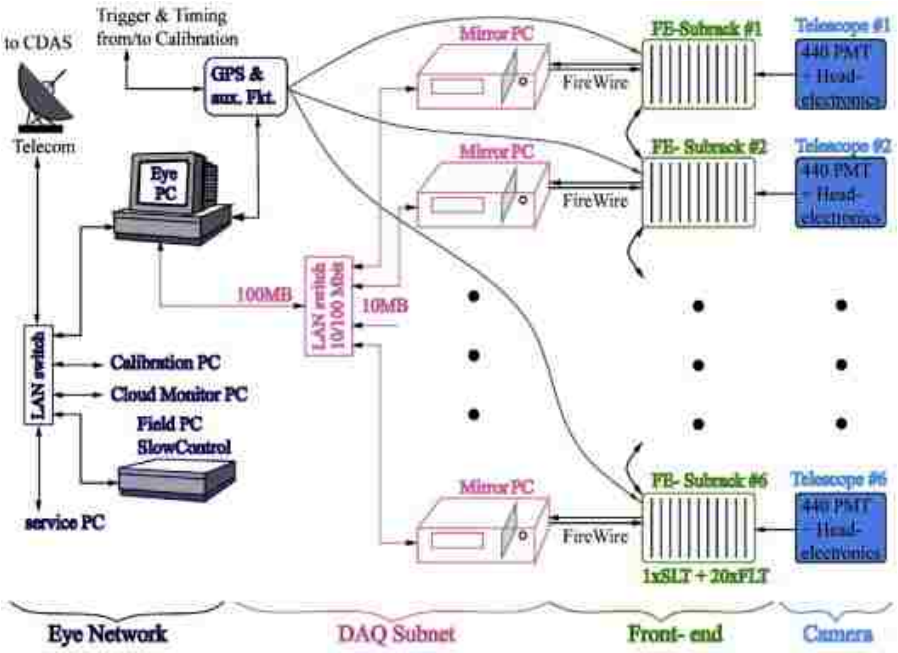

Figure 3.16: Schematic plot of the FD data acquisition system, from right to left. From [24].

4. Expanding the 12 bit ADC to virtual 15 bits dynamic range.This is done by summing the 11 odd and 11 even channel at lower gain and digitizing these two additional "virtual channels", more details about "virtual channels" can be find [76].

5. Providing an injection point for test pulses.

The signals through AB are sent to the trigger system of FD. There are four kinds of triggers, the first level trigger (FLT), the second level trigger (SLT), the third level trigger (TLT) and the hybrid trigger (T3). Their functions and event rates are listed in Table 3.3.

Table 3.3: Trigger levels used by the fluorescence detector. From [24].

Trigger Name	Location	Functions	Event Rate
FLT	FE sub-racks	Pixel threshold trigger	100 Hz/pixel
SLT	FE sub-racks	Track shape trigger	0.1-10 Hz/telescope
TLT	Mirror PCs	Lighting rejection trigger	0.01 Hz/telescope
T3	Eye PC	Hybrid trigger	0.02 Hz/building

3.3.3.1 Hardware Triggers

The first level trigger (FLT) is located on the digital front-end (FE) board. It stores the digitized raw data in the memory, measures the pixel trigger rate for each channel and adjusts the threshold to maintain a trigger rate of 100 Hz regardless of the background light conditions. It also measures the number of triggered pixels in one column.

The second level trigger (SLT), located on a separate board of the FE sub-racks, requires 5 adjacent pixels to be consistent with a light track segment. Figure 3.17 shows the basic types of pattern regard as straight track segments. Note that the algorithm of the SLT only requires 4 out of 5 triggered as the could be a bad pixel at the time of the event. The total number of pattern classes is 108 considering all the rotations and mirror reflections of the basic segments. The SLT reads the pixel trigger column of the camera every 50 ns and the full camera image is scanned by the STL module every 1 μs. Once a pattern is found, the recording of the ADC data starts and the Mirror PC is notified. Both the FLT and SLT are implemented by the Field Programmable Gate Array (FPGA) to improve the flexibility and cost-effectiveness.

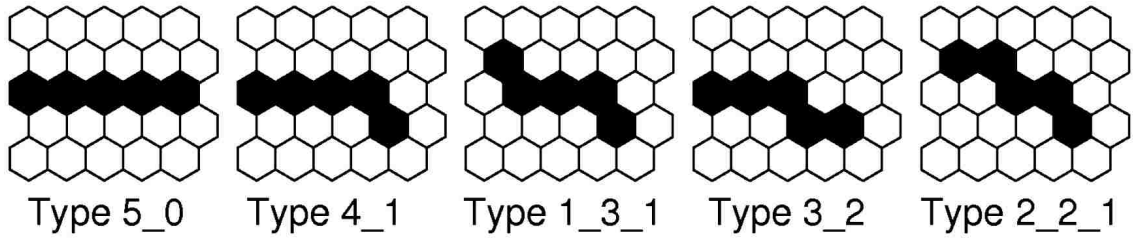

Figure 3.17: Basic types of pattern of triggered pixels used by the second level trigger (SLT) of FD. From [24].

3.3.3.2 Software Triggers

The third level trigger (TLT) is a software trigger designed to reject the random triggered events by the noise. The time sequences of the SLT events are checked to see if they follows the track sequence. The elevation angle vs. azimuthal angle and time are fitted at this rep and the pixels with a large contribution to the uncertainty are removed. After this step,

candidates with more than four pixels are considered good events. The azimuth of the shower impact on the ground and the arrival time are calculated. TLT is optimized to remove the events caused by lighting, muon impact near the camera and random triggered pixels. The rejection rate for bad background events is about 94% and the rejection rate for true showers is below 0.7%.

The hybrid trigger (T3) is sent to the CDAS if coincidence is found between the FD and SD. The purpose of T3 is to record the hybrid events below 3×10^{18} eV where the SD array is not fully efficient. The T3 events usually occur within 20 km of the FD buildings and trigger only one or two surface stations. This is still sufficient for high-quality hybrid reconstruction since the triggered surface stations give good estimate of distance of the shower hitting the ground. These information are merged in offline for hybrid analysis.

A slow remote control system is used for safety measures. During daylight or windy weather, the external shutter is automatically closed. A fail-safe curtain is added at the aperture should there be a mechanical shutter failure. The high-voltage will be cut to protect the PMT once any high light level is detected. An uninterruptible power supply (UPS) is installed to prevent the data losses and emergency operations of the computers and shutters just in case of the main power outage [70].

3.3.4 FD Calibration

The purpose of the calibration is to find the correspond ADC counts to the flux of fluorescence light at the telescope aperture. There are four independent techniques used for the FD calibration, drum calibration, laser shot calibration, multi-wavelength calibration and relative calibration [77].

The first technique, drum calibration, uses a portable 2.5 m diameter, 1.4 m deep drum shaped light source mounted in front of the FD apertures. The drum calibration was originally developed and built by the LSU group. The light source is provided by a pulsed UV LED (375 ± 12 nm) mounted at the center of the drum but against the camera. The light from the LED is then reflected by the side and the back of drum to the front surface. The

side and back surfaces of the drum use diffusively reflective Tyvek while the front surface uses Teflon, a material transmits the light diffusively. This design keeps the light brightness from the surface to be within 1% and the angular dependence to be less than 2%. The light from the drum provides a known photon flux and triggers all the pixels in the camera for an absolute calibration. The overall uncertainty for this calibration is about 9% [77].

The second technique uses artificial laser shots located $\sim$ 4 km from the FD building. The laser is shot vertically upwards at 337 nm $\sim$ 355 nm [77]. The fluorescence yield and pixel response are both well known thus provides an accurate way of the calibration. The advantage of this technique is that it creates a track image that is very similar to the actual shower. Overall, the uncertainty of laser shot calibration is around 12% [24].

The third technique, multi-wavelength calibration, uses a xenon flasher mounted a the back of the drum and 5 notch filters to create lights at wavelengths of 320, 337, 355, 380 and 405 nm. The FD acceptance at different wavelengths can therefore be measured and adjusted. However, the uncertainty of this calibration is large, around 20% [77].

The final technique is a relative calibration done on a nightly basis. Three light sources, fixed at various places in the telescope, are illuminated and the lights are transmitted through optical fibers. The "A" light source is a 470 nm LED located at the center of mirror. It shines the light on the camera directly to calibrate the direct light response of the camera PMTs. The "B" light source uses xenon flash lamps located at the focus of the mirror. It shines the light to the mirror and monitors the mirror reflectivity and camera gain. The "C" light source, using the same light instruments as B, is located out side the aperture. It shines on a reflective Tyvek sheets mounted on the inside of the shutters. It also contains five filters to create five wavelengths at 330, 350, 370, 390 and 410 nm. "Calibration C" is to monitor the end to end detector stability at these five wavelengths.

3.3.5 FD Event Reconstruction

3.3.5.1 Geometrical Reconstruction

The FD event reconstruction follows the general discussions in Section 2.5.2.1. The shower geometry can be determined by timing and signals of the triggered pixels. The first step is to find the Shower Detector Plane (SDP), which is the plane contains both the shower axis and location of the eye, as shown in Figure 2.13. The normal vector of SDP can be found by minimizing weighted product of $\vec{n}_{SDP}$ and the corresponding direction $\vec{r_i}$.

$$\chi^2 = \sum_{i=1}^{n} S_i [\vec{n}_{SDP} \cdot \vec{r_i}]^2 \tag{3.10}$$

where n is the number of pixels triggered, S_i is the signal of the ith pixel for weighting purpose. This step is very solid and the typical error of $\vec{n}_{SDP}$ is within a few tenth of one degree.

The second step is to find the shower axis; this is done by minimizing the sum of the square of the time difference between measurement and expectation.

$$\chi^2 = \sum_{i=1}^{n} \frac{[T_i - t_i]^2}{\sigma_{t_i}} \tag{3.11}$$

where T_i is the expected time for test shower axis which can be obtained by equation 2.38 discussed in Section 2.5.2.1 and t_i is the measured time for that pixel.

However, most FD events stored at PAO are detected in hybrid mode and the triggered surface station can be used to constrain the fit thus improving the accuracy. Also, part of the showers are detected by more than one FD telescope. In this case, the intersection of the SDPs can be used as the shower axis.

The geometry reconstruction accuracy is also tested by the Central Laser Facility (CLF), which will be discussed in Section 3.5. The laser shot from CLF is accurately known in terms of location, direction and intensity so it is a very good source for validating purposes.

Overall the hybrid geometry reconstruction has an angular accuracy of 0.6° in terms of arrival direction and a resolution of 50 m in the shower core ground location [24]. This

uncertainty shows good agreement with the shower simulation studies.

3.3.5.2 Shower Profile and Energy Reconstruction

The FD shower profile is reconstructed by the fitting of Gaisser-Hillas (GH) function, described in equation 2.37. As discussed earlier in Section 2.5.2.1, the energy deposit during the shower development is proportional to the emitted fluorescence light. Thus it is possible to get the primary shower energy by integrating the shower profile.

$$E_{FD} = \int_0^\infty GH(x)\,\mathrm{d}x \tag{3.12}$$

Note that this integral will miss the "invisible" energy carried away by neutrinos and high-energy muons that are not contributing to the FD shower profile. The solution is to apply corrections based on Monte Carlo simulations [78]. The extent of corrections depends on assumptions about the primary particle type and the interaction model, however, the difference is only a few percent. If assuming a mixed composition (50 % protons and 50 % iron nuclei) with energy 10^{19} eV, the average missing energy correction is about 12 %. The systemic uncertainty of FD is rather large at 22 %, compared to SD at 5% [78]. The major contributions to the uncertainty include absolute fluorescence yield, absolute calibration of FD and the reconstruction method. The pressure, humidity and temperature of the air also affect the reconstruction.

Figure 3.18 shows the information obtained from the reconstruction of a real FD event.

3.4 Hybrid Events

The surface detector (SD) takes data all the time (100% duty cycle) while the fluorescence detector (FD) only works on clear moonless nights ($\sim$ 10% duty cycle). So the FD data give a small subset of the total data and provide nice crosschecks of these two techniques. Events measured by both detector systems are called hybrid events. Figure 3.19 shows a hybrid event example.

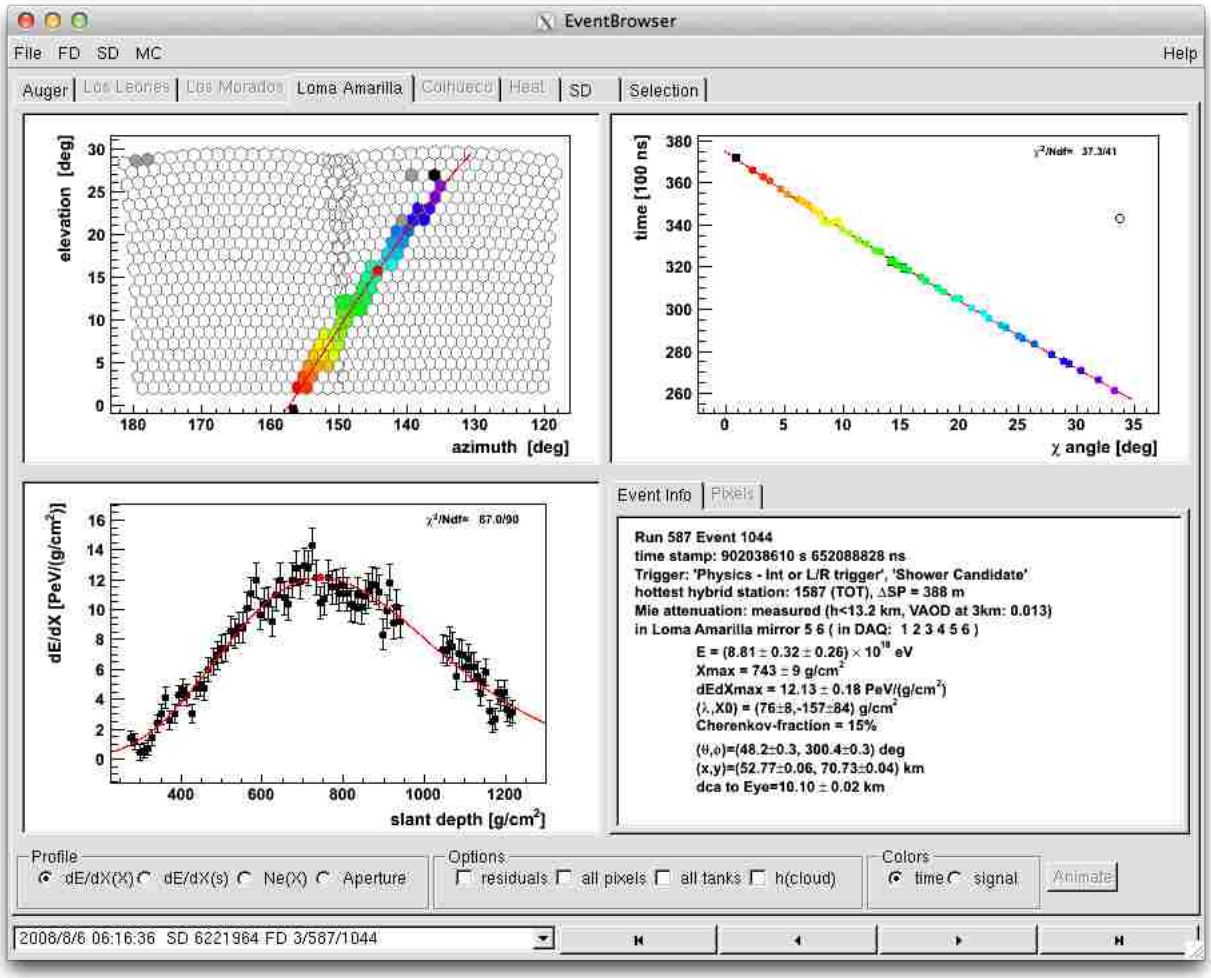

Figure 3.18: Reconstruction of a real FD event with an energy of $(8.81 \pm 0.32) \times 10^{18}$ eV. Top left: the fluorescence light track recorded by camera. The color of the pixels shows the time sequence (top to bottom). Top right: correlation between the pixel triggered time and the pixel pointing direction. This is for geometrical reconstruction. Bottom left: shower profile reconstruction by the fitting of GH function. Bottom right: summary of the event information, including the event time, trigger type, energy, X_{max}, direction and location.

Two steps are needed for the geometrical reconstruction of hybrid events . The first step is to find the SDP, which we already discussed in Section 3.3.5.1. The second step is to find the shower axis. The shower axis can be determined just by FD signal, as also described in Section 3.3.5.1. However, any single triggered surface detector location and time can constrain the parameters and vastly improve the shower axis reconstruction accuracy. Figure 3.20 shows the comparison between the reconstruction by FD and by Hybrid method.

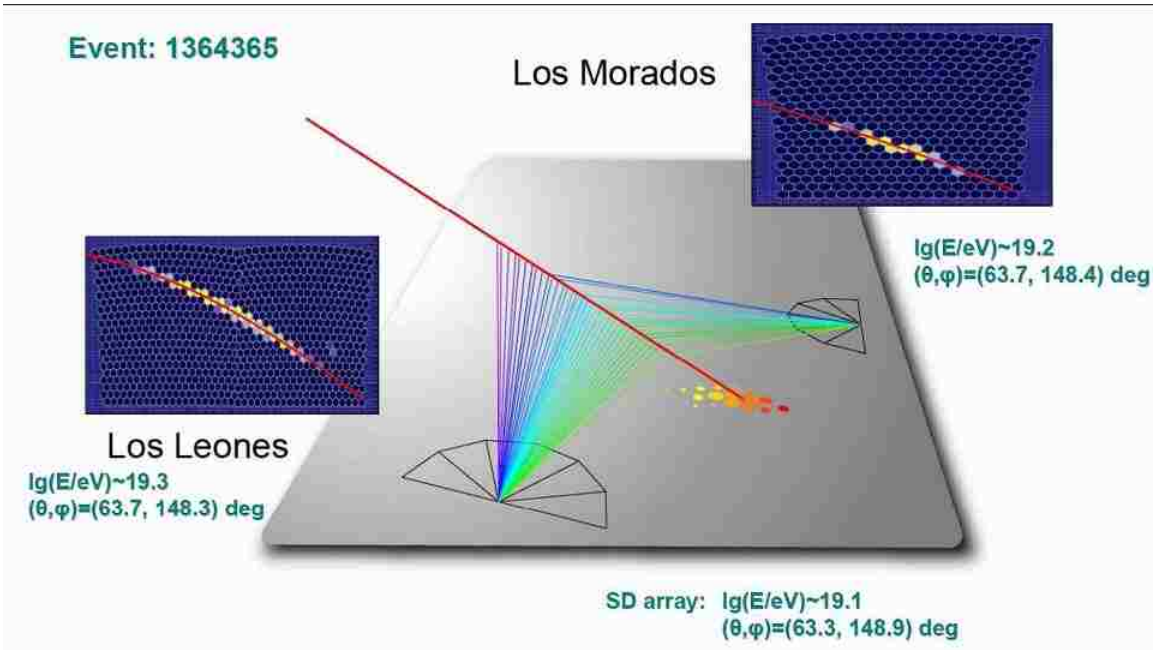

Figure 3.19: A hybrid event example. Courtesy Auger group at University Complutense of Madrid.

The improvement is significant.

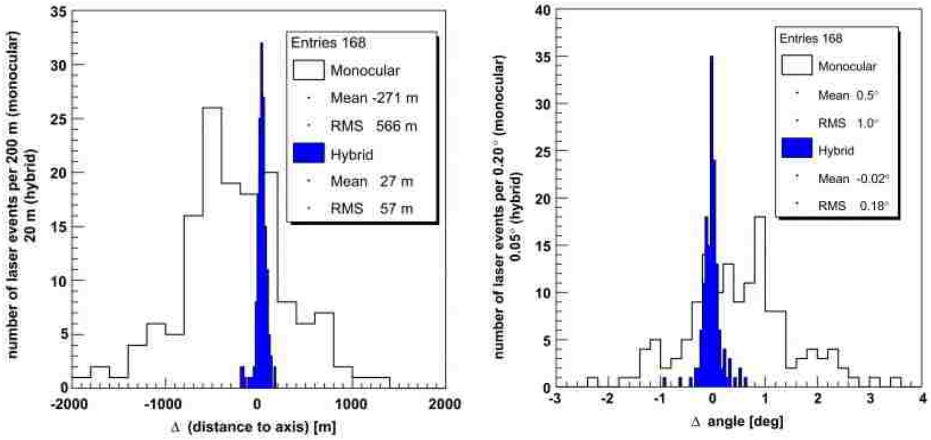

Figure 3.20: R_p (left) and angular resolution (right) of artificial vertical laser shots (CLF) reconstructed by monocular (1 FD eye only) and hybrid (1 FD eye + 1 SD timing) data. From [79].

The energy reconstruction follows the same procedures as discussed in Section 3.3.5.2. The difference lies in that the hybrid reconstruction brings better geometrical precision thus

the shower profile measured would be more accurate.

3.5 Atmosphere Monitoring

The atmosphere monitoring has always been an important part of the PAO since the knowledge of UV light production and transmission in the atmosphere is crucial for the FD reconstruction as been discussed in Section 3.3.5.2. PAO has implemented multiple types of atmosphere monitoring facilities to provide detailed information of the atmosphere properties at different time of operation. These facilities include: two central laser facilities, four elastic LIDAR stations, one Raman LIDAR, four IR cloud cameras, five weather stations, a balloon launch facility, two aerosol phase function (APF) monitors, and two optical telescopes (HAM, FRAM) [81]. The locations of current facilities for the atmosphere monitoring with regard to SD and FD are shown in Figure 3.21.

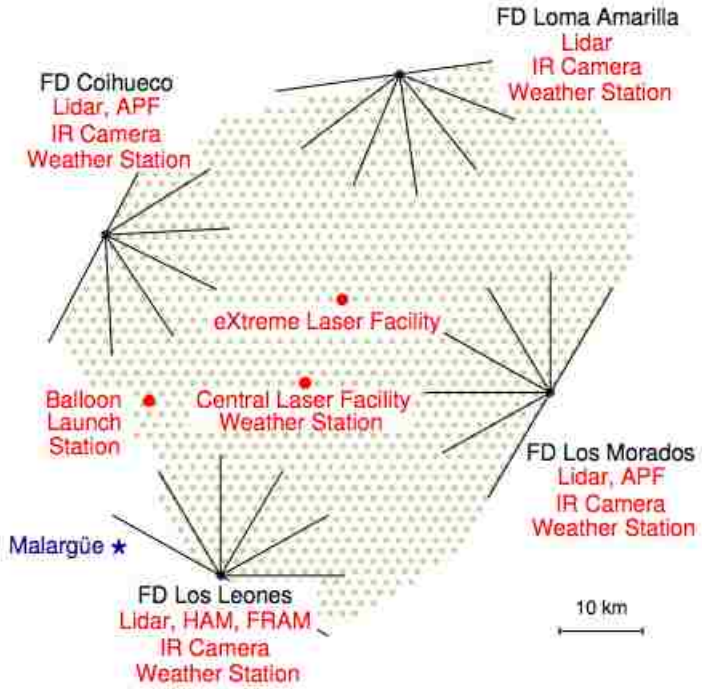

Figure 3.21: The locations of the atmosphere monitoring facilities in the PAO map. From [85].

3.5.1 Central Laser Facility (CLF) and eXtreme Laser Facility (XLF)

The CLF and XLF are two laser facilities located in the middle of the PAO surface array. The goal of CLF and XLF includes: atmospheric conditions monitoring, independent FD calibration, as described in Section 3.3.4, and improving the geometric reconstruction of air shower events, as detailed in Section 3.3.5.1. The laser used by the two facilities has a wavelength of 255 nm, in the middle of the air shower fluorescence bandwidth. The laser has a pulse lasting 7 ns, at full power, the light scattered in the atmosphere is very close to the fluorescence light emitted from a cosmic ray shower of 10^{20} eV primary energy [82]. In addition, the facility is connected with a nearby surface detector via optical fiber, which provides a perfect cross-check of the hybrid event reconstruction.

A weather station and a single-pixel radiometric cloud monitor are also attached to the facilities. The weather station can record the temperature, pressure, humidity, wind speed and direction. The radiometric cloud camera can record the temperature of the sky, which provides the cloud information together with the more elaborate cloud camera [82]. Figure 3.22 shows a picture of the CLF with a near by SD station.

Figure 3.22: The central laser facility, shown with near by surface station "celeste". The two are connected via optical fibers. From [82].

3.5.2 LIght Detection And Ranging (LIDAR)

The LIDAR system are installed in all the four FD sites. The goal of LIDAR is to provide clouds information during the FD operation. Every hour during the FD shift, the LIDAR shoots its laser to scan the sky and get back the reflected signals. The back-scattered signal is detected by the PMTs at the foci of three parabolic mirrors. The laser and mirrors are mounted on a steerable frame so that it can point to any direction on the sky. The signal data provide the information about the clouds height, coverage, depth and opacity as well as the local aerosol scattering and absorption properties. In addition to that, a program called "shoot the shower" is used by LIDAR. When a high quality shower is detected, the LIDAR will suspend its routine scanning duty and shoot a laser along the reconstructed shower axis within a few minutes. This program allows rejection of events that are distorted by the clouds or aerosol non-uniformity, thus improves the reconstructed events quality [83].

It should be noted that a Raman LIDAR system is available near Los Leones. This detector measures backscatter light that has been frequency shifted by Raman scattering from atmospheric nitrogen and oxygen. The Raman LIDAR allows for a more accurate reconstruction of aerosol transmission comparing to elastic backscatter LIDARs.It detects aerosols and the relative concentrations of N_2 and O_2 in the atmosphere. Due to the small Raman scattering cross-section, this technique requires high power laser shot, which would lead to light pollution during the FD operation. Hence the Raman LIDAR only operates 20 mins before and after each FD shift.

The LIDAR database from 2004 to 2009 reports 50% of the FD operating hours are in clear conditions, 60 % time are with less than 25 % of coverage and 20 % time are with more than 80 % of cloud coverage [81].

3.5.3 Infrared Cloud Camera (IR camera)

Since clouds radiate strongly in infrared, four IR cameras with spectral range between 7 and 14 μm are mounted on the roof of each FD building to take a full picture of the sky every 15

mins. The camera has a field of view(FOV) of $45^\circ \times 35^\circ$ but is mounted on a steering frame, so it can scan the whole sky routinely. The sky images are processed and mapped with the FD camera location. Figure 3.23 shows an example of an IR camera image.

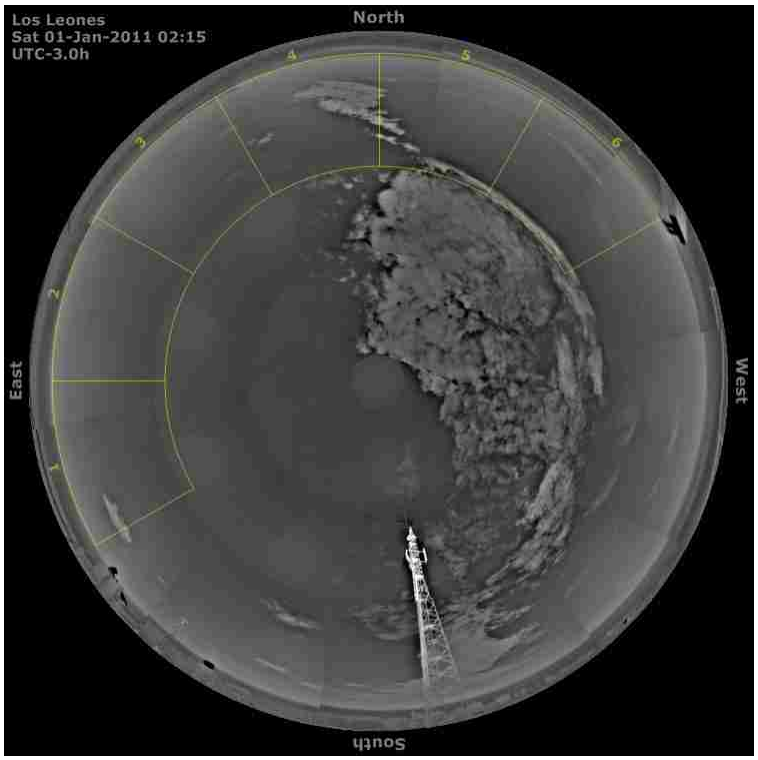

Figure 3.23: An example cloud image from the IR camera at Los Leones on Jan. 1st, 2011. The tower shows the location of Los Leones, and the white part is the cloud coverage. Courtesy Auger group at University of Adelaide.

3.5.4 Radiosonde Balloons

A balloon launch facility is used to model the altitude dependence of the temperature, air pressure and relative humidity. The balloons are filled with helium and equipped with radiosondes. They are launched up to 23 km above Auger site roughly every five days. Since 2003, there has been more than 280 successful launches. The first atmosphere model was introduced in 2005 and has been updated to include more radiosonde data and humidity profiles [81].

3.5.5 Aerosol Phase Function monitors (APF)

For better FD energy reconstruction, one needs to have a great knowledge of the light scattering due to atmospheric aerosols. In practice, aerosols vary greatly in size and shape and can change rapidly during rain and wind. Thus, it is very difficult to find a theoretical model for the scattering cross-section. The Aerosol Phase Function monitors [84] are designed for better measurement of the aerosol scattering. There are two APF light sources, one near Coihueco and the other near Los Morados. The APF light sources fire a near-horizontal pulsed light beam across the field view of a near by FD. The APF can be fitted by light signal received by the FD camera with regard to the scattering angle. This measurement is done on an hourly basis during the FD operation. The FD, with a broad range of viewing angle($\sim 180°$) in azimuth, can measure the APF over wide range of scattering angle.

3.5.6 Horizontal Attenuation Monitors (HAM)

The Horizontal Attenuation Monitors are designed to measure the horizontal attenuation length near the ground level of FD. The laser shoots horizontally from a DC light source on one FD building to a receiver on another FD building. The shots are below the field of view of the FD eye. The DC light source emits a broad spectrum of wavelengths including the FD sensitive range($300 \sim 400$ nm). The light receiver uses UV enhanced CCD arrays at the focus of a 15 cm diameter mirror. A filter is used before the CCD allows measurements at five different wavelengths. The measurement is performed every hour during the FD operation [86].

3.5.7 Fotometric Robotic Atmosphere Monitoring (FRAM)

The main purpose of FRAM is to continuously monitor the wavelength dependence of the total column aerosol optical depth. The facility is located near Los Leones and works independently and automatically. FRAM observes a set of standard bright UV stars and obtains the extinction coefficient and extinction wavelength dependence. Five filters are used, for

wavelengths between 360 and 547 nm. FRAM performs a photometric calibration of the sky on various UV-to-optical wavelengths using a 0.2 m telescope and a photometer. FRAM is fast; the data for one star is taken in less than five minutes. Since it observes stars, it does not introduce any light pollution to the FD observation, which is an advantage comparing the CLF and LIDAR. On the other hand, the disadvantage is that FRAM can only get the integral measurement of the whole atmosphere. The facility was installed in 2005 and has been taking data routinely since 2006 [87].

3.6 PAO Scientific Results

As the world's largest cosmic ray observatory, PAO has had multiple important scientific results since its debut in 2004. Having collected more ultra-high energy cosmic ray events than any other cosmic ray experiments and implementing the hybrid technique, PAO is steadily fulfilling its goal to answer the most basic UHECR questions hindering the scientists for the last century. Recent PAO results include limits on the photon and neutrino primary fraction, observation of the "ankle" in the energy spectrum and GZK suppression at the end, depth of shower maximum (X_{max}) measurement and its indication on cosmic ray composition, anisotropy studies with the cosmic ray arrival direction and the proton cross-section at the highest energy.

3.6.1 Photons and Neutrinos Limits

Ultra-high energy photons are expected to penetrate deeper in the atmosphere than protons with a same energy. Their X_{max} differences are about 200 to 300 g/cm^2 [88]. This is due to the electromagnetic showers initiated by photons have a smaller multiplicity comparing the hadronic ones such that more interactions would need to reach critical energy before the cascades stops. The LPM effect (turning on above $\sim 5 \times 10^{19}$ eV) also suppresses the pair production and bremsstrahlung cross-sections [89]. Both FD and SD events can be used to study the photon primary fraction. On the FD side, events with unusually large X_{max}

are searched. For the SD, the sensitive observables are the bigger rise time and smaller shower front curvatures. This is due to the muon signal in the photon primary showers and the photon shower starts deeper in the atmosphere. The relations between shower front curvature and muon signal fraction will be discussed in Chapter 5.

The first photon limit result uses FD data from December 2004 through December 2007 [90]. Reconstruction and quality cuts are used to select high quality events. Quality cuts set limit on X_{max}, number of triggered pixels, SD timing, fitting χ^2 to make sure the shower are well measured. Additional cuts, including deeper limit of X_{max}, no clouds, and correlation factor are used to select the photon candidate. The number of FD events after the cut and photon shower candidates are given in the Table 3.4.

Table 3.4: FD photon fraction limit result. From [90].

Threshold Energy (EeV)	Number of event after initial cuts	Number of candidates after additional cuts	Photon fraction upper limit at 95% confidence level
2	2063	8	3.8 %
3	1021	1	2.4%
5	436	0	3.5%
10	131	0	11.7%

The SD data give the photon upper limit on the higher energies because of their much larger statistics. From current analysis, PAO found no candidates for photon showers above 10 EeV in data range between January 2004 to December 2006. The SD photon fraction limit result are shown in Table 3.5.

Table 3.5: SD photon fraction limit result. From [89].

Threshold Energy (EeV)	Number of event after initial cuts	Number of candidates after additional cuts	Photon fraction upper limit at 95% confidence level
10	2761	0	2.0 %
20	1329	0	5.1%
40	372	0	31%

The photon fraction limit also sets bounds for the "top-down" models for the production of UHECR, since "top-down" models would see significant amount of photon flux. Hence

the "bottom-up" models seems to be more likely. These two type of models are discussed in Section 2.3.1.

Neutrinos rarely interact within the atmosphere, so it is very unlikely to see neutrino showers because of the hight background of cosmic ray events. PAO is searching its horizontal showers (zenith angle $> 60°$) since they have very large atmosphere depths. A neutrino interacts deep in the atmosphere and starts a shower that still has detectable electromagnetic components in SD while the hadronic showers loses most of its electromagnetic component in the atmosphere if the atmosphere depth is very large. PAO sets a series of requirements for an event to be considered a neutrino candidate, including FADC signal size, "young shower condition", triggering tank spread shape and trigger time [91]. The searchable event base includes the SD data from January 2004 to May 2010 and no tau neutrino candidate was found. The updated tau neutrino upper limit is set at $E_\nu \, dN_{\nu_\tau}/dE_\nu < 3.2 \times 10^{-8} GeV \, cm^{-2} \, s^{-1} \, sr^{-1}$ in the energy range of 1.6×10^{17}eV $< E < 2.0 \times 10^{19}$eV at a confidence level of 90% [92].

3.6.2 Cosmic Ray Flux and GZK Cutoff Observation

One of the most important tasks of PAO is to measure the energy spectrum at the highest energies. The measurement is done by combining the hybrid data and SD data with a maximum likelihood method. As discussed in Section 3.2.4, the SD energy estimator S(1000) is calibrated using the hybrid events, so they share the same systemic uncertainties. On the other hand, the two have different normalization uncertainties (6% for the SD and 10% for hybrid data at 10^{18} eV). The energy resolution for hybrid data is better at 6 % comparing to SD data at 15%. The hybrid data used here is from November 2005 to May 2008 and the SD data is until December 2008 [93].

Figure 3.24 shows the energy spectrum derived from PAO data and a comparison to the HiRes spectrum. The shapes are very similar, just shifted with different energy reconstruction. It can be clearly seen that the power law index changes at around 4×10^{18} eV from $3.26(\pm\ 0.04)$ to $2.55(\pm\ 0.04)$. This change is called "the ankle", as we discussed in Section 2.2. The reason for the change is either there is a transition of flux from galactic to extra-

galactic sources or a change in the source spectrum [72]. Above "the ankle", there is another change at around 4×10^{19} eV; the flux is suppressed by a factor of 2. The significance exceeds 20 σ. This is similar to the expected spectrum effects from GZK interaction processes, but could also be caused by the changes at the source [93].

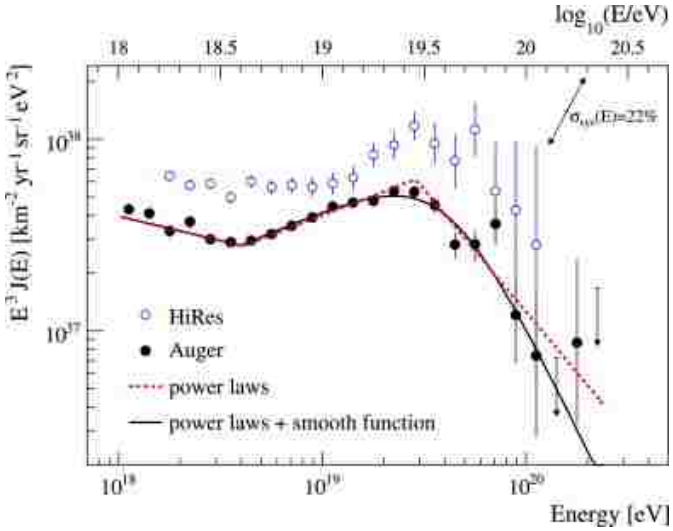

Figure 3.24: The highest energy cosmic ray spectrum from PAO data and HiRes data. The PAO spectrum is fitted with power law functions. The two spectrum are compatible if shifted within their energy uncertainty. Auger data have a energy scale uncertainty of 22% (indicated by arrows). From [93].

3.6.3 Composition Studies with Depth of Shower Maximum (X_{max})

As discussed in Section 2.4, the depth of shower maximum (X_{max}) is very sensitive to the comic ray primaries. Proton showers, having smaller cross-sections (first interaction deeper) and developing multiplicity at a slower rate than iron showers (taking longer to stop developing), get a larger X_{max} on average and a larger event to event fluctuation. The FD of PAO can measure the longitudinal shower profile in the sky and therefore can calculate the average X_{max} by fitting the Gaisser-Hillas function to the shower profile. The X_{max} depends on the energy, the composition and the hadronic model. The generalized Heitler model gives such relationship

$$\langle X_{max} \rangle = \alpha(\ln E - \langle \ln A \rangle) + \beta \tag{3.13}$$

where $\langle \ln A \rangle$ is average of the logarithm of the primary masses, E is the energy of the primary particle and α and β are model dependent parameters [33, 34].

Multiple cuts are made to ensure event reconstruction quality and unbiased event selection. Only hybrid data from December 2004 to March 2009 are used and a total of 3754 events survives all the cuts. The results of $\langle X_{max} \rangle$ and RMS(X_{max}) as a function of energy are shown in Figure 3.25, comparing with simulation with different hadronic models. The systematic uncertainty of FD energy is 22% and the uncertainties for $\langle X_{max} \rangle$ and RMS(X_{max}) are $\leq 13\,\mathrm{g/cm^2}$ and $\leq 6\,\mathrm{g/cm^2}$ respectively. As can be seen both results show a transition from lighter composition to a heavier one and RMS(X_{max}) transition seems faster. However, a cross-section increase of proton at higher energies could also be an explanation.

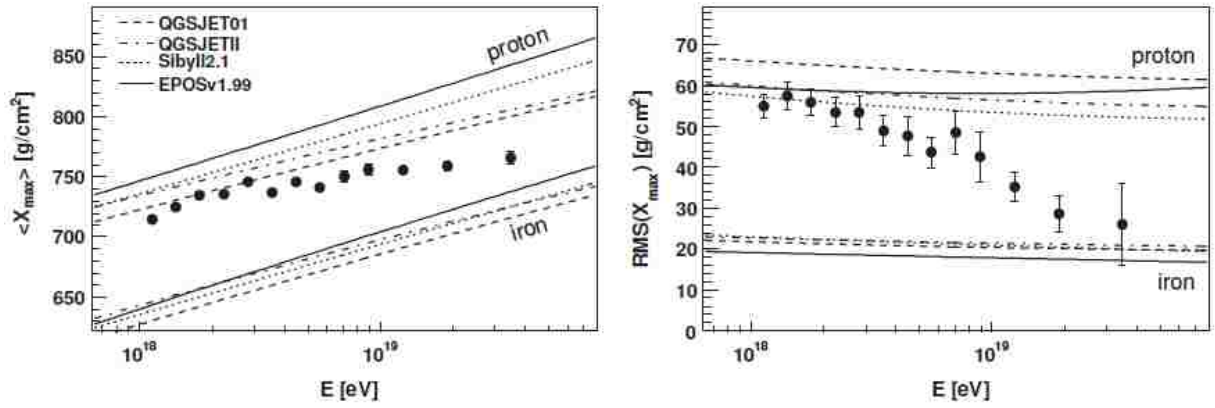

Figure 3.25: Measurement of the average depth of shower maximum $\langle X_{max} \rangle$ and the fluctuation RMS(X_{max}) versus the cosmic ray energy compared with air shower simulations using different hadronic models. From [94].

3.6.4 Anisotropy Studies with the Arrival Direction

The highest energy cosmic rays are sufficiently rare that only a handful of 100 EeV events were detected before PAO. The data set of PAO exceeds that from all the previous experiments given the large exposure. The "GZK effect" discussed in Section 2.3.3 implies that

only relatively nearby sources (within about 200 Mpc) can contribute to the UHECR flux observed on Earth [96]. Most of the cosmic rays are charged so they are deflected by the magnetic field during travel to the earth. Fortunately, the deflection angles are relatively small, especially for those particles with an energy above a few tens of EeV. Then, an efficient way to look for the sources is to look for the correlation between the reconstructed arrival direction of events above certain energy and the location of candidate sources.

The first result of PAO [95] suggested a correlation between the the arrival direction of cosmic rays above 6×10^{19} eV and AGN of the 12th Veron-Cetty and Veron catalog(VCV) [97]. The PAO data used here is from January 2004 to August 2007. The correlation studies use a scan of three variables: the minimum energy threshold E_{th}, the maximum AGN red shift z_{max} and the maximum angular separation ψ. A scan is performed for the probability P that k or more out of N events correlate by chance for an isotropic flux of events. P is described by the cumulative binomial distribution [72].

$$P = \sum_{i=k}^{n} \binom{n}{i} p^i (1-p)^{n-i} \tag{3.14}$$

where p is the acceptance-weighted fraction of sky accessible to PAO that is within ψ of AGN [95].

In these scan results, a minimum probability P_{min} is found for the parameter set E_{th}=56 EeV, $z_{max} = 0.018$ (75 Mpc) and $\psi = 3.1°$. With this parameter set, 21 % of correlation of AGN are expected for the isotropic flux. For events from January 2004 to May 2006 (period I), 12 out of 15 events are found to be correlated (80%). For events from May 2006 to August 2007 (period II), 8 out of 13 events are found to be correlated (62%). A full scan for period I and II is performed and the result for a minimum P_{min} occurs for the parameter set E_{th}=57 EeV, $z_{max} = 0.017$ (71 Mpc) and $\psi = 3.2°$. With this new parameter set, 20 out of 27 events (one event is dropped for the new E_{th}) are found to be correlated (74%) while only 5.6 events are expected for isotropic flux. With this large difference in the correlation level, the hypothesis of isotropic flux is rejected at 99% confidence level. Figure 3.26 shows the arrival direction of most energetic auger events and the closest AGN in Galactic coordinate

system.

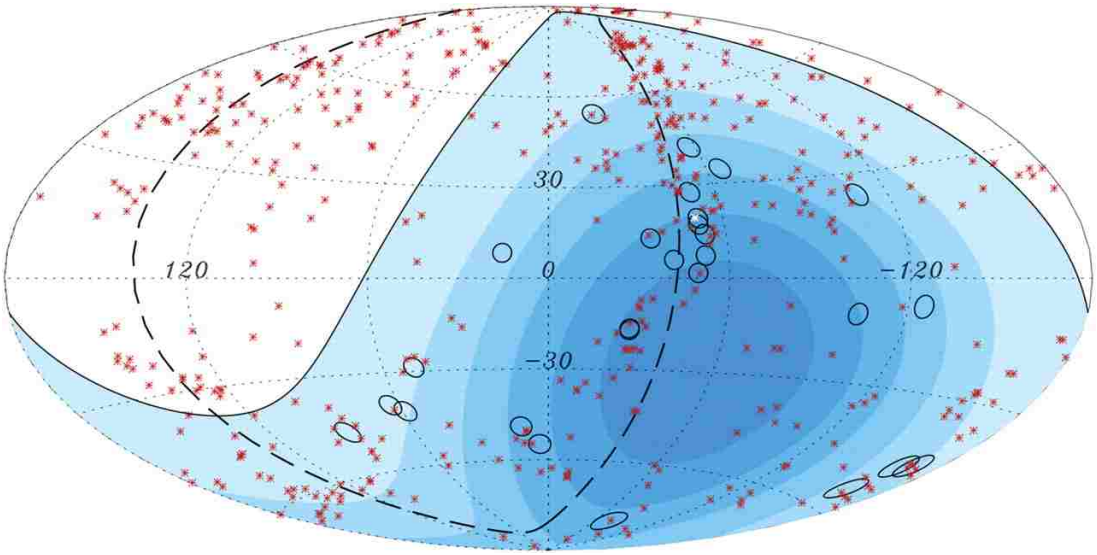

Figure 3.26: Sky map of PAO correlation result in 2007. The arrival direction of the 27 highest energy PAO events are marked in black circles and the locations of 472 AGN in VCV catalog are indicted in red dots. The solid line marks the border of the field of view of PAO (zenith angle $\leq 60°$) and the dashed line is the super Galactic plane. The blue color indicates the relative PAO exposure. From [95].

The correlation result was updated in 2009 International Cosmic Ray Conference with more statistics [99]. The new data added period III from September 2007 to March 2009. The updated parameter set is E_{th}=55 EeV, $z_{max} = 0.018$ (75 Mpc) and $\psi = 3.1°$. In the updated data set (period II+III), 17 out of 44 events are found to be correlated (39%) compared to 9.2 expected for the isotropic flux. Figure 3.27 shows the changes between period II and III. The anisotropy is not strengthened by the new data but there is still less than 1% of probability the UHECR arrive isotropically. The degree of correlation with the VCV catalog, however, is weaker than the first correlation result [99]. The cause for this change is still under investigation.

3.6.5 Ultra-High Energy Proton Cross Section with Air

The energy of cosmic rays measured at PAO is beyond the reach of man-made accelerators. The observations provide a unique way of studying the proton air interactions at such en-

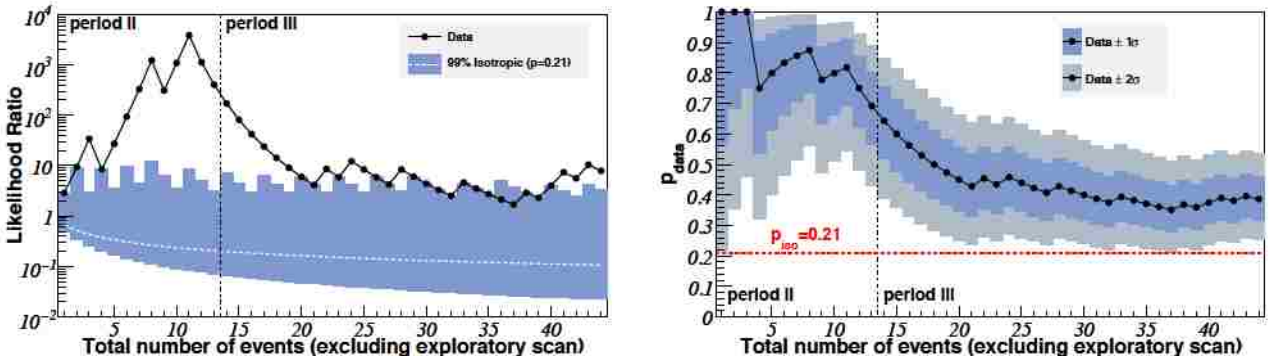

Figure 3.27: Sequential PAO correlation result for period II and III. Left, likelihood ratio as a function of total number of time-ordered events. Black circles are the likelihood ratio and the blue shaded area indicates the range of the 99 % isotropic arrival. Right, the experimental fraction of correlated events as a function of total number of time-ordered events. Data are still in black circles and the 1 σ and 2 σ uncertainties of the observed value are given in the blue shaded area. The isotropic expectation value 21% is shown in a red horizontal dotted line. From [99].

ergies. Since proton is more penetrating in the atmosphere, the events observed with large X_{max} are dominated by protons. Hence the shape of the tail of the X_{max} distribution is very sensitive to the proton-air cross section, a technique first used in Fly's Eye Experiment [100, 101]. Hybrid data are used to get an accurate measurement of X_{max}. The energy range chosen here is from 10^{18} eV to $10^{18.5}$ eV for the reason of large statistics, substantial proton fraction and a high center of mass energy of 57 TeV, much higher than LHC could achieve [103].

The method to calculate the proton-air cross section has two steps. The first step is to find an air shower observable sensitive to the cross section to compare with the simulation. The second step is to convert this observable to an estimate of the proton-air cross section. The shape of the tail of the X_{max} distribution can be described by an exponential function $dN/dX_{max} \propto exp(-X_{max}/\Lambda_\eta)$, where η is the fraction of the most deeply penetrating air showers. The observable used for the cross section calculation is the tail shape constant Λ_η [102]. η is chosen to be 20 % for two consideration, to ensure large enough proton fraction in the tail and keep enough events for good statistics.

The PAO data used is between December 2004 and September 2010. The quality cuts

similar to the $\langle X_{max} \rangle$ and RMS(X_{max}) are used and leave an original data set of 11628 events. Additional fiducial cuts are used to extract a data set to have an unbiased X_{max} distribution. A total of 2082 events passed all the cuts, out of which 783 events are in the range of 768 g/cm^2 to 1004 g/cm^2, which directly contribute to the measurement of Λ_η. The average energy of the 783 events is $10^{18.24}$ eV, which corresponds to a center of mass energy of $\sqrt{s} = 57$ TeV for proton-proton collision. The fitting result is shown in Figure 3.28.

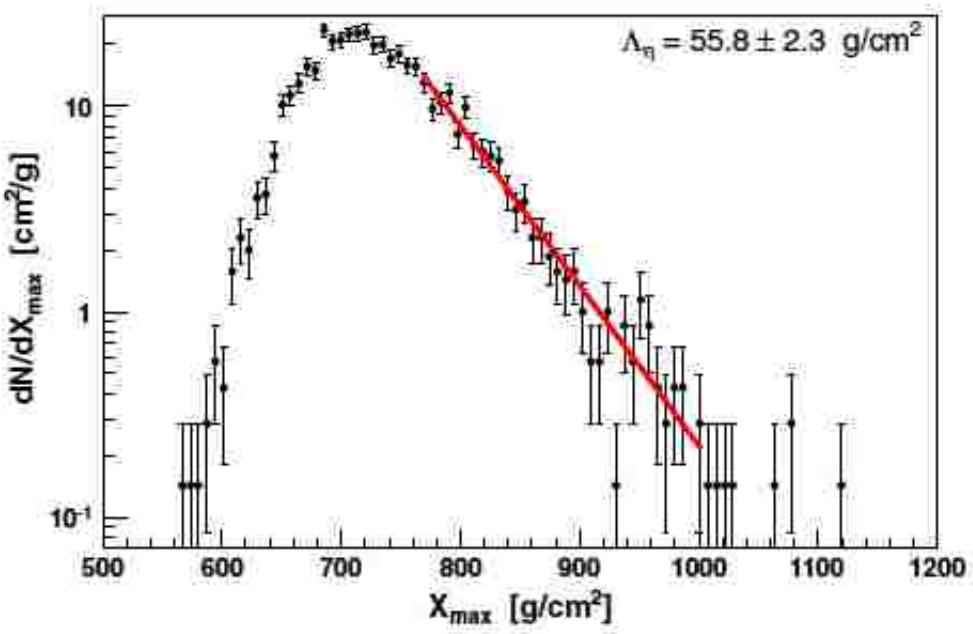

Figure 3.28: Unbinned likelihood fit of Λ_η to the tail of X_{max}. From [102].

The fitting parameter obtained is

$$\Lambda_\eta = 55.8 \pm 2.3(stat) \pm 1.6(syst)\,\mathrm{g/cm^2} \tag{3.15}$$

To convert parameter Λ_η to the proton-air cross section σ_{p-air}, one needs to rely on the Monte Carlo simulations. The value Λ_η derived from the fitting are directly related to σ_{p-air} used in the simulation. Figure 3.29 shows the conversion curves between Λ_η and σ_{p-air}. The four popular hadronic models used in the simulation are QGSJET01 [104], QGSJETII.3 [105], SIBYLL2.1 [106] and EPOS1.99 [107]. The proton-air cross sections obtained from the conversions are 523.7, 502.9, 496.7 and 497.7 mb , respectively, with a

same statistical uncertainty of 22 mb for each model [102].

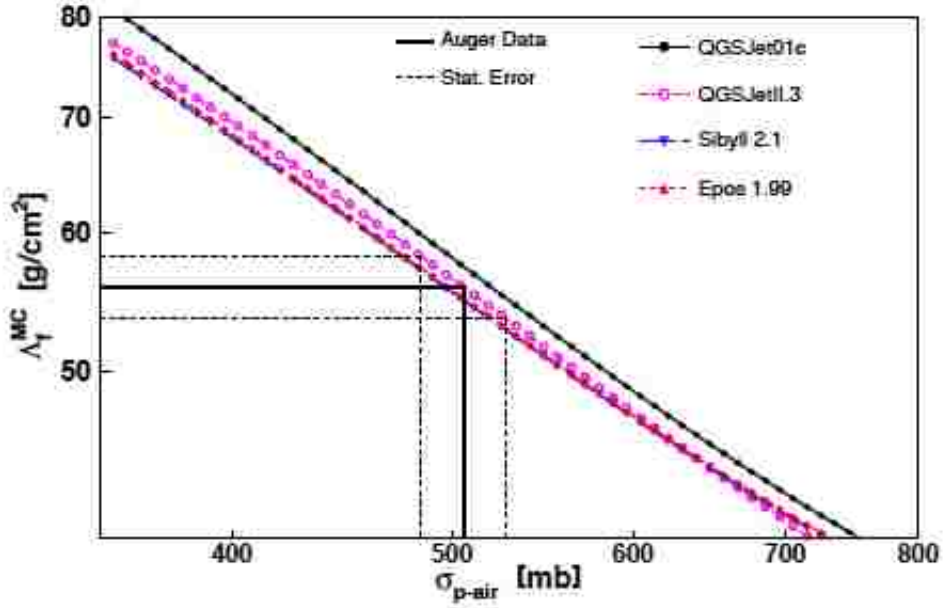

Figure 3.29: The conversion between Λ_η and σ_{p-air} for different simulation models. The example auger conversion line from QGSjetII model is indicated in the black solid line and the dashed line is the the statistical error. From [103].

While none of these models give a completely accurate description of all shower features, they are reasonably good in most of their main features. The differences between models are generally bigger than using the same model with different variables. The uncertainties of the final σ_{p-air} take into account Λ_η uncertainties, different hadronic interaction models, energy scale, conversion between the Λ_η and σ_{p-air}, different photon and helium fraction. The final result of the proton-air cross-section is calculated by averaging between the cross section values from the four hadronic models [102],

$$\sigma_{p-air} = 505 \pm 22(stat) \, ^{+28}_{-36}(syst) \, \text{mb} \tag{3.16}$$

This cross-section corresponds a center of mass energy of $57 \pm 0.3(stat) \pm 6(syst)$ TeV. Figure 3.30 shows the comparison of this result with different model predictions and other published results at lower energies.

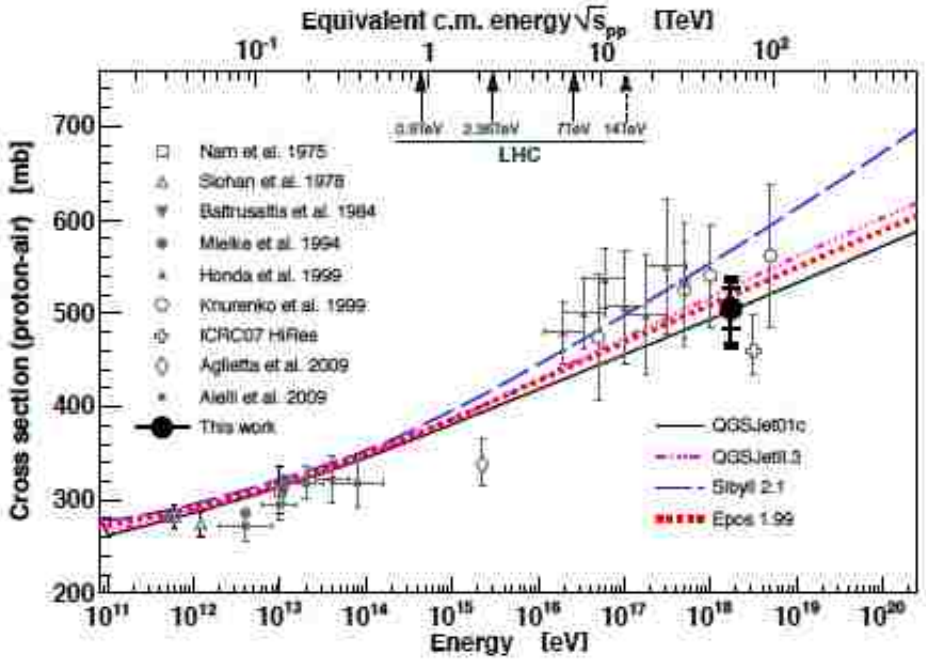

Figure 3.30: The PAO σ_{p-air} compared with different model predictions and other published results from previous experiments. The inner error bars are statistical only while the outer one include all systematic uncertainties for a helium fraction of 25 % and 10 mb photon systematics. From [103].

The proton-air cross section can also be converted to proton-proton cross section and the result agrees with a straightforward extrapolation of the LHC energies to 57 TeV for a limited side of models, more details can be find at [102].

4. Surface Detector FADC Peak Finding Method

4.1 Introduction

The surface detector (SD) array of Pierre Auger Observatory (PAO) has been collecting a huge amount of data every day. It has been discussed in Section 2.5 that the "foot prints" of the extensive air showers on the ground are mainly muons and electromagnetic particles. These particles are detected by the SD because of the Cherenkov light they emitted in the water tank. The signals are converted into the FADC traces stored in the PAO SD data. The shape and timing of FDAC traces contain major information for the study of cosmic ray composition and the hadronic physics at the highest energy level. However, in the FADC traces, the muon signal and the electromagnetic signal are mixed together.

The purpose of my work is to study new ways to quantify the electromagnetic and muon parts of extensive air showers on an event by event basis. I will use this information to attempt to assess the composition of cosmic rays as a mixture of heavy nuclei and protons and to study whether the "leading particles" of hadron interactions can be identified using muons and multiple shower fronts or "shells".

4.2 Hadronic Physics at Highest Energy Level

After an ultra-high energy cosmic ray (UHECR) enters in the earth's atmosphere, the primary particle collides with an atmospheric nucleus. There is not much knowledge about hadronic physics at this energy level because it is beyond the reach of any terrestrial particle accelerator (see Figure 2.1). We can only make extrapolations according to our knowledge at lower energies. One of the most interesting physics topics in hadronic interactions is "leading particle physics".

4.2.1 Leading Particle Physics

In any high energy interaction, there is a significant probability that one of the secondary particles emerges carrying a significant fraction of the primary particle energy. Consequently it causes a second big shower of its own.

This phenomenon will have two significant observable characteristics on the PAO detectors:

1. On the FD side, the shower profile may look different. If the leading particle travels far enough before interacting, we may see a "double bump" shower instead of the typical "one bump" normal shower.

2. On the SD side, we may see multiple shower fronts or "shells".

4.2.1.1 FD "Double Bump" Events

As discussed in Section 2.5.2.1, FD shower profiles are reconstructed with the Gaisser-Hillas (GH) function (see equation 2.37). The size of shower increases until it reach the shower maximum and then decreases. Reflected in GH function, the shape of a shower profile looks like a "bump" (see Figure 2.12). If the leading particle does not interact until it travels another few hundred g/cm^2 in the atmosphere, the FD shower profile will look like two well-separated showers traveling a long the same axis and overlapping each other, thus has a shape of a "double bump".

In order to find these events, our method includes the following procedures.

1. First, we select the events with a poor quality GH fit (with large χ^2), which may indicate the standard GH fit (which uses on "bump" only) not suitable for these events.

2. Second, we fit these events with two GH functions and check to see if any of those fits has an improved χ^2.

3. For the events that have good two-GH fit but bad one-GH fit, we check the cloud data from different atmosphere monitoring databases (discussed in Section 3.5) and exclude

the cloudy nights, because sometimes clouds overshadow the middle part of the shower causing some double bump like events.

Figure 4.1 shows an example event of double-bump shower profile we found. The χ^2 for one and two GH fit is 439 and 181 respectively, it is clear that for this event two GH fit is better.

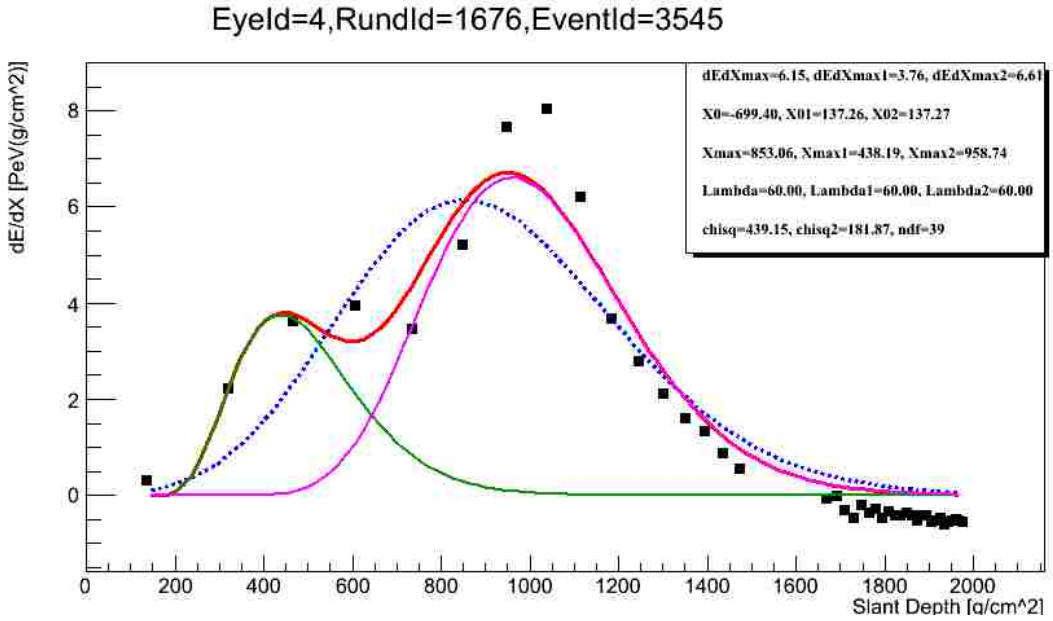

Figure 4.1: Example of a double-bump shower profile. The black squares are the FD data. The blue dashed line represents one GH function while the red solid line is the two GH fit. The thin green and magenta lines represent the fitted first and second shower profile. Courtesy Azadeh Keivani.

4.2.1.2 SD "Double Shell" Events

As suggested in Section 2.5.2.2, during the EAS development, the number of particles in the shower increases and spreads out. Even though the primary particle's ultra-high energy is split among millions of particles, the particles still have a very high energy and have a speed very close to the speed of light. So by the time the relativistic particles reach the ground, a nearly spherical shower front is observed. Figure 4.2 gives a schematic diagram of the spherical shower front.

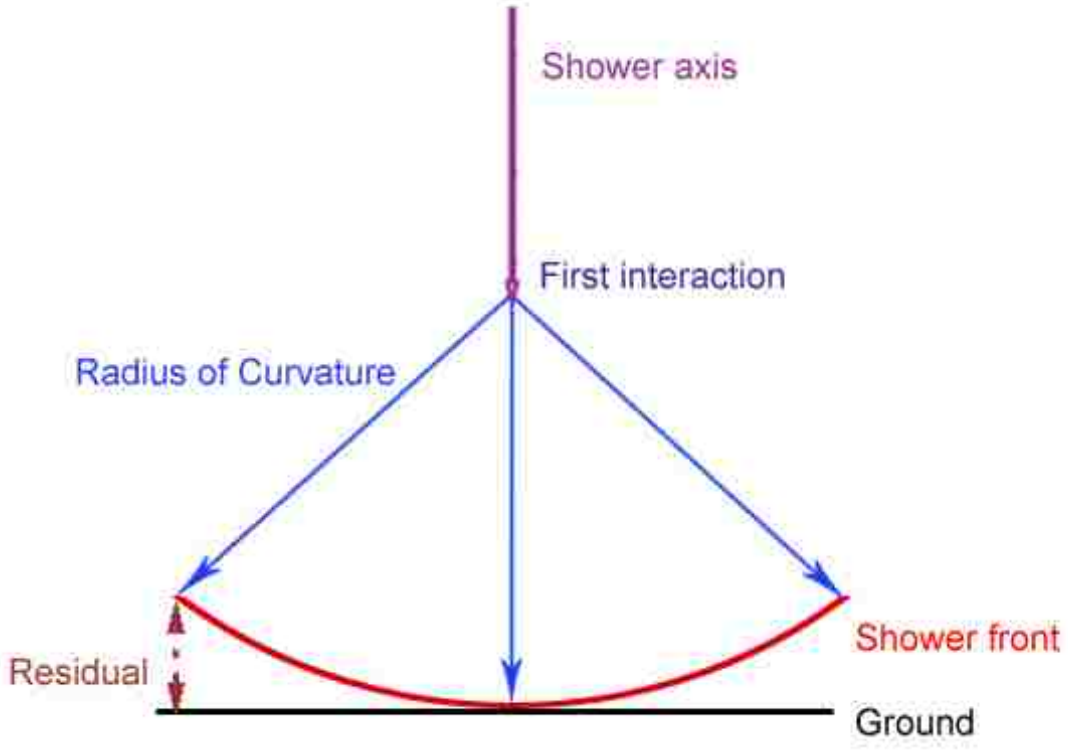

Figure 4.2: Schematic diagram of the spherical shower front of a vertical shower.

When we fit the shower front with a sphere, the radius we get is called the radius of curvature R_c. The R_c is obtained by minimizing the the χ^2 function of

$$\chi^2 = \sum_{i=1}^{n} \frac{[c\,(t_i - t_0) - |\vec{R_c}\,\vec{a} - \vec{x_i}|]^2}{c^2\,\sigma^2(t_i)} \tag{4.1}$$

where n is the number of stations triggered, t_0 and $\vec{x_0}$ are the initial time and position of the signal weighted barycenter, t_i and $\vec{x_i}$ are the reported time and position of ith station, $\vec{a}$ is the unit vector of the shower axis and $\sigma^2(t_i)$ is the uncertainty of t_i [74].

The leading particle from the first interaction travels and creates a second big shower. This shower starts later and deeper in the atmosphere, i.e., closer to the ground, consequently the second shower front (shell) has a smaller radius of curvature. If the major secondary particle travels a long distance before it creates a shower of its own, the separation between the shells would be distinguishable. Figure 4.3 presents the schematic geometry of a double shell event.

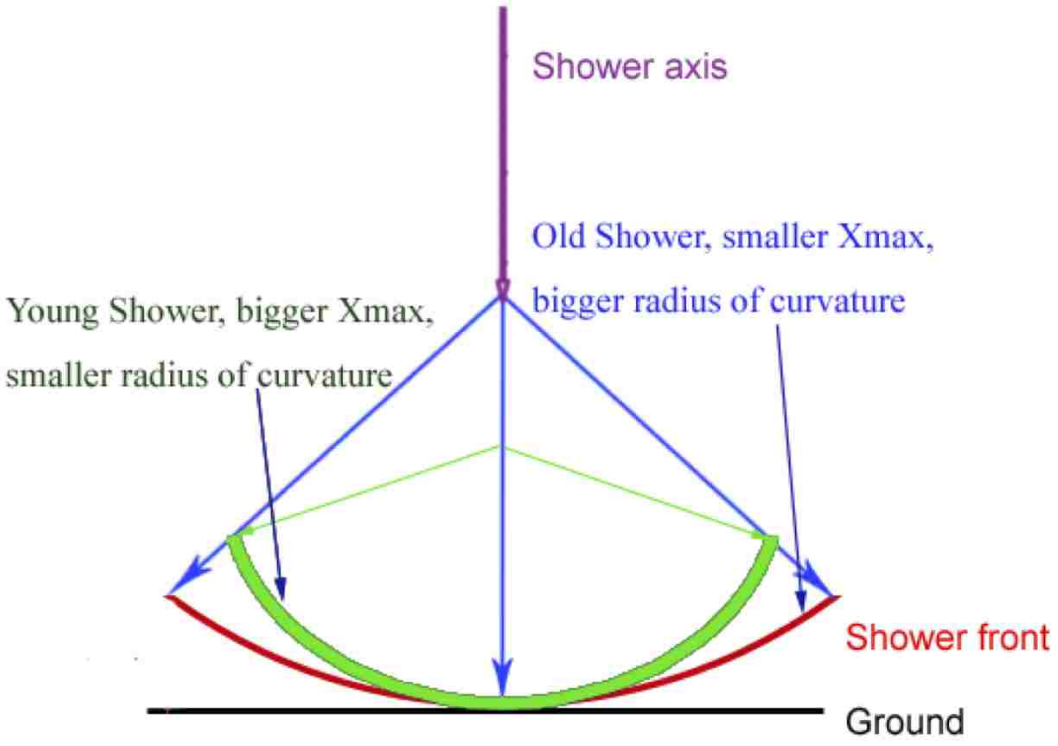

Figure 4.3: Schematic diagram of a double shower front geometry. The original shower, starts higher in the atmosphere, has a smaller X_{max} and larger radius of curvature. The secondary shower, starts deeper in the atmosphere, has a larger X_{max} and a smaller radius of curvature.

In PAO's official Offline [110] reconstruction, first a plane shower front is fitted. The fitted plane passes the stations in a time that is different from the reported station GPS time. For the station near the shower axis, the reported time is very close to the fitted time, the delay time is rather small. One the other hand, the station far away from the shower axis has a larger time delay. The time delay is called time residual (in the order of hundreds of nano seconds). Figure 4.4 shows the time residual distribution.

The time residual can be used for our fit of the curvature shower front. The corresponding SD event to the FD event in Figure 4.1 has the time residual plot shown in Figure 4.5.

The muons and EM particles have different signal response in the PAO surface water Cherenkov detector. Muons have higher energy and larger mass than electrons, so they

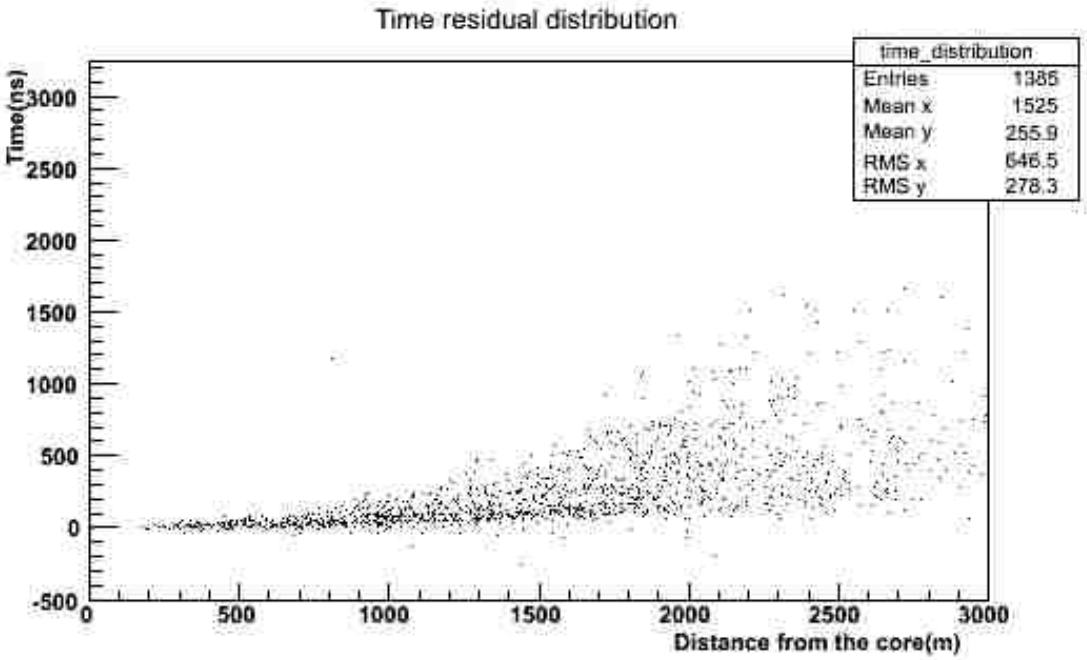

Figure 4.4: The shower plane time residual distribution with the station distance from the shower axis. The further away the station is, the bigger the time delay is. Plotted from 2007 PAO SD data.

travel almost in a straight line while the EM component's propagation is more diffusive because they undergo a great deal of multiple scattering. Thus, the muons will arrive earlier than the electrons and with less time spread. Also, a muon carries and deposits significantly larger energy in the water tank than the EM particles. Therefore, the FADC signal for a muon is bigger, sharper and narrower than the EM part. Figure 4.6 gives an example of the simulated FADC traces of muonic component and EM component.

Usually the narrow sharp peaks are muons and they are the main components of the shower front because they arrive the earliest. So if we can find the peaks in the total FADC traces, these may give you the arrival timing information of the shower fronts. Then the next step is to find the first and second peaks in the FADC traces.

Here is my peak finding procedure.

1. Find the maximum signal in the 768 FADC time bins.

2. Use 30% of that signal or 0.5 Vem as a cut, whichever is larger. The purpose of this

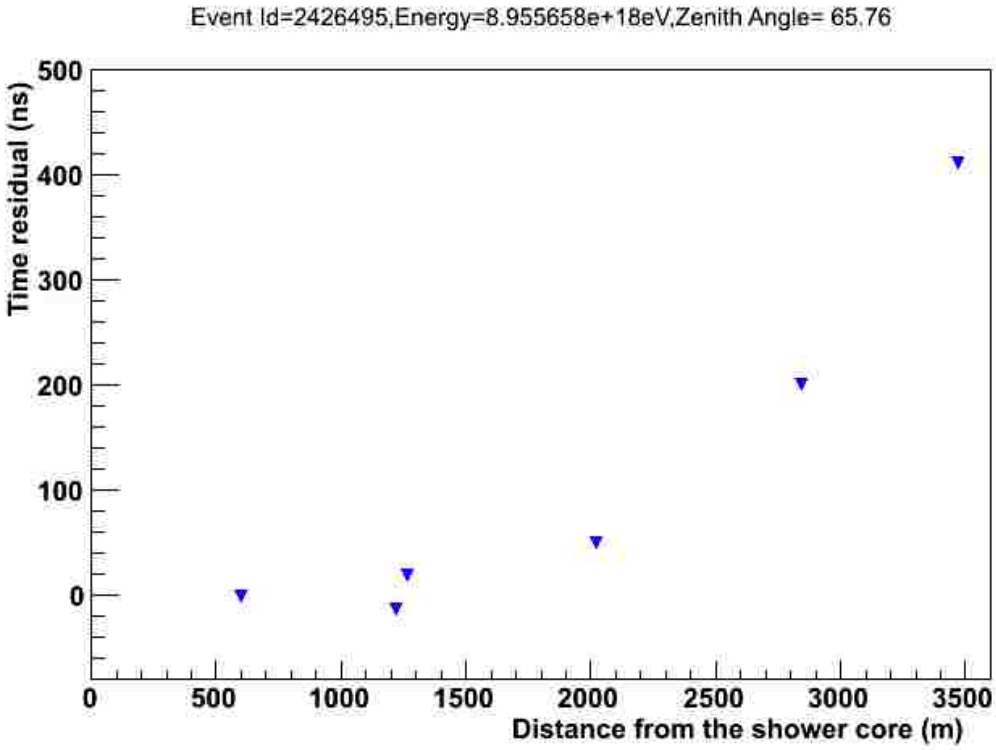

Figure 4.5: The shower plane time residual of SD event corresponding to the FD event shown in Figure 4.1. The blue points are the time fall behind the fitted shower plain with the increase of the distance from the shower core.

cut is to reduce or eliminate false peaks coming from background fluctuations.

3. Find the first peak that passes signal size cut and is larger than both the previous and following 4 bins. Furthermore, the peak bin must be "sharp", defined as the largest difference between the peak bin and any of the pervious or following three bins needs to be larger than 30% of the peak signal.

4. After the first peak is found, search for the second peak, starting from some minimum separation from the first one. The purpose of adding the separation is to ignore the close-by peaks caused by muons following the first one very closely and in the first shower front group. The selection of separation is important. It need to large enough to avoid identifying muons from the first shower front group but not too big so that the muon peaks from the second shower front group are not ignored. The amount used

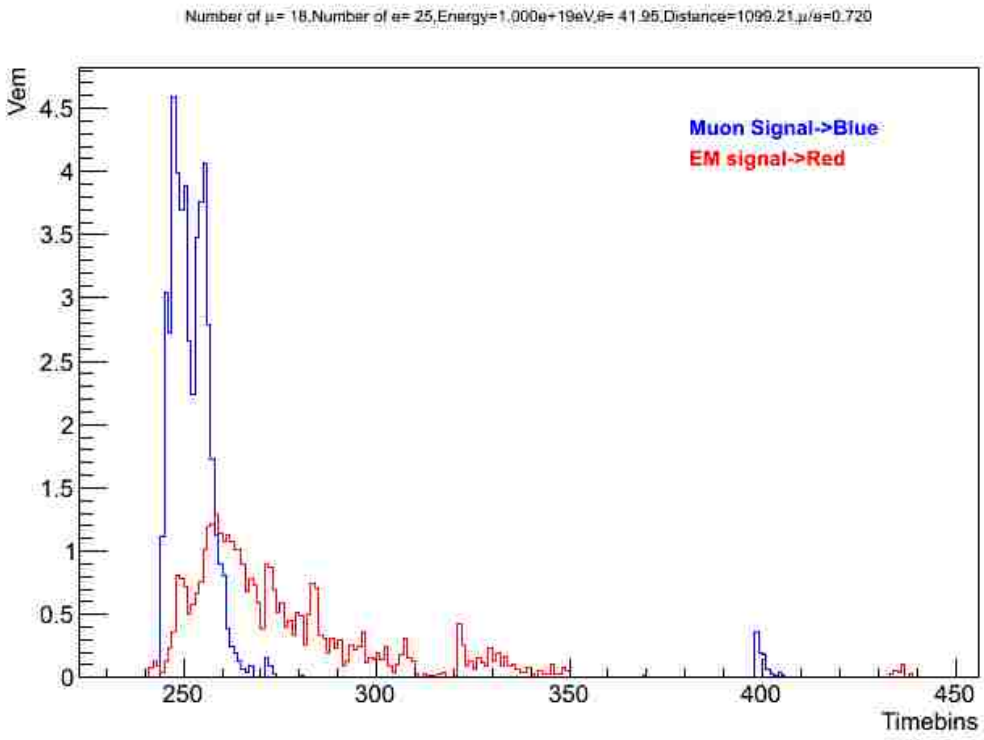

Figure 4.6: Simulated FADC traces of a surface detector 1.1 km away from the shower axis of a 10 EeV iron primary shower, showing the muonic and EM component. The blue trace is the muon signal and the red trace is the EM signal. The muonic signal is sharp and narrow while the EM signal is more diffusive in time.

here is 8 bins, corresponding to 200 ns.

Most detectors have a signal passing the first peak criteria. The first peak represents the first shower front signal group that passed the triggers. Their positions in the FADC traces are similar to each other (see Figure 4.7).

Figure 4.8 shows an example of the peaks selection in the FADC trace of one of the stations in the SD event referred in Figure 4.5.

The time separation between the two peaks can be calculated as the product of the difference between the peak bin numbers and the time per bin, which, in this case, is 25 ns (The FADCs used in PAO SD operate at 40 MHz.). Figure 4.9 shows the magnified version of the time separation between the two peaks found.

As discussed before, the muons travel in a straight line with a speed of "c". This allows

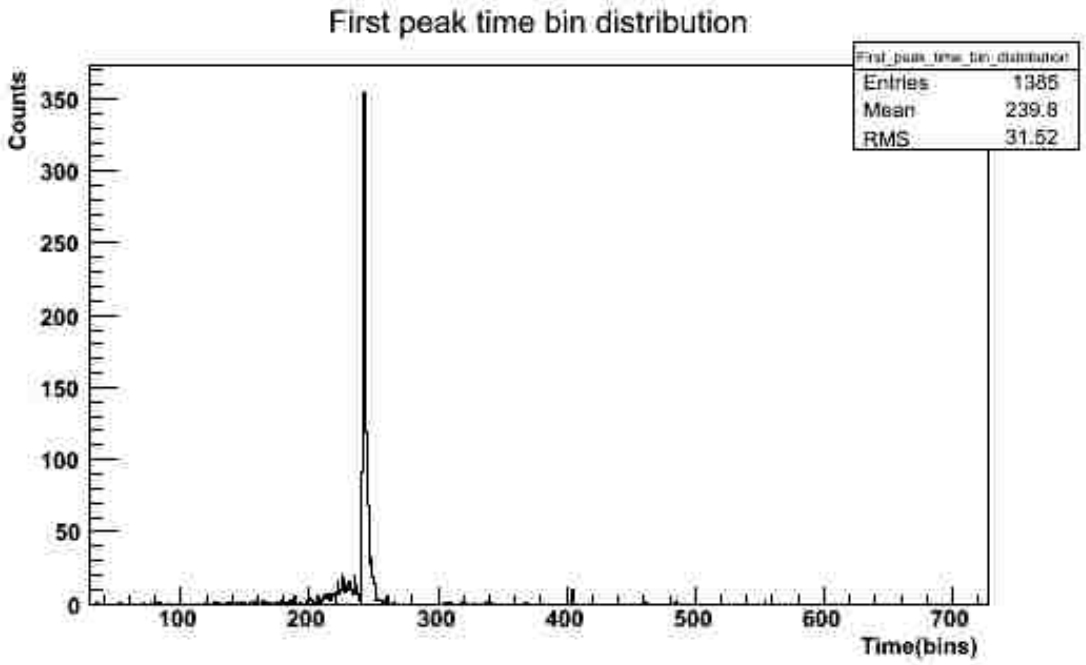

Figure 4.7: The first peak time bin position distribution in FADC traces. Most of them are at around time bin 250. Plotted from PAO 2007 SD data.

us to convert the time separation into distance separation. This distance separation is added to the distance residual plot to fit a potential second shower front. For example, the 950 ns separation in Figure 4.9 corresponds to a distance of 285 m. Then I fit the first and second peak groups in the distance residual plot with two spherical shower fronts. At least 3 data points for each peak group are required for the shower front fits. The fitting results are shown in Figure 4.10. The first shower front has a radius of curvature of 57 km and the second one has a radius of curvature of 13 km.

4.2.2 Connect SD with FD

4.2.2.1 The Normal Events

The first thing to check is whether the SD radius of curvature is correlated with the FD shower start point. I use two ways to check that:

1. From FD to SD

   Find the shower start point in the FD shower profile and convert it to the distance

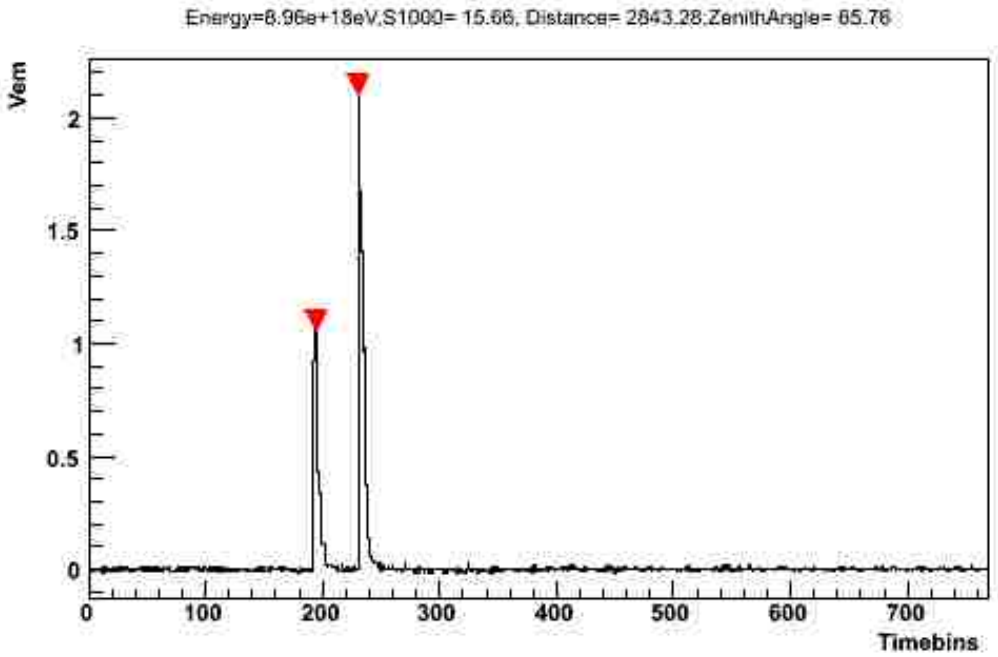

Figure 4.8: The FADC trace of the station at 2843 m from the reconstructed shower core in the event shown in Figure 4.5. One time bin equals 25 ns. The two red markers are the two peaks I found in this trace following the peak finding procedure. The signal size cut here is 30% of the largest bin ($\sim$ 0.6 Vem) since it is larger than 0.5 Vem cut.

from the start point to ground. Compare this distance to the fitted SD shower front radius of curvature.

2. From SD to FD

   Convert the fitted SD radius of curvature to FD slant depth. Check the age of this slant depth to see if the corresponding point is before the shower maximum.

4.2.2.1.1 From FD to SD

First, I try to find the location where the shower starts in the atmosphere from FD. I define the point in the shower profile where the shower size reaches 20% of the shower maximum as the shower start point, see Figure 4.11 for an example.

After that I convert that shower start point atmosphere depth X (in g/cm^2) into the distance from the shower start point to ground d_X (in km) with this relation:

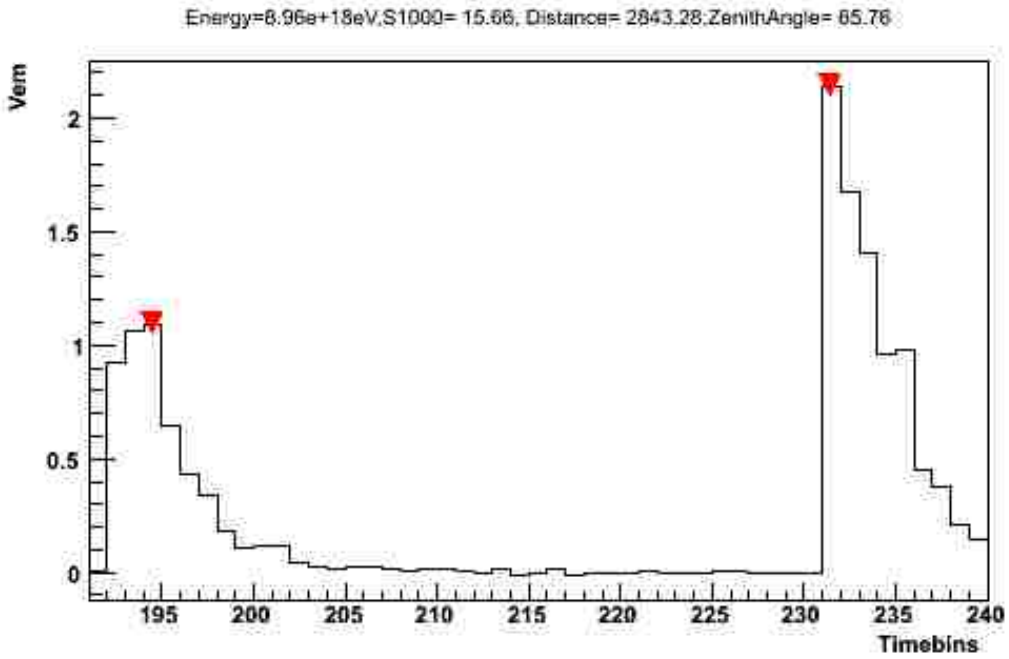

Figure 4.9: Separation of FADC trace peaks. The separation of the two peaks at this station is about 38 bins, corresponding to 950 ns in time and 285 m in distance. This FADC trace is a zoomed-in version of Figure 4.8.

$$d_X = \frac{8.3}{\cos\theta} \ln\left(\frac{880\,\mathrm{g/cm^2}}{X\cos\theta}\right)\ \mathrm{km} \tag{4.2}$$

where θ is the zenith angle of the reconstructed shower axis and 880 g/cm^2 is the atmosphere depth of PAO. This relation is derived from the standard atmosphere model (an exponential with scale height 8.3 km). Then I make a scatter plot of the radius of curvature R_c and the distance of the start point to the ground d_X. See Figure 4.12 for the result. There is obvious correlation between these two quantities.

The linear fit in Figure 4.12 gives the relations between the two quantities:

$$d_X = (1.12\,R_c \pm 4.3)\,\mathrm{km} \tag{4.3}$$

4.2.2.1.2 From SD to FD

I reflect back to the calculated shower curvature R_c and convert it back into the atmosphere

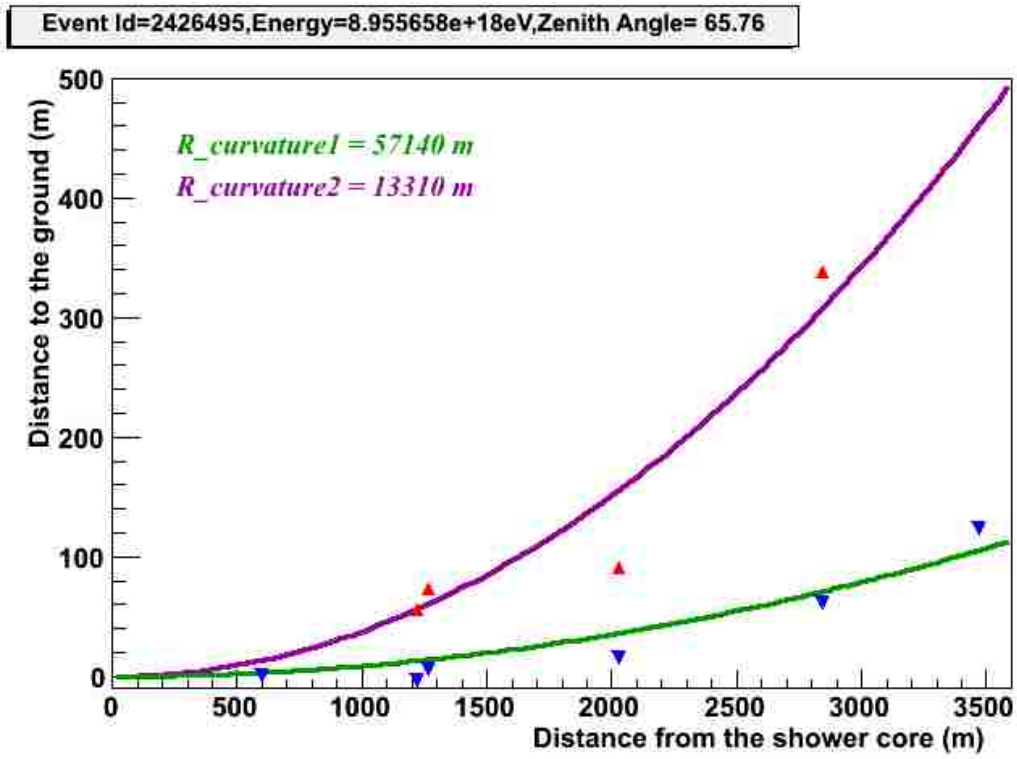

Figure 4.10: SD double shell events demonstration. The blue downward-pointing triangles are from the shower plain time residual (Figure 4.5). The red upward-pointing triangles are from the added separations between the first and second peaks found. The green shell is the fitted first shower front, which started higher in the atmosphere, thus having a larger radius of curvature. The purple shell is the fitted second shower front, which was created by the leading particle deeper in the atmosphere, thus having a smaller radius of curvature.

depth X_R with this relation:

$$X_R = \frac{880}{\cos\theta} \exp\left(-\frac{R_c \cos\theta}{8.3\,\mathrm{km}}\right) \ \mathrm{g/cm^2} \tag{4.4}$$

where θ is the zenith angle of the reconstructed shower axis. This relation is equivalent to equation 4.2. Figure 4.13 shows an example for the calculation of the corresponding atmosphere depth X_R.

In order to confirm that the projected point corresponds to the "start" of the shower (at least in some sense of the term), I calculate the corresponding shower age to the fitted radius of curvature. The shower age s is a parameter to describe the shower development stage. It

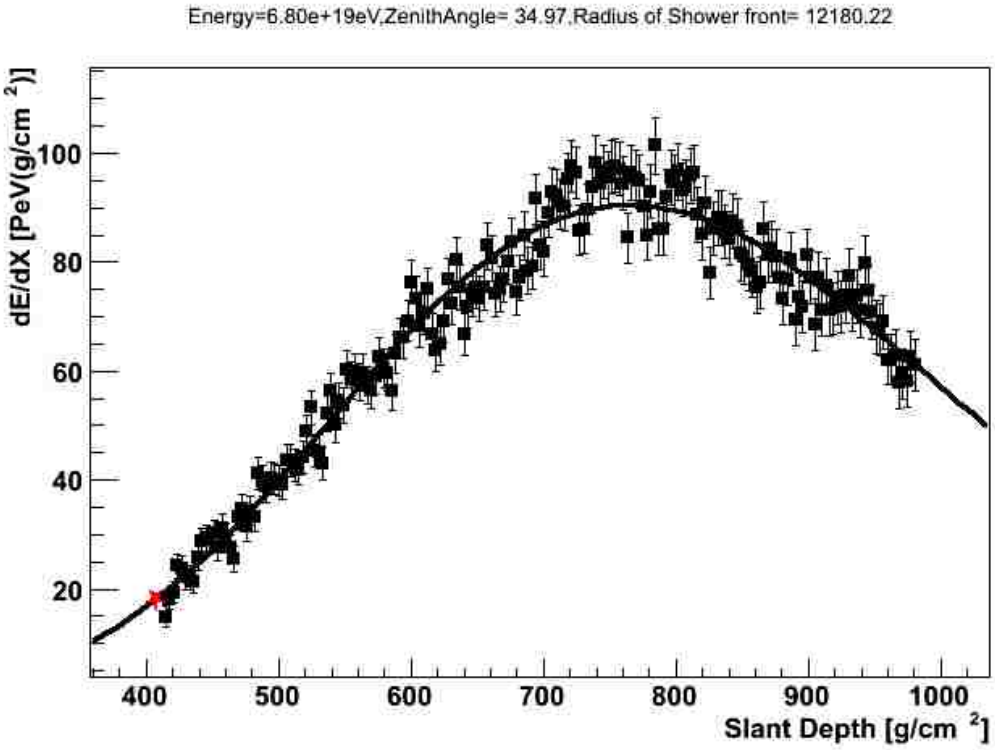

Figure 4.11: Example of calculation of the shower profile start point. First, I got the energy deposit maximum from the trace. Then I calculate the 20% value as the energy deposit value of the start point. Then I refer to the GH function to calculate the corresponding slant depth X. In this example, the slant depth corresponding to the calculated start point (marked by the red star) is about 410 g/cm^2.

is defined as: [36]

$$s(X) = \frac{3X}{X + 2X_{max}} \tag{4.5}$$

where X is the slant depth in the atmosphere and X_{max}, as mentioned in Section 2.5.1, is the slant depth where the shower reaches its maximum. From its definition, we can see the shower age has these meanings:

$$s \begin{cases} < 1 & \text{if } X < X_{max}, \text{ the shower size is growing} \\ = 1 & \text{if } X = X_{max}, \text{ the shower size reaches its maximum} \\ > 1 & \text{if } X > X_{max}, \text{ the shower size is decreasing} \end{cases}$$

For each shower similar to the example in Figure 4.13, I convert the slant depth (corresponding to the radius of shower curvature) to the shower age. Figure 4.14 shows the distribution of the shower ages. The mean of the shower age is 0.68, suggesting that most of

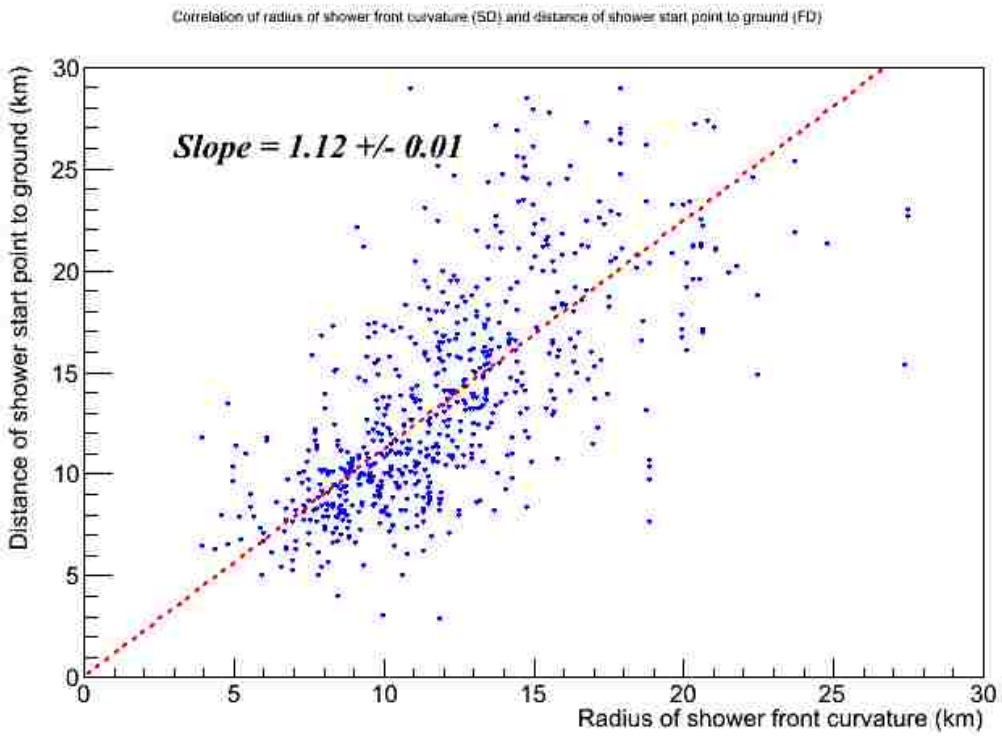

Figure 4.12: Correlation between calculated shower radius of curvature and calculated distance from shower start point to ground. There seems to be clear correlation here. Plotted from PAO 2007 hybrid data.

the fitted shower curvature circles have origins on the shower development stage. The distribution of ratios of the shower size (corresponding to the fitted shower radius of curvature) to the shower maximum is shown in Figure 4.15. The mean of the ratio is about 37 %.

4.2.2.2 Double Shell Event Candidates

SD event 2426495 discussed in Section 4.2.1.2 corresponds to FD event 3545 in Section 4.2.1.1. These two are in the same hybrid event. Now we will use the two methods discussed in Section 4.2.2.1 to check the relations between these two events.

4.2.2.2.1 From FD to SD

From the information in Figure 4.1, the first and second shower profiles are described by two

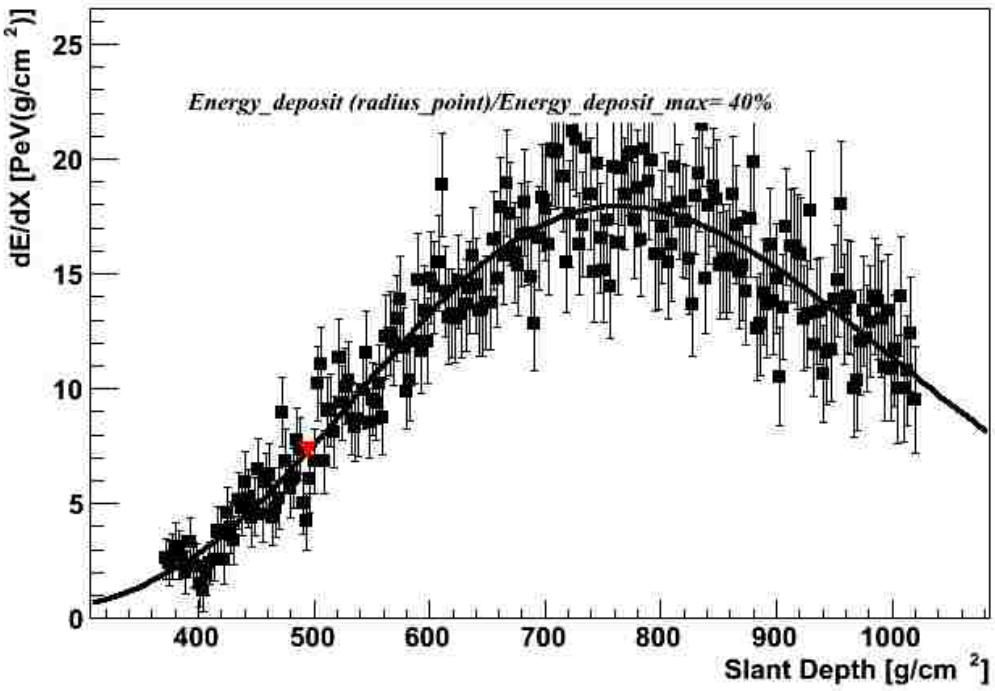

Figure 4.13: An example of converting the calculated shower curvature to the shower longitudinal profile. In this example, the corresponding slant depth (marked by red triangle) to fitted shower front radius of shower curvature is $\sim$ 500 g/cm^2. The corresponding shower size is about 40 % of the shower maximum.

GH functions listed as

$$\begin{aligned} \frac{dE}{dX} &= 3.76 \left(\frac{X - 137.26}{300.93}\right)^{5.02} \exp\left(\frac{438.19 - X}{60}\right) \frac{\text{PeV}}{\text{g/cm}^2} \\ \frac{dE}{dX} &= 6.61 \left(\frac{X - 137.27}{831.47}\right)^{13.86} \exp\left(\frac{958.74 - X}{60}\right) \frac{\text{PeV}}{\text{g/cm}^2} \end{aligned} \tag{4.6}$$

From equation 4.6, the "start points" (i.e., the slant depth for 20% of the full magnitude) in the two GH function can be calculated as $X_1 = 256.72\,\text{g/cm}^2$ and $X_2 = 622.03\,\text{g/cm}^2$ respectively. Substitute these two values in equation 4.2, we have the corresponding radii of curvature to the the first and second "bump" as $d_{X1} = 42.90$ km and $d_{X2} = 25.01$ km. The fitted radii of curvature for the double shells in Figure 4.10 are $R_{c1} = 57.14$ km and $R_{c2} = 13.31$ km respectively. Comparing d_{X1}, d_{X1} to R_{c1}, R_{c2}, we would put two points (57.14, 42.90) and (13.31, 25.01) in Figure 4.12. As can be seen from the Figure, these two

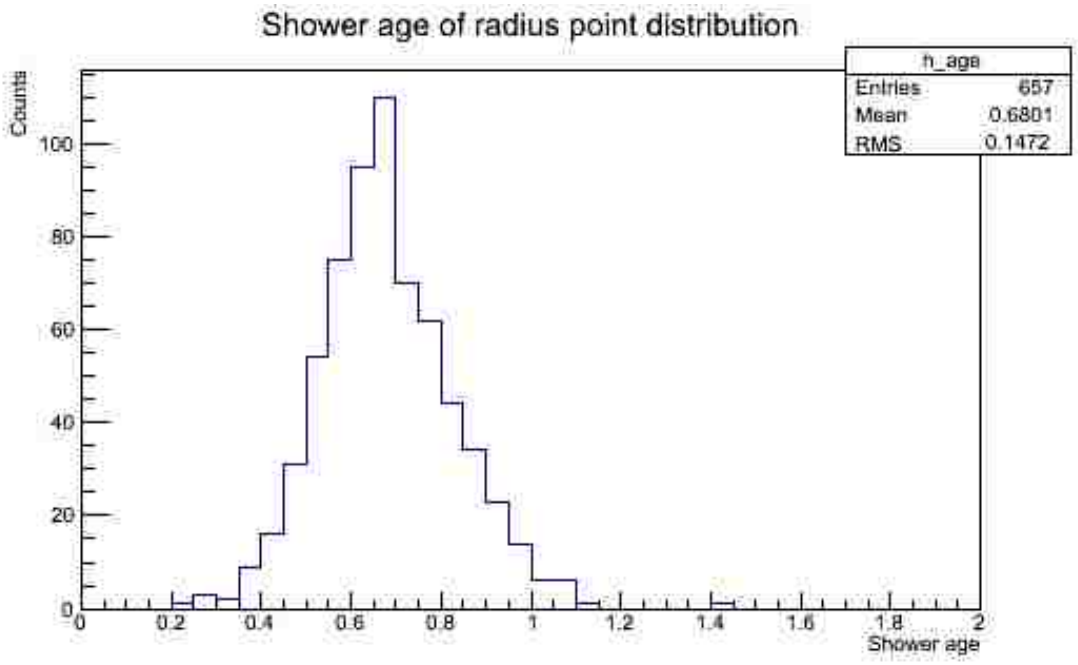

Figure 4.14: Distribution of the shower ages corresponding to the fitted radii of curvature. Most of the ages are below 1, indicating that most of the fitted shower curvature circles have origins on the shower development stage. Information gathered from PAO 2007 hybrid data.

points obey the correlation relation reasonably well.

4.2.2.2.2 From SD to FD

From equation 4.4, we can calculate the slant depths corresponding to the two fitted radii of curvature as $X_{R1} = 126.94$ g/cm^2 and $X_{R2} = 1109.62$ g/cm^2 respectively. From Figure 4.1, the depths of shower maximum of the two showers are $X_{max1} = 438.19$ g/cm^2 and $X_{max2} = 958.74$ g/cm^2 respectively. Substitute these two values into equation 4.5, we can calculate the respective shower ages as $s_1 = 0.38$ and $s_2 = 1.10$. These two shower ages are within the limit of the distribution in Figure 4.14.

4.2.3 Leading Particle Cross Section Implications

Once we confirm that the SD radius of curvature and FD slant depth are correlated, we can use the SD double shell events to study the leading particle cross sections. PAO SD data used

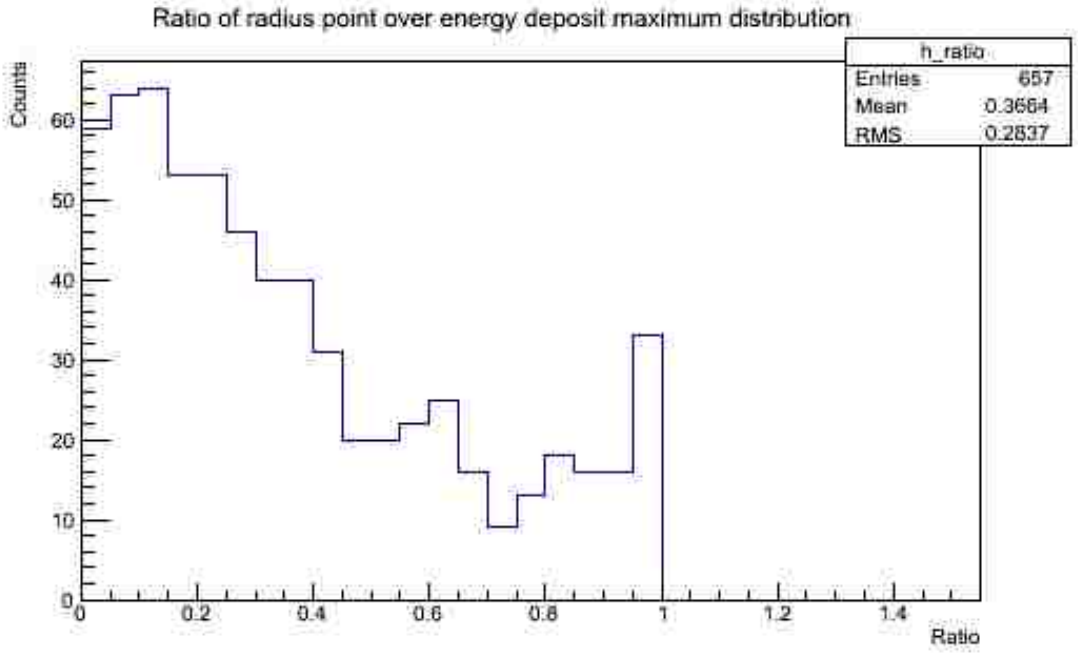

Figure 4.15: The ratio of the shower size (corresponding to the fitted shower radius of curvature) to the shower maximum distribution. The mean is about 50 %. Information gathered from PAO 2007 hybrid data.

here are between January 2004 to April 2011 and downloaded from Auger Observer [109]. They are reconstructed with the official $\overline{\text{Off}}\underline{\text{line}}$ [110] version v2r6p4 and stored in ADST data format [109].

The following cuts are made during the event selection and shower fronts fitting:

- Energy Cut

  The reconstructed energy range needs to be in the range of $18.0 \leq logE \leq 19.6$.

- Event Quality Cut

  Every PMT need to have a trace, so we discard stations that have one or two PMTs malfunctioning, to ensure better signal detection quality.

- Distance Cut

  The distance from the surface station to the shower axis need to be within 5 km.

- Signal Size Cut

The maximum peak in the FADC trace needs to be < 5000 VEM. The purpose of this cut is to eliminate the events where the PMTs begin to saturate when recording a large signal. The background noise can be very big and may be mistakenly considered to be a muon signal.

- Number of Stations Cut

  Event needs to have at least 4 stations for the first shower front fit and 3 stations for the second shower front fit. The purpose is to ensure the quality of the shower fronts fitting.

The peak finding procedure and shower front fitting procedure follow the discussion in Section 4.2.1.2. A total of 2523 events are fitted reasonably well with two shower fronts. The fitted radii of curvature of the two shower fronts (R_{c1} and R_{c2}) are converted to FD slant depths (X_{R1} and X_{R2}) with equation 4.4. The difference of the two slant depth ΔX = X_{R2} - X_{R1} is calculated for each event. The distribution of ΔXs is shown in Figure 4.16. The distribution between 300 g/cm^2 to 700 g/cm^2 looks exponential. The function I used for the fit is

$$N(\Delta X) = A \exp\left(-\Delta X/\lambda\right) \tag{4.7}$$

where $N(\Delta X)$ is the number of events at slant depth difference ΔX, A is a normalization factor and λ is the expected interaction length. The fitting gives a result of $\lambda = 119.9 \pm 4.8$ g/cm^2.

Considering the relation we obtained in equation 4.3, we apply the factor 1.12 to fitted radii of curvature (R_{c1} and R_{c2}) and convert them to the distances of the shower start point to the ground (d_{R1} and d_{R2}). Then we convert d_{R1} and d_{R2} to to FD slant depths (X_{d1} and X_{d2}) with equation 4.4. The modified ΔX = X_{d2} - X_{d1} is calculated for each event. The distribution of modified ΔXs is shown in Figure 4.17.

The fitting of modified ΔXs distribution gives a result of $\lambda = 121.9 \pm 4.8$ g/cm^2, which is not much different from the previous result. This is not surprising because even though

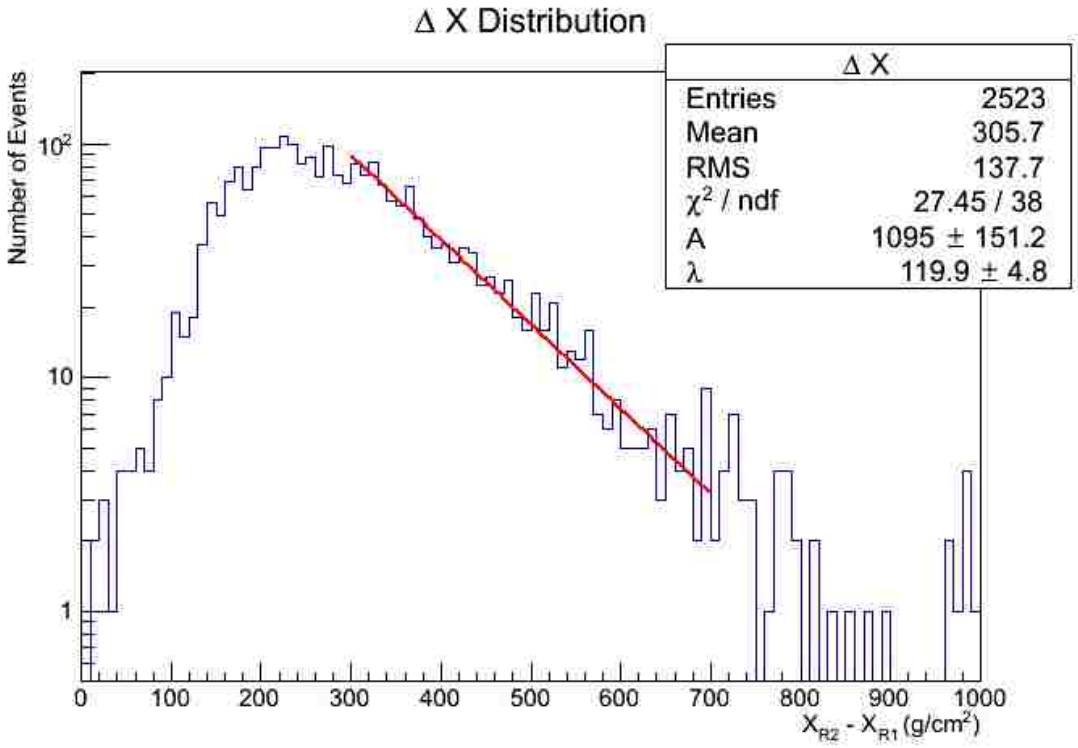

Figure 4.16: ΔX distribution. The red line represents the exponential fit.

the factor 1.12 make the difference in d_{R1} and d_{R2} larger than that of R_{c1} and R_{c2}, it also push the two corresponding radius of curvature points to the higher atmosphere, where the particle density is smaller.

4.3 Discussion and Summary

The peak finding method works well for the stations more than 1 km away from the shower axis but below 1 km, the EM component is overwhelming the muon content (Section 5.5) that increases the difficulties of finding the second peak in the close range . So the method needs some adjustment within the 1 km range or, if there is enough stations triggered beyond 1 km, one can throw away the stations below 1 km and still get good radius of curvature fit for the second shower front.

We find that the fitted SD radius of shower front curvature indeed correlates with the FD longitude profile (see Figure 4.12 and Figure 4.14), which provides basis for the hybrid

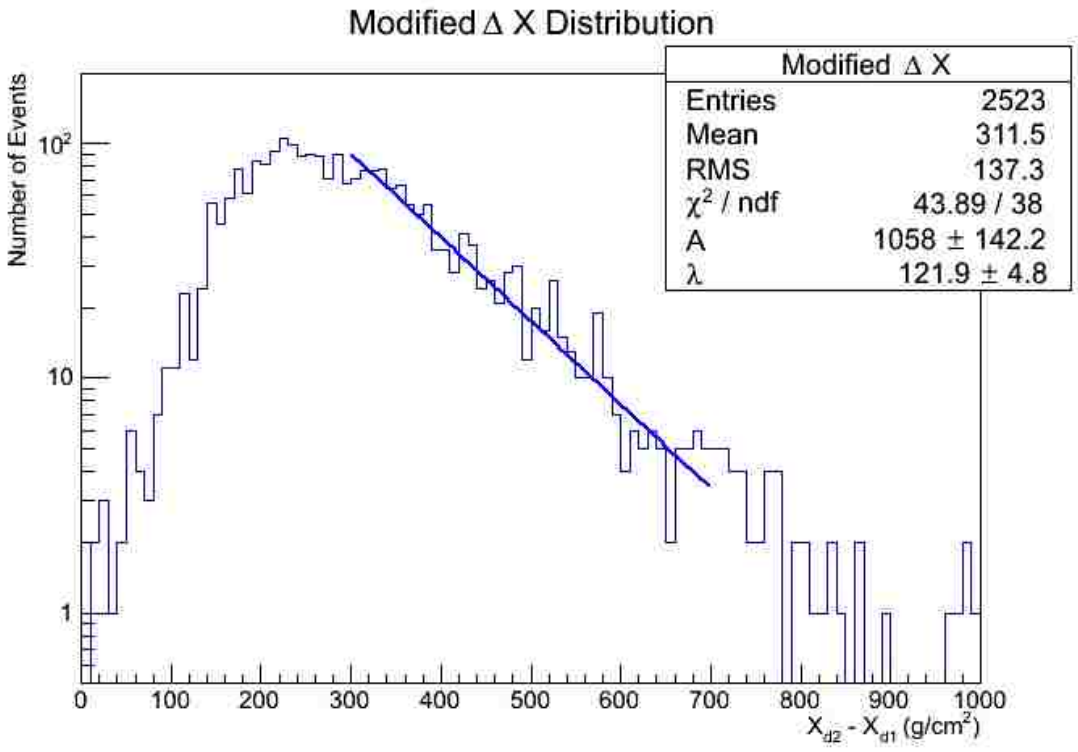

Figure 4.17: Modified ΔX distribution. The blue line represents the exponential fit.

data leading particle physics investigation. A preliminary interaction length for the leading particle is fitted.

We are able to find a few SD "double shells" event candidates that are confirmed by the FD "double bump" shower profiles. It is a good start and more "double shell" event candidates are needed for this study. The separation needed to find the second peak still leaves room for improvement as we try to eliminate artificial bias for forcing the second shower front. Amir Shadkam in our group is investigating the technique to identify FD "double bumps" events. A set of hybrid events that shows leading particle physics characters in both FD and SD would further enhance the credibility of this method finding.

The "double bump" and "double shells" events, if confirmed, can be used for studying the cross sections of hadronic interactions at ultra-high energy. They are also very valuable for the study of exotic physics. The peak finding method described above are also used in Chapter 5 to study muon numbers in a SD station.

5. New Methods for Muon Counting

5.1 Introduction

The primary particle type remains one of the unsolved mysteries in ultra-high energy cosmic rays studies, and muon number is very sensitive in the primary types, as we discussed in Section 2.5.1.2. In other words, heavier primaries, like iron, will produce more muons in air showers than will a proton primary with the same total energy [34]. In 2007, Garrido, et al. reported a method for counting muons with FADC trace jumps [28]. Inspired by that work, we extend the jump method and find that the jumps and our own peak finding methods show good correlation with the muon number in the simulation.

5.2 Muon Signal Characters

A muon produced in an air shower travels almost in a straight line to the ground, while the electromagnetic (EM) component is more dispersed, because of scattering interactions [34]. Therefore, the muons will arrive at the ground earlier and with less time spread. Muons also tend to have much higher energies than EM particles and so will have longer paths and larger signals in a detector. In the SD tank, muons usually have a signal in the order of 1 VEM while the photons and electrons have a signal in the order of 1/200 VEM [112]. In FADC traces, muon signals consequently appear earlier, sharper, bigger and narrower than do EM signals. Figure 4.6 in the Chapter 4 shows an example of an FADC trace with muons and EM signal from a simulated 10 EeV (10^{19} eV) iron primary air shower.

So if you see a sharp rise in a FADC traces in a station that is far away from the shower axis, it is most likely caused by muon signal, which motivates the concept of "jumps". In some cases, multiple muons may come within a small time window of 100 ns (1 time bin =25 ns) and the muon traces will overlap one another. The later one do not show sharp rise in the front since it has a very similar signal size as the previous muon, but will drop at the end.

In order to count that, we came up with the idea of the signal "drop", the reverse concept of the signal jump. Muon signals often appear as a peak in the background of (smaller, but abundant) EM signal components, so the peak signal also provides a possible way of muon counting, as discussed in Chapter 4.

5.3 Garrido's Method

Garrido's work had been focusing on the fitting of the muonic and electromagnetic components. A Jump is defined as the difference between the size of an FADC bin compared to the previous bin [28]. He uses 0.5 VEM for the signal size cut between a muon "jump" and an ordinary fluctuation.

$$\text{Jump}(i) = v(i) = V(i) - V(i-1) \;\; \text{considered if Jump}(i) \geq 0.5\text{VEM} \tag{5.1}$$

where i (from 1 to 768) is the FADC trace bin number.

He looks at the simulations air showers since in simulations the muonic and electromagnetic contributions can be separately quantified. Two distribution functions are introduced to describe the two components,

$$\begin{aligned} \left.\frac{dN}{dv}\right|_{em} &= f_{em}(v) = p_0 \times v^{-\gamma} \\ \left.\frac{dN}{dv}\right|_{\mu} &= f_{\mu}(v) \;\; = \frac{p_1}{1+\exp(\frac{v-p2}{p3})} \end{aligned} \tag{5.2}$$

where p_1, p_2, p_3 are all fitting parameters, v is the jump size and γ has a fixed value of 2.3. The electromagnetic distribution is a power law and the muonic distribution is described by a Fermi-Dirac function. Examples of their fitting to the shower simulations are given in Figure 5.1. The muon and electromagnetic signals are shown separately. From the χ^2/ndf result, we can see the fitting works well.

The disadvantage of this method is that it needs large statistics and it is hard to connect the fitting parameters to the ratio of the muon numbers and electromagnetic numbers. But

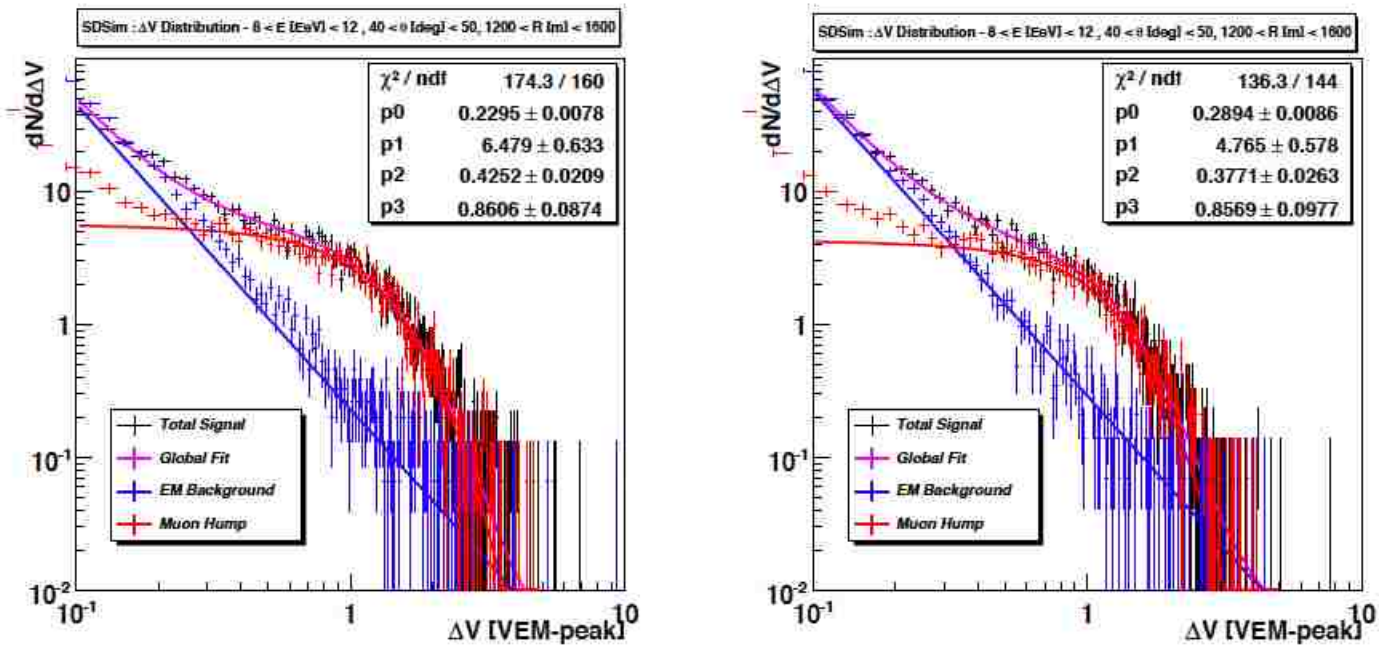

Figure 5.1: FADC trace jump fitting results for 10 EeV proton (left) and iron (right) simulated air shower. Both showers have a zenith angle of 45° and the stations are between 1200m and 1600m from the shower core. The distributions are normalized to the number of stations. From [28].

we can see that the "jumps" do have some physical connections with the muon content. So we tried several other methods to find the muon numbers directly.

5.4 New Methods for Muon Counting

We experimented with several quantities and examined their correlations with the muon number in simulations. The quantities we are looking for in the FADC traces include "Jump", "Drop" and "Peak".

A Jump is still the same definition as in Garrido's method but in our case, we find 0.4 VEM instead of 0.5 VEM is a better signal size cut for our correlation result.

$$Jump(i) = V(i) - V(i-1) \text{ considered if } Jump(i) \geq 0.4\,\text{VEM} \tag{5.3}$$

A Drop is defined as the difference between the size of the bin compared to the following

bin. It has to be larger than 0.4 VEM and not part of an identified Jump. The purpose of this restriction is to avoid double counting the early muons. This is the reverse concept of a Jump in order to include the situations that multiple muons arrive very close in time.

$$Drop(i) = V(i) - V(i+1) \text{ considered if } \begin{cases} Drop(i) \geq 0.4\,\text{VEM} \\ Jump(i) < 0.4\,\text{VEM} \end{cases} \tag{5.4}$$

A Peak is defined similarly as in Section 4.2.1.2. The size of the peak bin needs to be larger than 3 bins before or after it, provided it has a size larger than 0.5 VEM or 30% of the largest bin, whichever is larger.

$$Peak(i) = V(i) \text{ considered if } \begin{cases} V(i) \geq 0.5\,\text{VEM and 30\% of the largest bin} \\ V(i) > V(i+j),\ j = -3, -2, -1, 1, 2, 3 \end{cases} \tag{5.5}$$

Here we require 3 bins instead of 4 bins as in Section 4.2.1.2 because the two peak finding methods are for different purposes. For double shell event identification, we want to ignore the close-by muon peaks and search for a possible second shower front signal group while for muon counting, we want to include all the possible muon signals.

5.5 SD Stations Selection

We study the different muon counting methods using simulated events since in simulations, the muon numbers are given. To maximize our ability to identify muons in FADC traces, one should not look at stations very close to the core, where the EM component overwhelms the muons. Figure 5.2 shows a typical FADC trace from a SD station close to the shower core(482 m in this example). The iron primary showers have large muon numbers (157 in this case) but the muonic signals are still submerged by the EM signal. It is hard to get an accurate muon number count in these cases.

In order to get high quality events for the muon number correlation studies, the following cuts are made on the simulation events and on the SD station selection:

- Energy Cut

  The reconstructed energy range needs to be in the range of $18.0 \leq logE \leq 19.6$, which

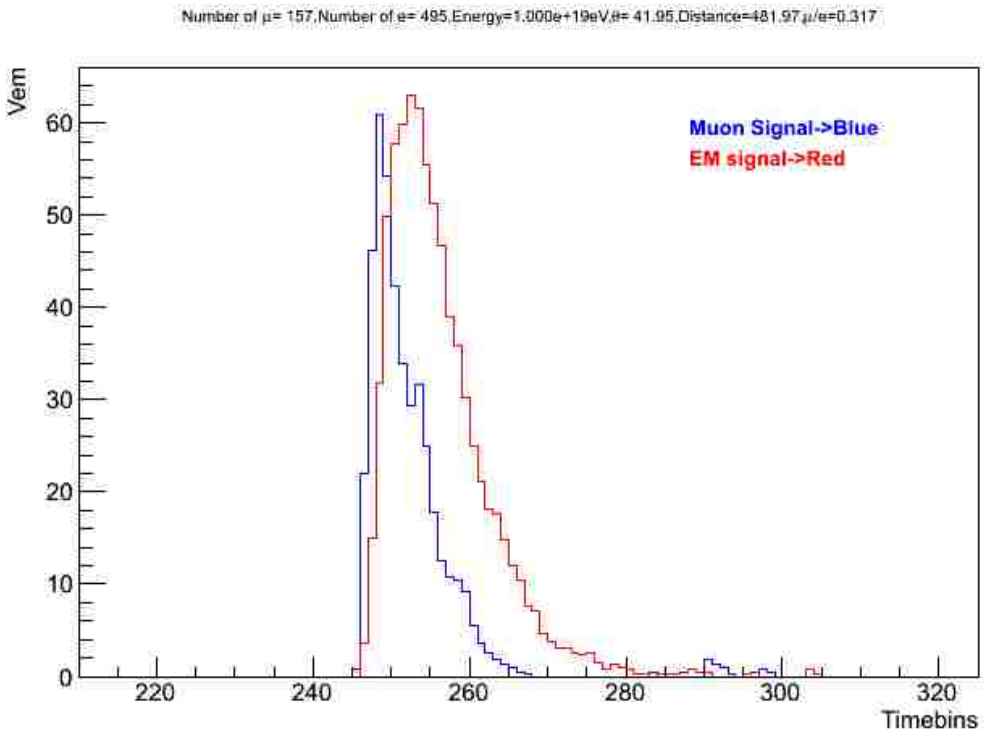

Figure 5.2: FADC trace from a station that is 482 m from the shower axis. The shower is a simulated 10 EeV iron primary air shower. Muon signal is shown in blue and EM signal is marked in red. Even with a large muon number from iron primary, the muon signal is overwhelmed by EM signal.

is same range for most PAO data.

- Event Quality Cut

  Every PMT need to have a trace, so we discard stations that have one or two PMTs malfunctioning, to ensure better signal detection quality. The T5 trigger (described in Section 3.2.3) is also required.

- Distance Cut

  The distance from the surface station to the shower axis can not be too close, so we only select stations from 1.2 km to 1.6 km away from shower axis.

- Zenith Angle Cut

  The reconstructed shower axis needs to be nearly vertical. The purpose of this cut is

to ensure the signal sizes are similar at all azimuthal locations around the shower axis. The zenith angle range I use is from 0° to 30°.

- Signal Size Cut

  The maximum peak in the FADC trace needs to be < 5000 VEM. The purpose of this cut is to eliminate the events where the PMTs begin to saturate when recording a large signal. The background noise can be very big and may be mistakenly considered to be a muon signal.

After the events cut, each FADC are searched for "Jumps", "Drops" and "Peaks". Five quantities related to these three types are calculated for each selected station. The five quantities are listed below.

(a) Sum of jumps signal size

(b) Number of jumps-plus-drops

(c) Sum of jumps-plus-drops signal size

(d) Number of peaks

(e) Sum of the peaks signal size

Figure 5.3 shows an example of an FADC trace and the five quantities we used in our correlation studies. The Number of muons of this stations is $N_\mu = 11$ from the simulation information. The five quantities listed above are 7.4, 10, 10.1, 3, 9.1, respectively. It should be noted here that we do not necessarily look for a quantity that is exactly the same as the simulation's muon number, but look instead for a quantity that is proportional to it.

5.6 Results

5.6.1 The Simulation Correlation Results

The methods cannot be expected to identify accurately all muons in each detector. Rather, it will be sufficient if the techniques show good correlations with the actual number of muons.

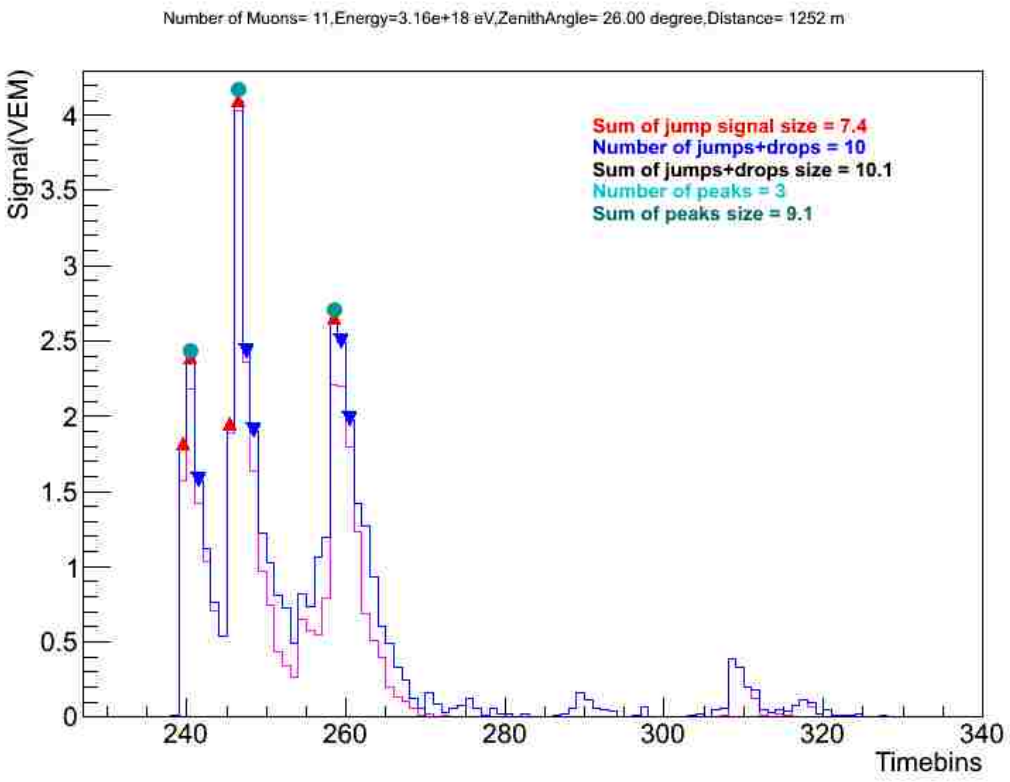

Figure 5.3: Different muon counting methods example. The cyan full circles are the peaks found, the red upward-pointing triangles are the jumps found and the blue downward-pointing triangles are the drops found. The title shows the number of muons that hit the station from the simulation and the five quantities calculated are shown in the upper right corner.

To check the correlations, the official simulation data from Lyon server in France [108] are used. Two hadronic models, QGSjetII [105] and Epos [107] are used and two types of primaries, protons and iron are assumed. We made scatter plots between all the five quantities and the actual number of muons penetrating the detectors in the simulation. The results shown below are the events with an iron primary with an energy of 10^{19} eV using the EPOS hadronic model (see Figure 5.4 through Figure 5.8). A total of 2726 events pass the selection cuts. The dashed red line is a linear least square fit and provide a reference to compare the correlation quality.

As seen from the results, it appears that all the four quantities except Number of peaks (Figure 5.7) correlated linearly. However, one of the four, the sum of jumps-plus-drops signal

size (Figure 5.6), correlate better than the other three quantities based on the uncertainty of the fit results (see Figure 5.9 through Figure 5.13). From now on, I will use this quantity as well as the sum of the peak signal size (Figure 5.8) in the following discussion since these two quantities take the signal size differences into account and provide a cross-check on the result.

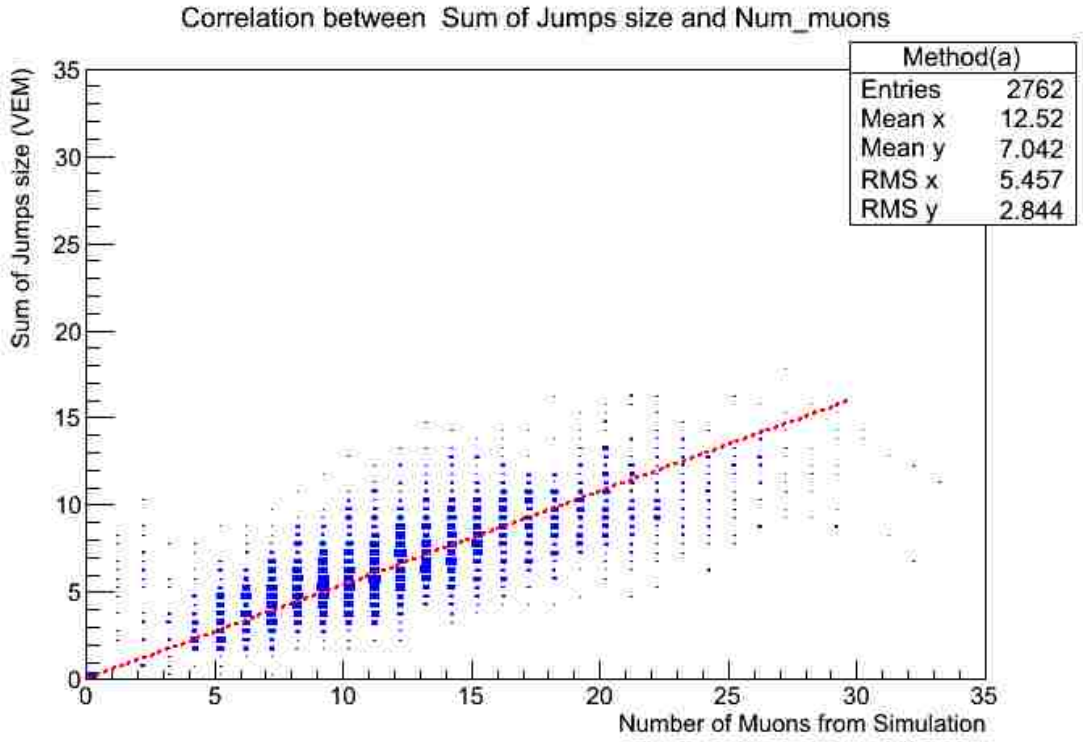

Figure 5.4: Sum of the jump signal size correlation result with true muon number, the dashed red line is a linear least square fit.

5.6.2 Grouping Improves the Correlation

We also find that if we group the similar stations together and sum the quantities, the correlations will be better. This is due to that the fluctuation from station by station can be reduced by increased statistics. In theory, the more stations you put in one group, the better linear fit you can do. In practice, however, we are limited by the size of the simulation database at Lyon server [108]. We tried 5, 10, 20, 50, 100 stations per group and found

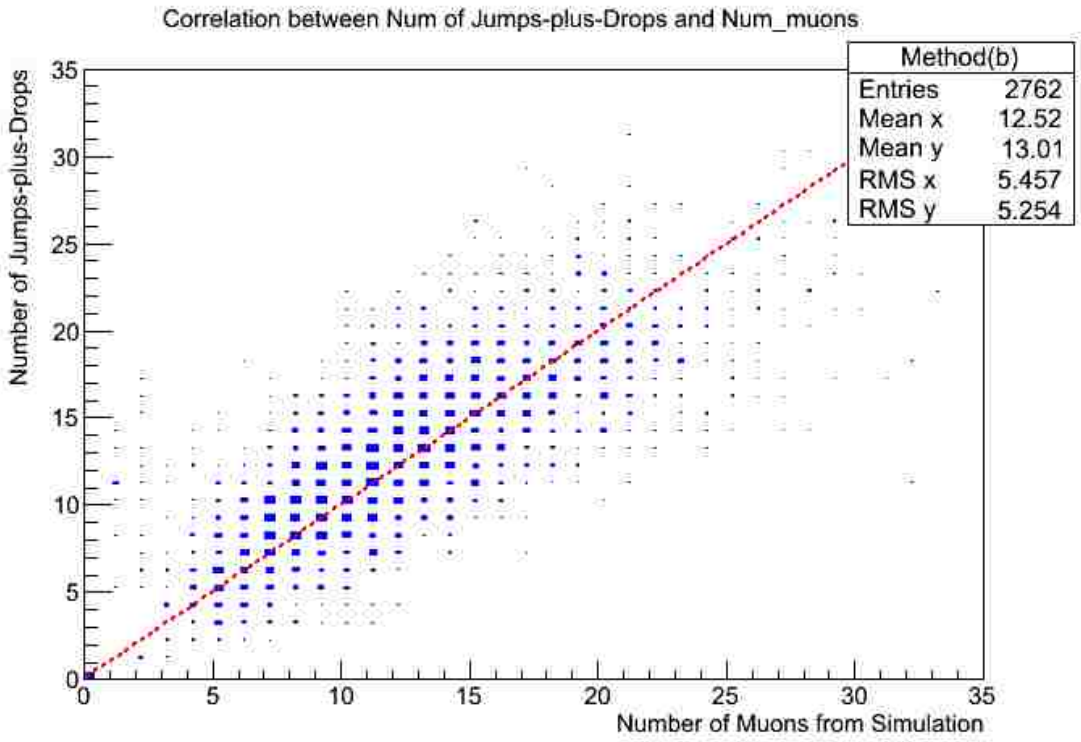

Figure 5.5: Number of jumps-plus-drops correlation result with true muon number, the dashed red line is a linear least square fit.

that 50 stations per group gives the best balance in the sense of eliminating fluctuation and keeping enough statistics. The correlation results of the sum of jumps-plus-drops signal (Figure 5.14) and sum of the peaks signal (Figure 5.15) with the muon numbers are shown below for 50 stations per group.

The slopes for these two linear fits are 0.78 and 0.95 respectively. We use this linear relation to calculate the number of muons from these two quantities. We then compare the calculated muon numbers ($N^{\mu}_{calculated}$) to the true muon numbers obtained from the simulations (N^{μ}_{true}). The results are shown in Figure 5.16 and Figure 5.17 respectively. As can be seen from the results, the calculated muon numbers are within 20 % of the true muon numbers, with the sum of jumps-plus-drops signal method (RMS $\sim$ 0.046) holding a slight edge over the sum of peaks signal method (RMS $\sim$ 0.056).

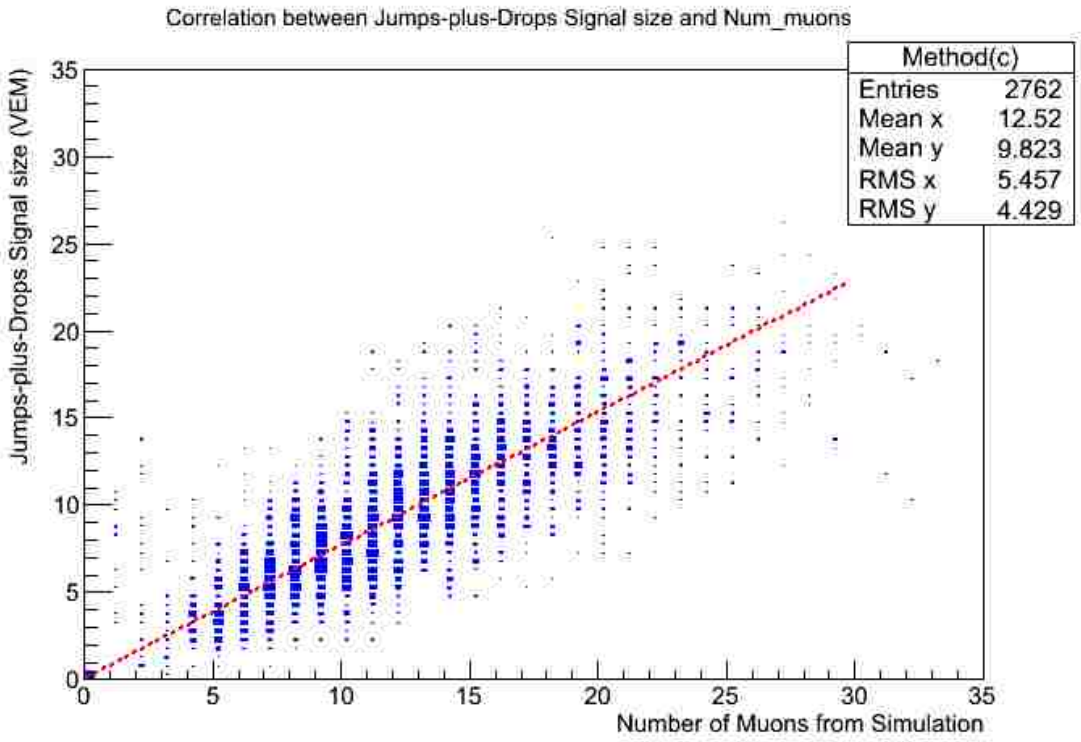

Figure 5.6: Sum of jumps-plus-drops signal size correlation result with true muon number, the dashed red line is a linear least square fit.

5.6.3 Results with the PAO Data

As we can correlate the two quantities rather nicely with the muon number from the simulation, we applied the same methods for the PAO SD data. The PAO SD data used here are from January 2004 to September 2009 and downloaded from Auger Observer [109]. It is reconstructed with the official $\overline{\text{Off}}\underline{\text{line}}$ framework [110] version v2r5p7 and stored in ADST data format [109]. In order to compare the quantities from the PAO SD data and the simulations, one needs to do the same data analysis for both data sets. The steps for the data analysis include:

1. Event selection cuts on both the PAO SD data and the simulation data of QGSjetII and Epos hadronic models.

2. Search for the "Jumps", "Drops" and "Peaks" for the stations and calculate the the

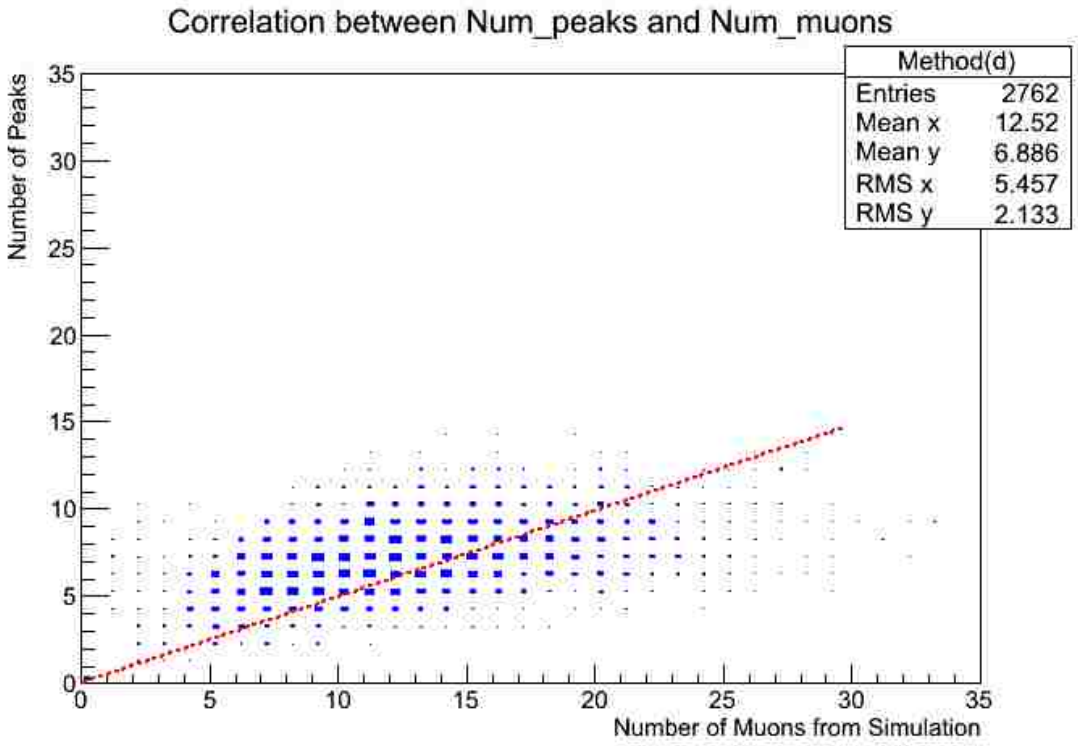

Figure 5.7: Number of peaks correlation result with true muon number, the dashed red line is a linear least square fit.

two quantities discussed in Section 5.6.2.

3. Save the values and store them with the energy information.

4. Separate the stations by the energy information, with 0.1 increase in log(E/eV) of the energy window.

5. Group the stations within the same energy window and calculate the average of the two quantities.

6. Make the plot for these two quantities with regard to the energy for the simulations and PAO data.

Figure 5.18 and Figure 5.19 show the comparison results between the PAO data and simulation. We find that iron primaries with the Epos hadronic model simulation agree

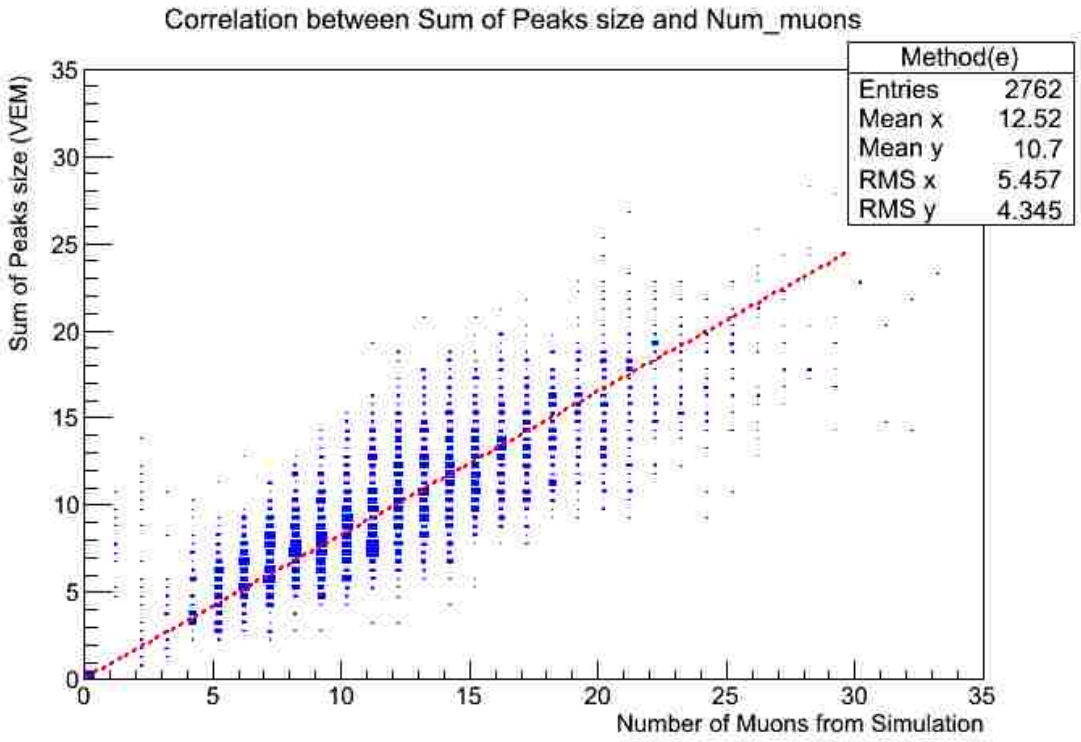

Figure 5.8: Sum of the peaks signal size correlation result with true muon number, the dashed red line is a linear least square fit.

very well with the PAO SD data. This has been seen also in studies of X_{max} [113]. Due to the limitation of the simulation file, the Epos data only have seven energies data points available. Both proton and iron primary shower simulations based on QGSjetII model have the two quantities below the PAO data. However, the QGSjetII model have been previously reported to underestimate the muon content [111]. So it can not be used to draw any simulation conclusions.

5.7 Discussion and Summary

In conclusion, we extend the Garrido's jump method by including ideas of drops and peaks. We find that two quantities, the sum of peaks signal and sum of jumps-plus-drops signal, correlate well with the actual muon number obtained in the simulation events. We find the muon numbers obtained from iron primaries with Epos hadronic model agrees well with the

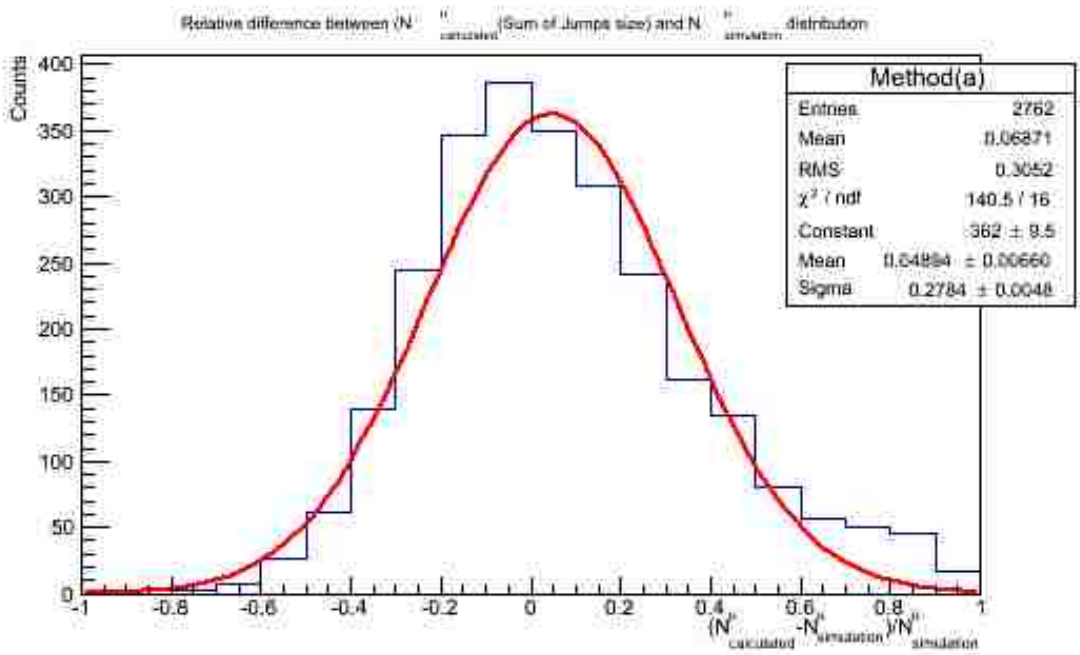

Figure 5.9: Distribution of relative difference between sum of the jump signal size and true muon number, the red line is a gaussian fit.

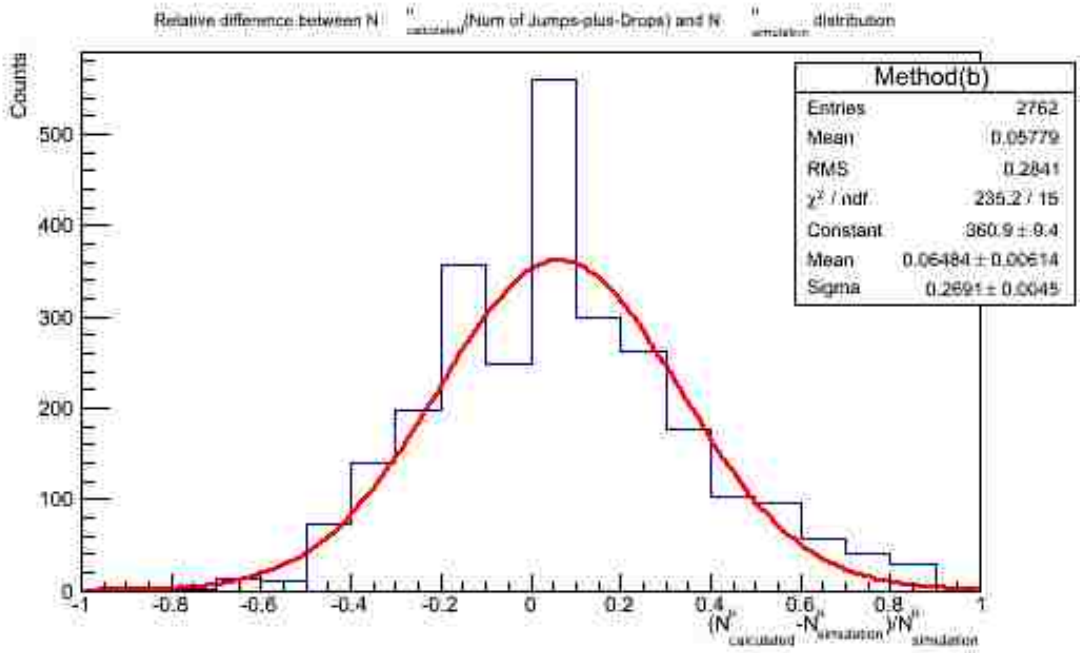

Figure 5.10: Distribution of relative difference between number of jumps-plus-drops and true muon number, the red line is a gaussian fit.

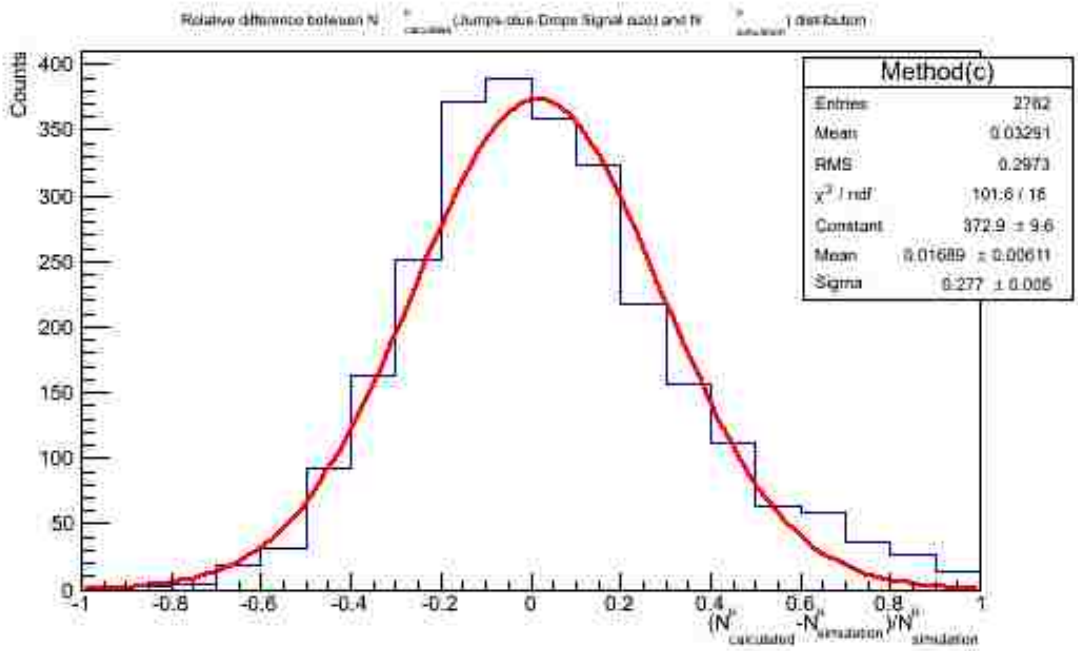

Figure 5.11: Distribution of relative difference between sum of jumps-plus-drops signal size and true muon number, the red line is a gaussian fit.

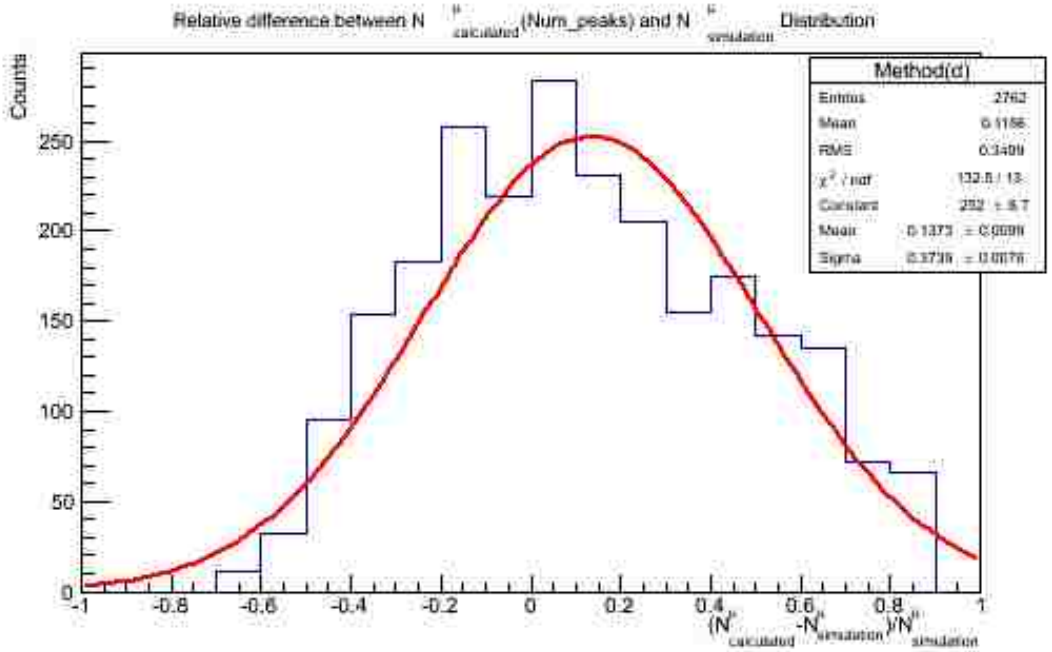

Figure 5.12: Distribution of relative difference between number of peaks correlation and true muon number, the red line is a gaussian fit.

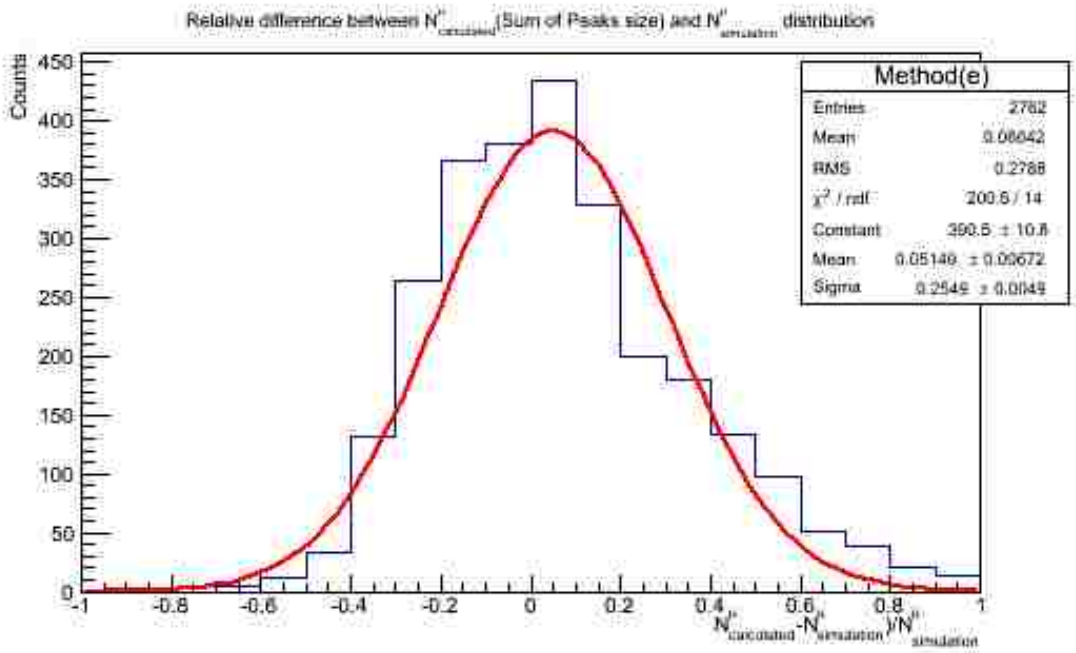

Figure 5.13: Distribution of relative difference between sum of the peaks signal size and true muon number, the red line is a gaussian fit.

PAO SD data while the both the iron and proton primary simulation give a lesser quantity in both of the methods. The QGSjetII model underestimates the muon numbers when compared to PAO data, as we have learned from other methods. More simulations for iron primary with Epos simulation model are needed to better check the results.

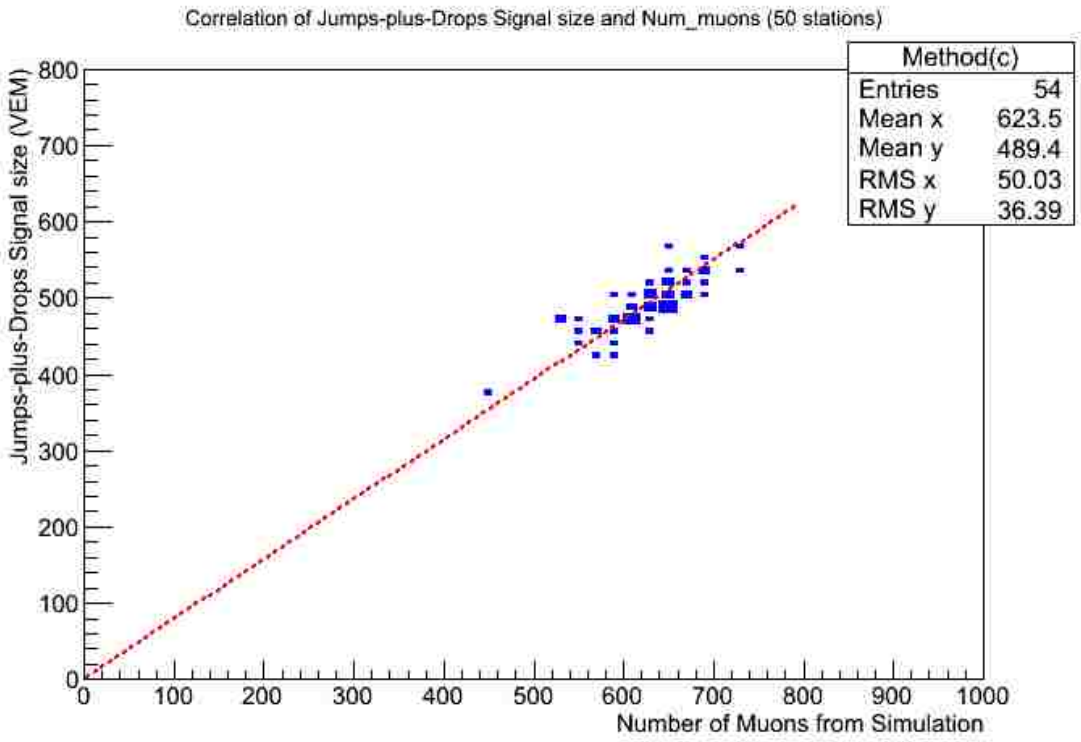

Figure 5.14: The correlation between the sum of jumps-plus-drops signal and total number of muons after grouping 50 stations for one data point, the dashed red line is a linear least square fit.

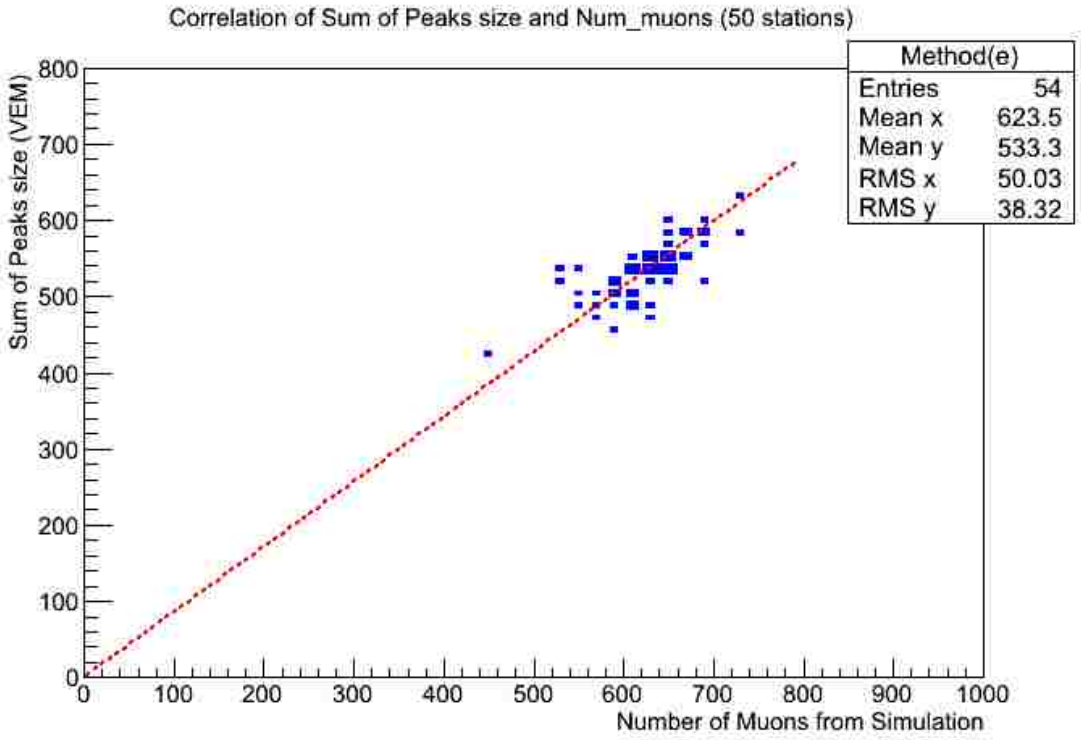

Figure 5.15: The correlation between the sum of peaks signal and total number of muons after grouping 50 stations for one data point, the dashed red line is a linear least square fit.

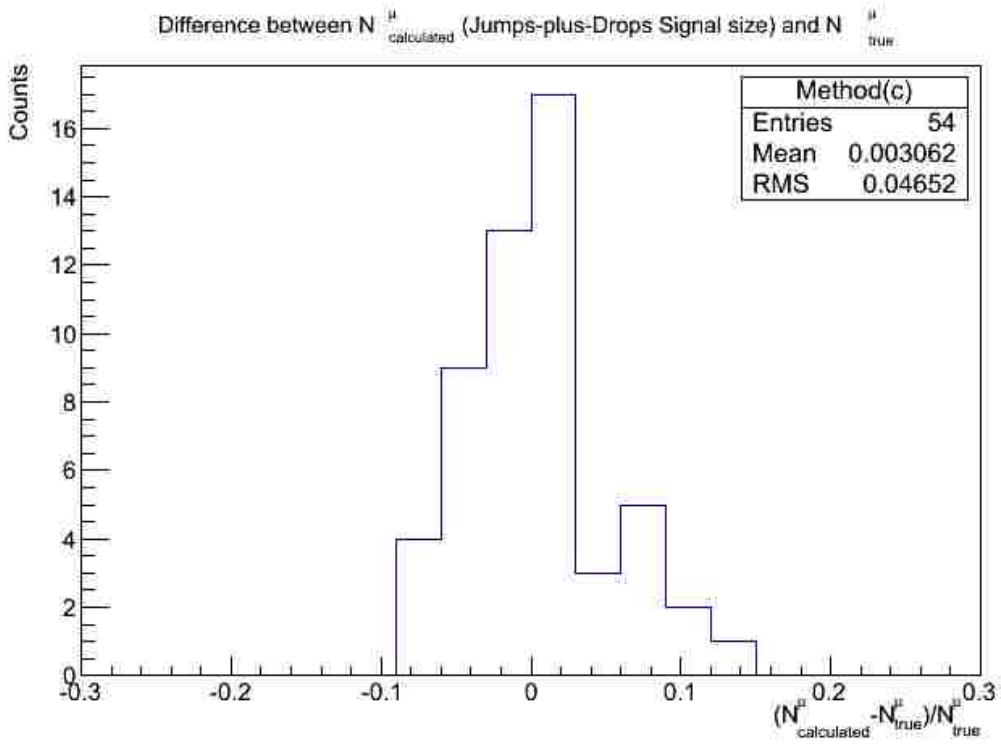

Figure 5.16: Distribution of the relative differences between the calculated muon numbers (sum of jumps-plus-drops signal method) and true muon numbers. RMS of this distribution is ~ 0.046.

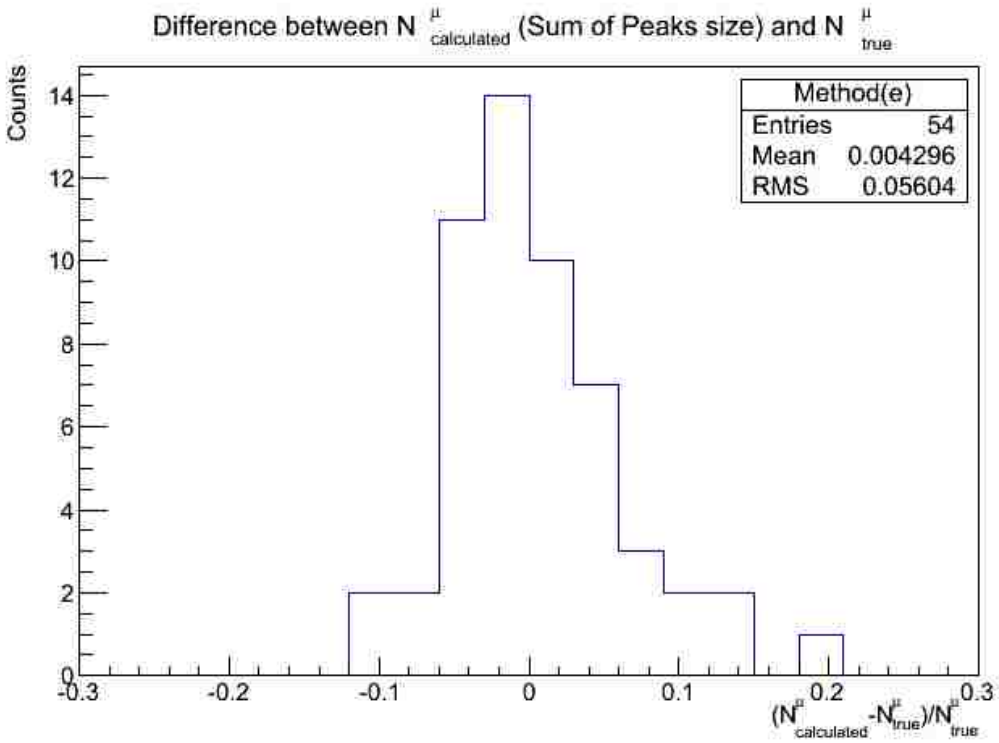

Figure 5.17: Distribution of the relative differences between the calculated muon numbers (sum of peaks signal method) and true muon numbers. RMS of this distribution is ~ 0.056.

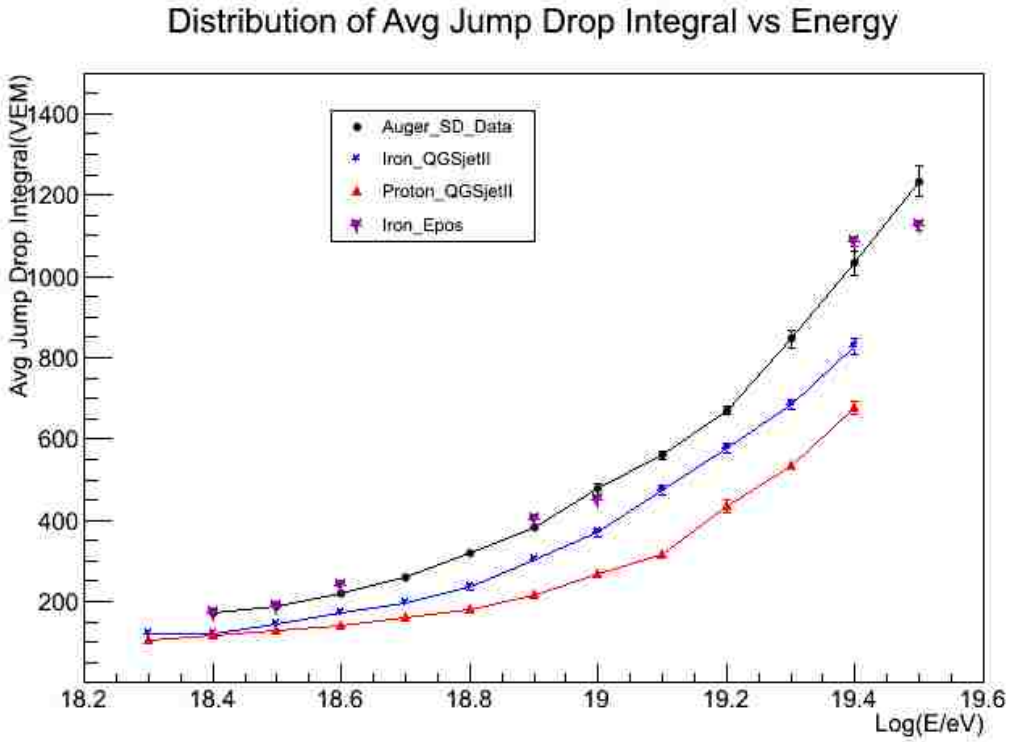

Figure 5.18: Average of the sum of jumps-plus-drops signal for 50 stations within the same energy window vs energy. Each data point is separated with 0.1 increase in log(E/eV). For example, the point at 18.5 is the average of the events with log(E/eV) between 18.5 to 18.6. The purple stars represent simulations of iron primaries with the Epos hadronic model and the PAO SD data are marked in black circles.

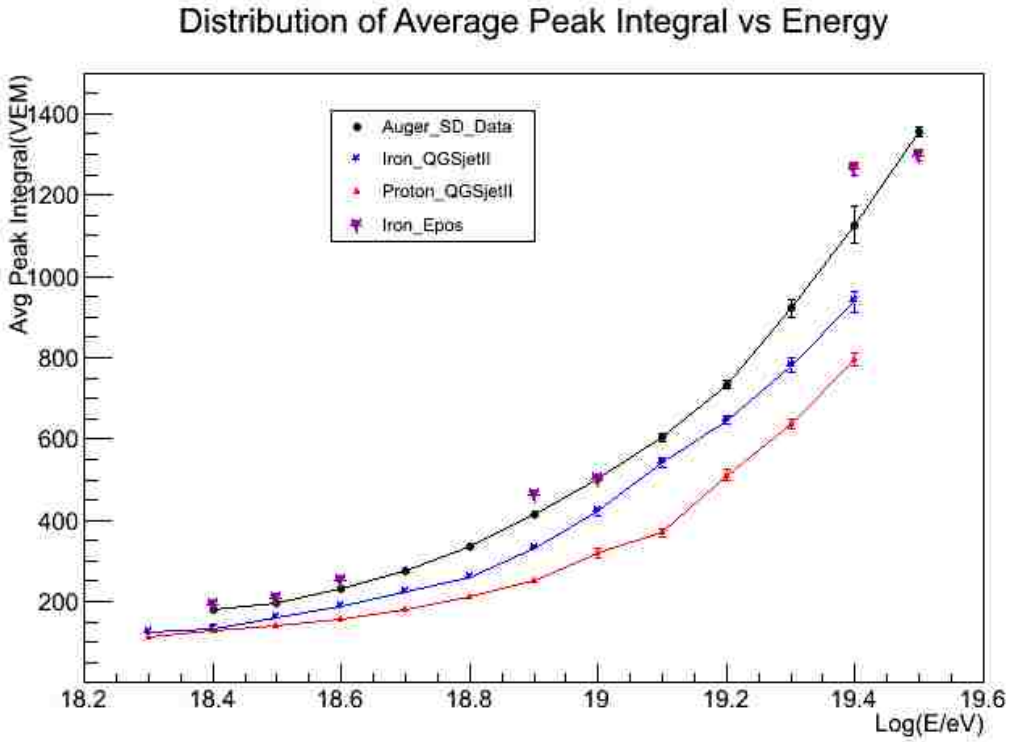

Figure 5.19: Average of the sum of the peak signal for 50 stations within the same energy window vs energy. Each data point is separated with 0.1 increase in log(E/eV). For example, the point at 18.5 is the average of the events with log(E/eV) between 18.5 to 18.6. The purple stars represent simulations of iron primaries with the Epos hadronic model and the PAO SD data are marked in black circles.

6. Summary and Outlook

6.1 Summary

Cosmic rays have been investigated since their discovery one hundred years ago, it has led to the discovery of several elementary particles at the early 20th century. Now ultra high energy cosmic rays (UHECR) have provided a platform for particle physics research beyond the energy that man-made accelerators could possibly achieve in the foreseen future. Yet the origin, acceleration and composition of UHECR are still unknown. Because of their rarity, UHECR can not be directly measured in practice. Extensive Air Showers (EAS) are used to study them but with challenges for the data interpretation. The physics of EAS is studied and there exist two components of air showers, hadronic and electromagnetic EAS, each with different properties. Scientists have developed two techniques for EAS study, ground based surface array detection and air fluorescence detection. Air fluorescence detection observes the longitudinal shower development in the air while the surface array detects the foot prints of the EAS on the ground.

The two complementary methods are successfully implemented in Pierre Auger Observatory (PAO), the largest cosmic ray observatory in the world. The data collected in one year at PAO roughly equals the exposure of all the previous cosmic ray experiments combined. The hybrid design provides crosschecks and improves event reconstruction accuracy of the energy and direction of UHECR. The trigger and data acquisition system of both the FD and the SD cut down the background noise and ensures the data collection efficiency. The atmosphere monitoring facilities provide information about the atmosphere during the FD operation and help FD reconstruction. Recently, PAO has set limits on the photon and neutrino fractions in UHECR. It has observed the "ankle" of the energy spectrum and confirmed the GZK suppression above 4×10^{19} eV. It has studied the composition by using depth of shower maximum information (X_{max}), suggesting that the composition gets heavier in higher

energies. It also observed the correlation between the arrival direction of UHECR and extra galactic sources. Proton-air cross section beyond 10^{18} eV is calculated the first time.

A "Peak Finding Method" is used for the study of the leading particle physics at the highest energies. The peak locations in the FADC trace reveal the timing information of the possible shower shells, which is related to the first interactions of the primary shower and a major sub-shower. The correlation between the SD radius of curvature and FD shower profile start point is confirmed.

Garrido first used the idea of FDAC "Jumps". We extend his "Jumps" method and added the concepts of "Drops" and "Peaks" for muon number calculation. We find two quantities, the sum of the jumps-plus-drops signal and the sum of the peak signal, show good correlations with the muon number. We also find grouping 50 stations together improve the correlation and still keeps enough statistics for the comparison between PAO SD data and the simulation. In the comparison, we see that the Epos iron primary simulations agree well with the PAO SD data, however, the statistics are low to draw an conclusion. The underestimation of muons in QGSjetII hadronic models is also observed.

6.2 Outlook

The methods of jumps, drops and peaks show good potential for leading particle physics study and muon number identification, which is sensitive in cosmic ray composition. The underestimation of muons of the hadronic models has been confirmed by multiple methods and an improvement of models is on the way. More simulation files accordingly would also help for the comparison with the PAO SD data and UHECR composition research.

Bibliography

[1] L. Evans, "The Large Hadron Collider," Ann. Rev. Nucl. Part. Sci. **61**, 435 (2011).

[2] T. Stanev, "Ultrahigh Energy Cosmic Rays: Review of the Current Situation," arXiv:1210.0927 [astro-ph.HE].

[3] V. Hess, "Uber Beobachtungen der durchdringenden Strahlung bei sieben Freiballonfahrten," Physik. Zeitschr. **13**, 1084 (1912).

[4] C. Anderson, "Early Work on the Positron and Muon," Am. J. Phys. **29**, 825 (1961).

[5] D. H. Perkins, "The discovery of the pion in Bristol in 1947," In *Varenna 1997, Heavy flavour physics* 1-12

[6] P. Auger, P. Ehrenfest, R. Maze, J. Daudin and A. F. Robley, "Extensive cosmic ray showers," Rev. Mod. Phys. **11**, 288 (1939).

[7] L. G. Porter, J. C. Earnshaw, E. Tielsch-Cassel, J. C. Ahlstrom and K. Greisen, "A space-time detector for cosmic ray showers," Nucl. Instrum. Meth. **87**, 87 (1970).

[8] A. M. Hillas, "The Origin of Ultrahigh-Energy Cosmic Rays," Ann. Rev. Astron. Astrophys. **22**, 425 (1984).

[9] R. J. Protheroe and A. P. Szabo, "High-energy cosmic rays from active galactic nuclei," Phys. Rev. Lett. **69**, 2885 (1992).

[10] A. Letessier-Selvon and T. Stanev, "Ultrahigh Energy Cosmic Rays," Rev. Mod. Phys. **83**, 907 (2011) [arXiv:1103.0031 [astro-ph.HE]].

[11] E. Waxman, "Cosmological gamma-ray bursts and the highest energy cosmic rays," Phys. Rev. Lett. **75**, 386 (1995) [astro-ph/9505082].

[12] M. Vietri, "Coronal gamma-ray bursts as the sources of ultrahigh-energy cosmic rays?," astro-ph/9510148.

[13] M. Milgrom and V. Usov, "Possible association of ultrahigh-energy cosmic ray events with strong gamma-ray bursts," Astrophys. J. **449**, L37 (1995) [astro-ph/9505009].

[14] K. Dolag, D. Grasso, V. Springel and I. Tkachev, "Mapping deflections of extragalactic ultra high energy cosmic rays in magnetohydrodynamic simulations of the local universe," Nucl. Phys. Proc. Suppl. **136**, 234 (2004).

[15] A. Dar and A. De Rujula, "The Magnetic field in galaxies, galaxy clusters, and the intergalactic space," Phys. Rev. D **72**, 123002 (2005) [astro-ph/0504480].

[16] R. Beck, "Galactic and Extragalactic Magnetic Fields," AIP Conf. Proc. **1085**, 83 (2009) [arXiv:0810.2923 [astro-ph]].

[17] L. Anchordoqui, T. C. Paul, S. Reucroft and J. Swain, "Ultrahigh-energy cosmic rays: The State of the art before the Auger Observatory," Int. J. Mod. Phys. A **18**, 2229 (2003) [hep-ph/0206072].

[18] P. Meszaros, "Theories of gamma-ray bursts," Ann. Rev. Astron. Astrophys. **40**, 137 (2002) [astro-ph/0111170].

[19] G. J. Fishman and C. A. Meegan, "Gamma-ray bursts," Ann. Rev. Astron. Astrophys. **33**, 415 (1995).

[20] K. Greisen, "End to the cosmic ray spectrum?," Phys. Rev. Lett. **16**, 748 (1966).

[21] G. T. Zatsepin and V. A. Kuzmin, "Upper limit of the spectrum of cosmic rays," JETP Lett. **4**, 78 (1966) [Pisma Zh. Eksp. Teor. Fiz. **4**, 114 (1966)].

[22] D. RBergman and J. W. Belz, "Cosmic Rays: The Second Knee and Beyond," J. Phys. G **34**, R359 (2007) [arXiv:0704.3721 [astro-ph]].

[23] J. Abraham *et al.* [Pierre Auger Collaboration], "Trigger and aperture of the surface detector array of the Pierre Auger Observatory," Nucl. Instrum. Meth. A **613**, 29 (2010) [arXiv:1111.6764 [astro-ph.IM]].

[24] J. Abraham *et al.* [Pierre Auger Collaboration], "The Fluorescence Detector of the Pierre Auger Observatory," Nucl. Instrum. Meth. A **620**, 227 (2010) [arXiv:0907.4282 [astro-ph.IM]].

[25] T. Gaisser,A. Hillas, "Reliability of the Method of Constant Intensity Cuts for Reconstructing the Average Development of Vertical Showers.," Proc. 15th Int. Cosmic. Ray Conf. Plovdiv, **8**, 353 (1977)

[26] G. Matthiae, "Observations of ultra high energy cosmic rays," J. Phys. Conf. Ser. **203**, 012016 (2010).

[27] J. W. Cronin, "Cosmic rays: The most energetic particles in the universe," Rev. Mod. Phys. **71**, S165 (1999).

[28] X. Garrido,et al. "Measurement of the number of muons in Auger tanks by the FADC jump counting method," Pierre Auger Collaboration Technical Note, GAP 2007-060.

[29] M. Ave, J. A. Hinton, R. A. Vazquez, A. A. Watson and E. Zas, "Constraints on the ultrahigh-energy photon flux using inclined showers from the Haverah Park array," Phys. Rev. D **65**, 063007 (2002) [astro-ph/0110613].

[30] J. Linsley, "Evidence for a primary cosmic-ray particle with energy 10^{20} eV," Phys. Rev. Lett. **10**, 146 (1963).

[31] R. M. Baltrusaitis, R. Cady, G. L. Cassiday, R. Cooper, J. W. Elbert, P. R. Gerhardy, S. Ko and E. C. Loh *et al.*, "The Utah Fly's Eye Detector," Nucl. Instrum. Meth. A **240**, 410 (1985).

[32] N. Chiba, K. Hashimoto, N. Hayashida, K. Honda, M. Honda, N. Inoue, F. Kakimoto and K. Kamata *et al.*, "Akeno giant air shower array (AGASA) covering 100 km^2 area," Nucl. Instrum. Meth. A **311**, 338 (1992).

[33] W. Heitler, "The Quantum Theory of Radiation,third ed." Oxford University Press, London (1954) 386 p (Section 38)

[34] J. Matthews, "A Heitler model of extensive air showers," Astropart. Phys. **22**, 387 (2005).

[35] W-Y. P. Hwang and B. -Q. Ma, "Neutrons and antiprotons in ultrahigh energy cosmic rays," Eur. Phys. J. A **25**, 467 (2005) [astro-ph/0509118].

[36] A. M. Hillas, "The Sensitivity Of Cherenkov Radiation Pulses To The Longitudinal Development Of Cosmic Ray Showers," J. Phys. G G **8**, 1475 (1982).

[37] J. Abraham *et al.* [Pierre Auger Collaboration], "Measurement of the Depth of Maximum of Extensive Air Showers above 10^{18} eV," Phys. Rev. Lett. **104**, 091101 (2010) [arXiv:1002.0699 [astro-ph.HE]].

[38] H. E. Bergeson, G. L. Cassiday, T. -W. Chiu, D. A. Cooper, J. W. Elbert, E. C. Loh, D. Steck and W. J. West *et al.*, "Measurement of Light Emission from Remote Cosmic Ray Air Showers," Phys. Rev. Lett. **39**, 847 (1977).

[39] D. J. Bird *et al.* [HIRES Collaboration], "The Cosmic ray energy spectrum observed by the Fly's Eye," Astrophys. J. **424**, 491 (1994).

[40] M. Teshima, G. M. Dion, N. Hayashida, K. Hibino, T. Kifune, M. Nagano, S. Yoshida and Y. Matsubara *et al.*, "Telescope array for advanced studies of cosmic rays at the highest and TeV energies," Nucl. Phys. Proc. Suppl. **28**, 169 (1992).

[41] J. W. Cronin, S. P. Swordy and T. K. Gaisser, "Cosmic rays at the energy frontier," Sci. Am. **276**, 32 (1997).

[42] A. A. Penzias and R. W. Wilson, "A Measurement of excess antenna temperature at 4080-Mc/s," Astrophys. J. **142**, 419 (1965).

[43] E. Fermi, "On the Origin of the Cosmic Radiation," Phys. Rev. **75**, 1169 (1949).

[44] R. D. Blandford, "Acceleration of ultrahigh-energy cosmic rays," Phys. Scripta T **85**, 191 (2000) [astro-ph/9906026].

[45] R. J. Protheroe, "Acceleration and interaction of ultrahigh-energy cosmic rays," In *DuVernois, M.A. (ed.): Topics in cosmic-ray astrophysics* 259-297 [astro-ph/9812055].

[46] W. I. Axford,E. Lear,G. Skadron, "The acceleration of cosmic rays by shock waves," Proc. 15th Int. Cosmic Ray Conf. Plovdiv, Bulgaria, **11**, 132 (1977)

[47] G. F. Krymsky, "The acceleration of cosmic rays by shock waves," Dokl. Akad. Nauk. SSSR, **243**, 1306 (1977)

[48] A. R. Bell, "The Acceleration of cosmic rays in shock fronts. II," Mon. Not. Roy. Astron. Soc. **182**, 443 (1978).

[49] R. D. Blandford and J. P. Ostriker, "Particle Acceleration by Astrophysical Shocks," Astrophys. J. **221**, L29 (1978).

[50] A. M. Taylor, I. Vovk and A. Neronov, "Extragalactic magnetic fields constraints from simultaneous GeV-TeV observations of blazars," Astron. Astrophys. **529**, A144 (2011) [arXiv:1101.0932 [astro-ph.HE]].

[51] C. Indrani and A. A. Deshpande, "The large scale structure of the Galactic magnetic field," New Astronomy **33**, 4 (1999).

[52] J. P. Vallee, "Magnetic fields in the galactic Universe, as observed in supershells, galaxies, intergalactic and cosmic realms," New Astron. Rev. **55**, 91 (2011).

[53] D. Harari, S. Mollerach and E. Roulet, "The Toes of the ultrahigh-energy cosmic ray spectrum," JHEP **9908**, 022 (1999) [astro-ph/9906309].

[54] J. Beringer *et al.* [Particle Data Group Collaboration], "Review of Particle Physics (RPP)," Phys. Rev. D **86**, 010001 (2012).

[55] P. Bhattacharjee and G. Sigl, "Origin and propagation of extremely high-energy cosmic rays," Phys. Rept. **327**, 109 (2000) [astro-ph/9811011].

[56] X. Bertou, M. Boratav and A. Letessier-Selvon, "Physics of extremely high-energy cosmic rays," Int. J. Mod. Phys. A **15**, 2181 (2000) [astro-ph/0001516].

[57] T. Stanev, "High energy cosmic rays," Chichester, UK: Praxis-Publ. (2004) 319 p

[58] M. V. S. Rao and B. V. Sreekantan, "Extensive air showers," Singapore, Singapore: World Scientific (1998) 337 p

[59] M. Nagano and A. A. Watson, "Observations and implications of the ultrahigh-energy cosmic rays," Rev. Mod. Phys. **72**, 689 (2000).

[60] K. Greisen "The Lateral and the Angular Structure Functions of Electron Showers," Prog. in Cosmic Ray Phys. Intersci. Publ. Inc., New York **3**(1956) 1 p

[61] K. Kamata and J. Nishimura, "The Lateral and the Angular Structure Functions of Electron Showers," Prog. of Theor. Phys. Suppl. **93**,(1958).

[62] J. Linsley, L. Scarsi and B. Rossi, "Extremely energetic cosmic-ray event," Phys. Rev. Lett. **6**, 485 (1961).

[63] M. M. Winn, J. Ulrichs, L. S. Peak, C. B. A. Mccusker and L. Horton, "The Arrival Directions Of Cosmic Rays Above 10^{17} ev," J. Phys. G G **12**, 675 (1986).

[64] S. N. Vernov, T. A. Egorov, N. N. Efimov, V. A. Kolosov, V. D. Koryakin, D. D. Krasilnikov, A. I. Kuzmin and V. P. Kulakovskaya *et al.*, "Preliminary results on extensive air shower recordings in a complex array at yakutsk," Izv. Akad. Nauk Ser. Fiz. **10**, 2098 (1971).

[65] T. Abu-Zayyad, M. Al-Seady, K. Belov, G. Chen, H. Y. Dai, M. A. Huang, C. C. H. Jui and D. B. Kieda *et al.*, "The prototype high-resolution Fly's Eye cosmic ray detector," Nucl. Instrum. Meth. A **450**, 253 (2000).

[66] H. Kawai, S. Yoshida, H. Yoshii, K. Tanaka, F. Cohen, M. Fukushima, N. Hayashida and K. Hiyama *et al.*, "Telescope array experiment," Nucl. Phys. Proc. Suppl. **175-176**, 221 (2008).

[67] M. T. Dova [Pierre Auger Collaboration], "The Pierre Auger Observatory," Nucl. Phys. Proc. Suppl. **122**, 170 (2003).

[68] A. M. Hillas, Acta Phys. Acad. Sci. Hung. **29**(Suppl. 3), 355 (1970).

[69] P. Sokolsky, P. Sommers and B. R. Dawson, "Extremely high-energy cosmic rays," Phys. Rept. **217**, 225 (1992).

[70] J. Abraham *et al.* [Pierre Auger Collaboration], "Properties and performance of the prototype instrument for the Pierre Auger Observatory," Nucl. Instrum. Meth. A **523**, 50 (2004).

[71] I. Allekotte *et al.* [Pierre Auger Collaboration], "The Surface Detector System of the Pierre Auger Observatory," Nucl. Instrum. Meth. A **586**, 409 (2008) [arXiv:0712.2832 [astro-ph]].

[72] A. Creusot [Pierre Auger Collaboration], "Latest results of the Pierre Auger Observatory," Nucl. Instrum. Meth. A **662**, S106 (2012).

[73] J. Abraham *et al.* [Pierre Auger Collaboration], "Observation of the suppression of the flux of cosmic rays above 4×10^{19}eV," Phys. Rev. Lett. **101**, 061101 (2008) [arXiv:0806.4302 [astro-ph]].

[74] D. Veberic and M. Roth. "SD Reconstruction; Offline Reference Manual," Pierre Auger Collaboration Technical Note, GAP 2005-035.

[75] M. Roth [Pierre Auger Collaboration], "Measurement of the UHECR energy spectrum using data from the Surface Detector of the Pierre Auger Observatory," [arXiv:0706.2096 [astro-ph]].

[76] V. Scherini [Pierre Auger Collaboration], " Performance of the Pierre Auger Fluorescence Detector at the Highest Energies," Proc. 20th Euro. Cosmic Ray Symp., Lisbon, Portugal, (2006).

[77] M. D. Roberts [Pierre Auger Collaboration], "Calibration of the Pierre Auger fluorescence detector," Proc. 28th Int. Cosmic Ray Conf. Tsukuba, Japan, **11**, 132 (2003), [astro-ph/0308410].

[78] H. M. J. Barbosa, F. Catalani, J. A. Chinellato and C. Dobrigkeit, "Determination of the calorimetric energy in extensive air showers," Astropart. Phys. **22**, 159 (2004) [astro-ph/0310234].

[79] L. Wiencke [Pierre Auger Collaborations], "Extracting first science measurements from the southern detector of the Pierre Auger observatory," Nucl. Instrum. Meth. A **572**, 508 (2007) [astro-ph/0607449].

[80] P. Abreu *et al.* [Pierre Auger Collaboration], "The Rapid Atmospheric Monitoring System of the Pierre Auger Observatory," JINST **7**, P09001 (2012) [arXiv:1208.1675 [astro-ph.HE]].

[81] J. Abraham *et al.* [Pierre Auger Collaboration], "Calibration and Monitoring of the Pierre Auger Observatory," [arXiv:0906.2358 [astro-ph.IM]].

[82] B. Fick *et al.* [Pierre Auger Collaboration], "The Central laser facility at the Pierre Auger Observatory," JINST **1**, P11003 (2006) [astro-ph/0507334].

[83] S. Y. BenZvi, R. Cester, M. Chiosso, B. M. Connolly, A. Filipcic, B. Garcia, A. Grillo and F. Guarino *et al.*, "The Lidar System of the Pierre Auger Observatory," Nucl. Instrum. Meth. A **574**, 171 (2007) [astro-ph/0609063].

[84] S. Y. BenZvi, B. M. Connolly, J. A. J. Matthews, M. Prouza, E. F. Visbal and S. Westerhoff, "Measurement of the Aerosol Phase Function at the Pierre Auger Observatory," Astropart. Phys. **28**, 312 (2007) [arXiv:0704.0303 [astro-ph]].

[85] K. Louedec *et al.* [Pierre Auger Collaboration], "Atmospheric aerosols at the Pierre Auger Observatory and environmental implications," Eur. Phys. J. Plus **127**, 97 (2012) [arXiv:1208.6275 [astro-ph.IM]].

[86] R. Cester *et al.* [Pierre Auger Collaboration], "Atmospheric aerosol monitoring at the Pierre Auger Observatory," FERMILAB-CONF-05-293-E-TD,(2005).

[87] S. BenZvi *et al.* [Pierre Auger Collaboration], "New method for atmospheric calibration at the Pierre Auger Observatory using FRAM, a robotic astronomical telescope," [arXiv:0706.1710 [astro-ph]].

[88] J. Bluemer [Pierre Auger Collaboration], "The Pierre Auger Observatory: Results on Ultra-High Energy Cosmic Rays," [arXiv:0807.4871 [astro-ph]].

[89] J. Abraham *et al.* [Pierre Auger Collaboration], "Upper limit on the cosmic-ray photon flux above 10^{19} eV using the surface detector of the Pierre Auger Observatory," Astropart. Phys. **29**, 243 (2008) [arXiv:0712.1147 [astro-ph]].

[90] J. Abraham *et al.* [Pierre Auger Collaboration], "Upper limit on the cosmic-ray photon fraction at EeV energies from the Pierre Auger Observatory," Astropart. Phys. **31**, 399 (2009) [arXiv:0903.1127 [astro-ph.HE]].

[91] J. Abraham *et al.* [Pierre Auger Collaboration], "Upper limit on the diffuse flux of UHE tau neutrinos from the Pierre Auger Observatory," Phys. Rev. Lett. **100**, 211101 (2008) [arXiv:0712.1909 [astro-ph]].

[92] P. Abreu *et al.* [Pierre Auger Collaboratio Collaboration], "Search for point-like sources of ultra-high energy neutrinos at the Pierre Auger Observatory and improved limit on the diffuse flux of tau neutrinos," Astrophys. J. **755**, L4 (2012).

[93] J. Abraham *et al.* [Pierre Auger Collaboration], "Measurement of the energy spectrum of cosmic rays above 10^{18} eV using the Pierre Auger Observatory," Phys. Lett. B **685**, 239 (2010) [arXiv:1002.1975 [astro-ph.HE]].

[94] J. Abraham *et al.* [Pierre Auger Collaboration], "Measurement of the Depth of Maximum of Extensive Air Showers above 10^{18} eV," Phys. Rev. Lett. **104**, 091101 (2010) [arXiv:1002.0699 [astro-ph.HE]].

[95] J. Abraham *et al.* [Pierre Auger Collaboration], "Correlation of the highest energy cosmic rays with nearby extragalactic objects," Science **318**, 938 (2007) [arXiv:0711.2256 [astro-ph]].

[96] E. Roulet, "Latest results from the Pierre Auger Observatory," PoS HRMS **2010**, 034 (2010) [arXiv:1101.1825 [astro-ph.HE]].

[97] M. -P. Veron-Cetty and P. Veron, "A catalogue of quasars and active nuclei: 12th edition," Astron. Astrophys. **455**, 773 (2006).

[98] J. Abraham *et al.* [Pierre Auger Collaboration], "Correlation of the highest-energy cosmic rays with the positions of nearby active galactic nuclei," Astropart. Phys. **29**, 188 (2008) [Erratum-ibid. **30**, 45 (2008)] [arXiv:0712.2843 [astro-ph]].

[99] J. Abraham *et al.* [Pierre Auger Collaboration], "Astrophysical Sources of Cosmic Rays and Related Measurements with the Pierre Auger Observatory," Proc. 30th Int. Cosmic. Ray Conf. Lodz, Poland,(2009) [arXiv:0906.2347 [astro-ph.HE]].

[100] R. W. Ellsworth, T. K. Gaisser, T. Stanev and G. B. Yodh, "Ultrahigh-energy Cross-section From Study Of Longitudinal Development Of Air Showers," Phys. Rev. D **26**, 336 (1982).

[101] R. M. Baltrusaitis, G. L. Cassiday, J. W. Elbert, P. R. Gerhardy, S. Ko, E. C. Loh, Y. Mizumoto and P. Sokolsky *et al.*, "Total Proton Proton Cross-Section at $\sqrt{s} = 30$ TeV," Phys. Rev. Lett. **52**, 1380 (1984).

[102] P. Abreu *et al.* [Pierre Auger Collaboration], "Measurement of the proton-air cross-section at $\sqrt{s} = 57$ TeV with the Pierre Auger Observatory," Phys. Rev. Lett. **109**, 062002 (2012) [arXiv:1208.1520 [hep-ex]].

[103] P. Abreu *et al.* [Pierre Auger Collaboration], "The Pierre Auger Observatory II: Studies of Cosmic Ray Composition and Hadronic Interaction models," Proc. 32nd Int. Cosmic. Ray Conf. Beijing, China,(2011) [arXiv:1107.4804 [astro-ph.HE]].

[104] N. N. Kalmykov and S. S. Ostapchenko, "The Nucleus-nucleus interaction, nuclear fragmentation, and fluctuations of extensive air showers," Phys. Atom. Nucl. **56**, 346 (1993) [Yad. Fiz. **56N3**, 105 (1993)].

[105] S. Ostapchenko, Nucl. Phys. Proc. Suppl. **151**, 143 (2006) [hep-ph/0412332].

[106] E. -J. Ahn, R. Engel, T. K. Gaisser, P. Lipari and T. Stanev, "Cosmic ray interaction event generator SIBYLL 2.1," Phys. Rev. D **80**, 094003 (2009) [arXiv:0906.4113 [hep-ph]].

[107] K. Werner, F. -M. Liu and T. Pierog, "Parton ladder splitting and the rapidity dependence of transverse momentum spectra in deuteron-gold collisions at RHIC," Phys. Rev. C **74**, 044902 (2006) [hep-ph/0506232].

[108] The official PAO simulation database. http://auger.in2p3.fr/DPA/index.html

[109] The Auger Observer database. http://http://augerobserver.fzk.de

[110] S. Argiro, S. L. C. Barroso, J. Gonzalez, L. Nellen, T. C. Paul, T. A. Porter, L. Prado, Jr. and M. Roth *et al.*, "The Offline Software Framework of the Pierre Auger Observatory," Nucl. Instrum. Meth. A **580**, 1485 (2007) [arXiv:0707.1652 [astro-ph]].

[111] R. Engel [Pierre Auger Collaboration], "Test of hadronic interaction models with data from the Pierre Auger Observatory," [arXiv:0706.1921 [astro-ph]].

[112] P. Billoir. "The Muon Hump in the Real Shower Data from the Surface Detector," Pierre Auger Collaboration Technical Note, GAP 2005-004.

[113] K. -H. Kampert and M. Unger, "Measurements of the Cosmic Ray Composition with Air Shower Experiments," Astropart. Phys. **35**, 660 (2012) [arXiv:1201.0018 [astro-ph.HE]].

Vita

Guofeng Yuan was born and raised in Luoyang, an ancient city in China. In 2002, he began his undergraduate study in University of Science and Technology of China, where he earned his Bachelor Degree in Physics in 2006. He began his graduate study in Louisiana State University since Fall 2006 and started the research of Cosmic Rays under Dr. James Matthews since summer 2008. The degree of Doctor of Philosophy will be conferred on him at the December 2012 Commencement.